CRANFIELD UNIVERSITY

LEWIS KIELY

REVIEW OF NEW METHODS OF MODELLING PLASTICITY

SCHOOL OF ENGINEERING

MSC Thesis
Academic Year: 2012 - 2013

Supervisor: Prof. Rade Vignjevic
September 2013

CRANFIELD UNIVERSITY

SCHOOL OF ENGINEERING

MSc Thesis

Academic Year 2012 - 2013

LEWIS KIELY

REVIEW OF NEW METHODS OF MODELLING PLASTICITY

Supervisor: Prof. Rade Vignjevic
September 2013

This thesis is submitted in partial fulfilment of the requirements for the degree of Master of Science

ABSTRACT

Recent short pulse (femtosecond) laser experiments have shown the existence of a so called superelastic precursor for short time periods after shock wave formation. The superelastic precursor is characterised as having amplitude far greater than the Hugoniot Elastic limit.

This work reviews the current orthotropic thermoelastic plastic-damage model developed at Cranfield University, which includes the ability to model high velocity, shock wave forming impacts. The current model is unable to reproduce the superelastic precursor. Recent methods of looking at plasticity are reviewed and model improvements are suggested to enable the Cranfield model to reproduce superelastic precursor waves. The methods investigated are both dislocation based as it is determined that it is necessary to model deformation on the microscale in order to achieve reproduction of phenomena on the timescales of the early stages of shock wave formation and propagation. The methods investigated are the so-called self-organisation of dislocations and a mobile and immobile dislocation method proposed by Mayer.

The plasticity part of the model proposed by Mayer is suggested for further investigation, including implementation into the DYNA 3D hydrocode which contains the current Cranfield model, to numerically asses the models capabilities. Similar, the self-organisation model is put forward for further numerical analysis.

Further, calculation of the continuum Cauchy stress using purely atomistic variables is investigated in the form of the virial stress. It is determined that the virial stress calculation is unsuitable for modelling shock waves, however an alternative atomistic stress calculation which is more suited to shock waves is discussed. It is proposed that this stress calculation could be used to investigate the stresses contained within the thin shock front.

Keywords:

Self-organization, Dislocations, Superelastic precursor, orthotropic, multiscale

ACKNOWLEDGEMENTS

I would like to thank Professor Vignjevic for his help and guidance throughout the completion of this work.

A special thanks goes to Daniel Portelli whose kind help and advice enabled me to find and achieve this opportunity.

It goes without saying I would like to thank my parents, without their support and guidance I would not have been in the position to have completed this work.

Finally I would like to thank my friends, who during the tougher times of the past year have always been there for me to provide support and keep me sane.

TABLE OF CONTENTS

LIST OF FIGURES

NOTATION

Due to the large number of terms used within this work, the notation used throughout may not be consistent between chapters. Due to this, the notation used is defined here for each chapter.

Chapter 3:

Alphabet:

- $\boldsymbol{b}$ - Left Cauchy-Green deformation tensor
- $\boldsymbol{C}$ - Right Cauchy-Green deformation tensor
- C - Current configuration
- C_0 - Initial configuration
- C_{pd} - Intermediate configuration
- $\tilde{C}_{pd}$ - Isoclinic configuration
- $\boldsymbol{d}$ - Rate of deformation tensor
- $\boldsymbol{E}$ - Green-Lagrange strain
- $\boldsymbol{F}$ - Deformation gradient
- $\dot{\boldsymbol{F}}$ - Material velocity gradient
- $\boldsymbol{F}_e$ - Elastic part of the deformation gradient
- $\boldsymbol{F}_{pd}$ - Inelastic part of deformation gradient
- J - The Jacobian
- $\boldsymbol{l}$ - Spatial velocity gradient
- $\boldsymbol{n}, \boldsymbol{N}$ - Unit vectors normal to the surface of spatial and material surface elements
- $\boldsymbol{P}$ - First Piola-Kirchhoff stress tensor
- $\boldsymbol{R}$ - Tensor of rotation
- $\boldsymbol{R}_{dp}$ - Rigid body rotation caused during inelastic deformation
- $\boldsymbol{S}$ - Second Piola-Kirchhoff stress tensor

ds, dS - Spatial and material surface elements

$\boldsymbol{t}, \boldsymbol{T}$ - Traction vectors

t - Time

$\boldsymbol{U}$ - Right stretch tensor

$\boldsymbol{v}$ - Left stretch tensor

v, V - Volume in current and reference configuration

$\boldsymbol{w}$ - Rate of rotation tensor

$\boldsymbol{x}$ - Position vector in current configuration

$\boldsymbol{X}$ - Position vector in reference configuration

Greek alphabet:

$\boldsymbol{\varepsilon}$ - Euler-Almansi strain

ρ_0 - Density in initial configuration

ρ - Density in current configuration

$\boldsymbol{\sigma}$ - Cauchy stress

$\boldsymbol{\Sigma}$ - Mandel stress

$\boldsymbol{\tau}$ - Kirchhoff stress

$\boldsymbol{\chi}$ - Motion

Chapter 4:

Alphabet:

$\boldsymbol{d}$	-	Rate of deformation
$\boldsymbol{E}$	-	Green-Lagrange strain
$\boldsymbol{E}_{tot}$	-	Total energy of the continuum
g	-	Gibbs free energy function
h	-	Enthalpy
K	-	Kinetic energy of the continuum
P_{int}	-	Stress power
$\boldsymbol{q}$	-	Heat flux vector
Q	-	Heat added to the system
Q_{input}	-	Heat input to the system
r	-	Heat source
s	-	Entropy
$\boldsymbol{S}$	-	Second Piola-Kirchhoff stress tensor
U	-	Internal energy
W	-	Work done by the system

Greek alphabet:

Δ	-	Dissipation
Δ_{ad}	-	Adiabatic dissipation
θ	-	Temperature
ρ	-	Density
$\boldsymbol{\sigma}$	-	Cauchy stress
ψ	-	Helmholtz free energy function

Chapter 5

Alphabet:

$\mathbb{A}$	-	State variable determined by structural tensors
$\mathbb{C}$	-	Elastic stiffness tensor
$\boldsymbol{d}_p$	-	Rate of plastic deformation
$\boldsymbol{E}_e$	-	Elastic Green-Lagrange strain
f_d	-	Damage potential
f_{pl}	-	Plastic potential
$I_1 - I_7$	-	Invariants of a stress tensor
$\mathbb{I}$	-	4th order identity tensor
$J_1 - J_7$	-	Invariants of a stress tensor
$\bar{\boldsymbol{M}}^1, \bar{\boldsymbol{M}}^2$	-	Structural tensors
P	-	Pressure
$\boldsymbol{S}, S_{\boldsymbol{ij}}$	-	2nd Piola-Kirchhoff stress tensor
$s(\theta, \dot{\varepsilon}_p)$	-	Thermal activation factor

Greek alphabet:

$\alpha_1 - \alpha_9$	-	Linearly independent material constants
$\beta_1 - \beta_6$	-	Material parameters
$\gamma_1 - \gamma_9$	-	Material parameters
θ	-	Temperature
σ_a	-	Athermal part of the MTS model
$\hat{\sigma}$	-	Plastic evolution parameter
σ_{MTS}	-	Flow stress from the MTS model
Σ^D	-	Deviatoric part of Mandel stress
$\bar{\boldsymbol{Y}}$	-	Damage energy release rate

ψ	-	Helmholtz free energy function
$\bar{\boldsymbol{\omega}}$	-	Damage tensor
ω^H	-	Damage hardening parameter
Ω_0	-	Initial damage hardening conjugate force
Ω	-	Damage hardening conjugate force

Chapter 6:

Alphabet:

- B - Viscous drag of dislocations
- c - Wave velocity
- c_e - Elastic wave velocity
- c_p - Plastic wave velocity
- E - Young's modulus
- E_0 - Energy in front of shock
- E_1 - Energy behind shock
- G - Shear modulus
- K - Bulk modulus
- K_p - Swegle-Grady proportionality constant
- m - Orientation factor
- P_0 - Momentum in front of shock
- P_1 - Momentum behind shock
- P - Pressure
- S - Slope of stress-strain curve
- u - Displacement in the x-direction
- U_p - Particle velocity
- U_s - Shock velocity
- v - Velocity
- V_0 - Volume in front of shock
- V_1 - Volume behind shock
- Y_0 - Yield point

Greek alphabet:

ε	-	Strain
$\dot{\varepsilon}$	-	Strain rate
ν	-	Poisson's ratio
ρ	-	Mass density
ρ_0	-	Mass density in front of shock
ρ_1	-	Mass density behind shock

Chapter 7:

Alphabet:

b	-	Burgers vector
G	-	Shear modulus
h_a	-	Characteristic distance of annihilation of screw dislocations with opposite signs
h_d	-	Mean height of edge dipoles being destroyed by mobile dislocations
h_i	-	Mean height of edge dipoles
K	-	Normalising coefficient
K_0	-	Bulk modulus
K_p	-	Swegle-Grady coefficient
m_T	-	Taylor factor
n	-	Bulk density of dislocation sources
t	-	Time
t_w	-	Time of wave front formation
U	-	Internal energy
U_1	-	Velocity of shock wave
u^a	-	Velocity of dislocations with the same Burgers vector
W	-	Work done on the system
Z	-	Width of shock front

Greek:

α	-	Coefficient of interactions of dislocations
ε_G	-	Wave induced strain inconsistency
ε_{pl}	-	Plastic strain
λ_f	-	Free path of screw dislocations between acts of multiplication on obstacles of deformation origin
λ_{ie}	-	Free path of screw dislocations between acts of DCS with

		formation of edge dipoles
λ_{is}	-	Free path of screw dislocations to obstacles destroying their mobility either through immobilisation or annihilation
λ_m	-	Free path of screw dislocations between acts of multiplication on obstacles of non-deformation origin
λ_p^a	-	Characteristic free path of dislocations before elementary acts of change of density
ρ^a	-	Density of dislocations with the same Burgers vector
ρ_i	-	Density of immobile dislocations
ρ_m	-	Density of mobile dislocations
σ	-	Compressive stress
σ_p	-	Maximum stress
ψ, X, T	-	Dimensionless variable, coordinate and time, respectively

Chapter 8:

Alphabet:

- b - Modulus of Burgers vector
- B - Friction coefficient
- c_t - Transverse speed of sound
- k_a - Coefficient of annihilation
- k_g - Coefficient of generation
- P - Pressure
- Q_D^β - Generation rate of mobile dislocations
- Q_I^β - Generation rate of immobile dislocations
- S_{ik} - Stress deviator
- U - Specific internal energy
- V_D^β - Velocity of mobile dislocations
- V_I - Characteristic velocity of dislocation movement during the process of consolidation
- v_i - Mass velocity
- w_{ik} - Plastic deformation tensor
- W_{ik} - Fracture deformation tensor
- Y - Yield strength

Greek:

- ρ - Mass density
- ρ_D^β - Density of mobile dislocations
- ρ_I^β - Density of immobile dislocations
- ρ_0 - Minimal density of dislocations
- σ_{ik} - Mechanical stresses

Chapter 9:

Alphabet:

- $\boldsymbol{b}$ Body force
- B Bond function
- $\boldsymbol{f}_\alpha$ Force on particle alpha
- $\boldsymbol{f}^{ext}$ External force
- $\boldsymbol{f}^{int}$ Internal force
- m_α Mass of particle alpha
- $\boldsymbol{p}_\alpha$ Linear momentum of particle alpha
- $\boldsymbol{r}_\alpha$ Displacement of particle alpha from the position of the centre of mass of the system
- $\boldsymbol{t}$ Traction
- $\boldsymbol{\mathcal{T}}_\alpha$ Kinetic tensor
- $\boldsymbol{v}_\alpha^{rel}$ Velocity of particle alpha relative to the centre of mass of the system
- V Volume
- $\boldsymbol{\mathcal{W}}_\alpha$ The Virial tensor
- $\boldsymbol{x}$ Position of the centre of mass of the system
- $\boldsymbol{x}_\alpha$ Position of particle alpha

Greek:

- $\boldsymbol{\sigma}$ Cauchy stress tensor
- τ Atomistic time
- ϕ^α Atomistic potential energy
- $\psi(\boldsymbol{x}_\alpha - \boldsymbol{x})$ Localisation function

LIST OF ABBREVIATIONS

SC	Simple cubic
BCC	Body centred cubic
FCC	Face centred cubic
MTS	Mechanical threshold stress model
HEL	Hugoniot elastic limit
EOS	Equation of state
TEM	Transmission electron microscope
LEDS	Low energy dislocation structures
CA	Cellular automata
MD	Molecular dynamics

1 Introduction

Accurate modelling of the deformation of material is of great benefit to many areas within industry. Many metals which are used extensively for various applications exhibit anisotropic properties which are caused during the working and forming of structures from such metals. Anisotropy is characterised as a directional dependence on the material properties. The focus of this work is on the modelling of orthotropic metals. Orthotropic metals are a subset of anisotropic materials with a set of three mutually orthogonal planes of symmetry.

The main aim of this work is to propose model improvements which can be implemented in the future into a material model which was developed within the School of Engineering at Cranfield University. The current model, referred to as the Cranfield model in this work, has the capability of reproducing elastic deformation, plastic deformation and damage of orthotropic metals, including under high velocity impacts. High velocity impacts can induce shock waves to form and propagate through the metal. The current Cranfield model reproduces shock waves, however, recent experiments have shown that for short time periods after a shock inducing impact, the shock wave formed can have an elastic precursor wave with greater amplitude than the elastic limit. This behaviour cannot be reproduced by the current Cranfield model. This work is therefore proposing model improvements which will allow the current Cranfield model to more accurately reproduce this behaviour. To achieve this it is necessary to model behaviour on the microscale to provide the time resolution required.

It has long been established that plastic deformation of metals with specific crystal structures is determined by the processes associated with microscale properties of the metal, predominantly in the motions, generation and annihilations of crystal imperfections called dislocations. To accurately model these processes it is required for the model to be able to model processes on a microstructural scale. Currently the Cranfield model is developed in a continuum

mechanics framework, therefore future developments point towards a multiscale approach being required.

The multiscale modelling approach is investigated by reviewing existing plasticity and shock wave models which are available in literature. The models of interest are dislocation based models, with two particular methods being analysed in depth. These two methods are the so called self-organisation of dislocations and a plasticity model proposed by Mayer et al.

Further to the models in literature, an investigation has been carried out to determine the applicability of using an atomistic scale stress tensor, referred to as the Virial stress, in the context of multi-scale modelling, specifically applied to the conditions under which shock waves form and propagate.

1.1 Aims and objectives

The overall aim of this work is to propose model improvements for the existing Cranfield model which has been developed in the department of applied mechanics and astronautics at Cranfield University.

The objectives to achieve the aim are:

- Identify new models of plasticity which appear to meet the requirements for future implementation in to the current Cranfield model.
- Critically review the identified methods for plasticity to determine the full range of applicability of the method and to identify potential weaknesses in the method.
- To assess the applicability of applying the Virial stress tensor to the context of multi-scale modelling, specifically in the case of considering a shock wave forming and propagating through a metal.

1.2 Thesis Structure

Chapter 2 introduces the materials of interest for this work, focussing on the atomistic scale arrangement of the materials. Further, the relevant mechanisms for deformation are described.

Chapters 3 and 4 outline the relevant continuum mechanics and thermodynamics required for understanding the development and formulation of the current Cranfield model, which is then introduced in chapter 5. The areas for which improvements are being proposed are highlighted in the relevant sections of this chapter.

The condition required for the formation and propagation of shock waves are given in chapter 6. The mathematical relations governing material properties, which are used in the modelling of shock wave propagation, are given.

In chapter 7 the method of dislocation self-organisation is discussed. This method explains in depth the nature of dislocation patterning which occurs naturally within metals under plastic deformation. As well as the self-organisation method, a shock wave model born out of the equations describing the self-organisation is also reviewed.

A review of a recent plasticity and failure model is carried out in chapter 8. The formulation of the model as well as the relevant results and limitations are analysed. A comparison of the shock wave modelling capability of this model and the shock wave model review in chapter 7 is also made.

Finally in chapter 9, the applicability of the atomistic virial stress calculation to the modelling of shock loading is determined.

The remainder of this chapter will discuss the significant historical models of plasticity, providing the background of the current development of the Cranfield model, along with outlining the methodology and reasoning behind the process of choosing the two models to study in detail.

It is widely observed that the effect of strain rate on the flow stress, or the dynamic strength of the metal, is non-linear, with the degree of dependence varying as the strain rate increases. It is seen in Figure 1 that effect of the strain rate on the dynamic strength of a material is non-linear and consists of three major regimes.

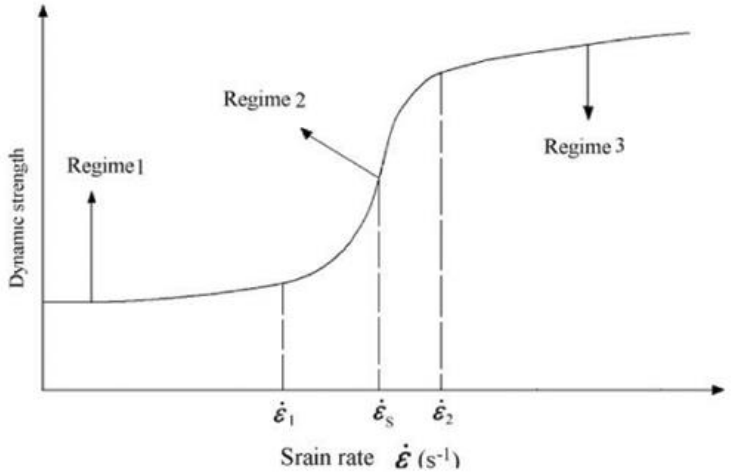

Figure 1: A typical dynamic strength or yield strength versus strain-rate curve showing three clear regimes. Regime 1 shows little rise in dynamic strength with increasing strain-rate, regime 2 shows a strong change in dynamic strength with increasing strain-rate, and regime 3 shows, as in regime 1, little increase in the dynamic strength with increasing strain rate [1].

One of the earliest attempts to include the strain rate dependency in to the plasticity model was made by Johnson and Cook [2]. The proposed an empirical model of some simplicity, containing three main terms which accounted for the dependence of strain, strain rate and temperature on the flow stress. The model accounted for hardening caused by strain and for thermal softening [3]. In its original form, the model contains five material constants, all of which are obtained from experimental data, with many methods of obtaining these being available in literature. Whilst the Johnson-Cook model has been widely used [4] it is a fully empirical model, which does not include the physics of the microstructural processes that are dominant during plastic deformation.

An early attempt to model at very high strain rates, regime 3 on Figure 1, was made in 1980 in the form of the Steinberg-Guinan model. The model, in its original form [5] was only applicable to high strain rates, where increasing strain rate has little impact on the dynamic strength of the metal, as the yield strength calculation in the model is independent of the strain rate. The value of the strain rate obtained experimentally and used as this limitation was 10^5 s^{-1} [6]. The

model was extended by Steinberg and Lund [7] in 1989 to include low strain rates, incorporating the strain rate dependency of the yield stress.

Further, in 1987 the Zerilli-Armstrong model was proposed. This model is based on simplified dislocation dynamics, specifically focussing on the thermal activation of dislocations. A key feature of this model is that it contains separate equations providing a flow stress depending on the structure of the metal being modelled. This is due to observations relating to differing dependencies of the strain rate and temperature on the flow stress for different structures and the observation that the activation area of dislocations is dependent on strain for fcc structures but independent for bcc structures [4]. Despite the spate equations for differing structures, the number of parameters required in the Zerilli-Armstrong model is low with a total of five required.

It will be seen later in this work that the Mechanical Threshold Stress model (MTS) is of significant importance to this work as it is a part of the current Cranfield model. The MTS model was first proposed in 1988 by Follansbee and Kocks. As with the Zerilli-Armstrong model, the MTS model is built around the thermal activation of dislocations. Again, the model provides a flow stress, which is calculated from two key terms in the function: an athermal part and the thermally activated part. The MTS model is examined in more detail in section 5.3.1 where it is shown how the model fits in with the current Cranfield model. One of the key assumptions that the MTS model is built on, and consequently a limiting factor, is the assumption that the viscous drag effects are small compared to the dominant thermally activated dislocation motion [8]. This assumption holds only for strain rates up to around $10^4 s^{-1}$, therefore limiting the range of validity of the MTS model to the same strain rate.

With consideration given to the above models, two more recent plasticity models were chosen as a focus for the remainder of this work. These two chosen models were the self-organising processes of dislocations method by Malygin [9] and the latest mobile/immobile dislocation model by Mayer et al. [10] After surveying currently available literature, these two model have been

chosen as they meet specific needs or areas of future research of the Cranfield model and the sponsors of this project.

The method used to identify relevant models included searching literature for recently published models which shown the characteristics identified as relevant for future inclusion into the Cranfield model. The characteristics used were:

- Model capable of modelling the metals of interest,
- High velocity/shock wave capabilities
- Microscale effects present within the model
- Continuum mechanical basis to ensure the method is in line with the framework of the current Cranfield model
- Ability to capture timescales of interest in a predominantly continuum model

The self-organisational processes of dislocations model [9] was identified for further analysis as, further to meeting the above criteria, the shock wave part of the model shows a natural reproduction of the Swegle-Grady power law (see section 6.5).This power law is a well-established empirical law, of which the exact physical origin is unknown. The power law naturally arises in the shock wave part of the self-organisational processes of dislocations model when considering the dislocation densities generated at the shock wave front. The calculation of the dislocation densities is a key part to this method, including a wide range of dislocation processes observed to alter the dislocation density, therefore capturing the physics governing the microstructural deformation, before feeding this up to the continuum scale via the density calculation. This power law being present is of interest as it is a future aim of the continuation of this work to investigate the physical reasoning behind the law/

The Mayer's model was chosen for further analysis as it meets all of the criteria outlined above, plus the initial reported results of the model show the reproduction of the superelastic precursor wave (amplitude of the elastic precursor of a shock wave being higher than the Hugoniot elastic limit). This precursor phenomena, which is observed on the timescale of a few nanoseconds is one of the main behaviours future iterations of the Cranfield model are aiming to reproduce. This is the only model for which this behaviour

was observed. The Mayer model treats mobile and immobile dislocations as two separate processes (mobile and immobile dislocation type model). Calculation is made of the densities of both the mobile and immobile dislocations, which account for certain dislocation altering processes, which is then used in the continuum model to calculate the materials response to loading.

2 Crystal structures and deformation processes

The materials of interest for the future development of the Cranfield model are limited to metals with a cubic structure, and an orthotropic nature. To gain an understanding of the physical processes that govern the material response to loading and the mechanisms for deformation, this chapter discusses the structures of the metals of interest on a microscopic scale and outlines the main deformation mechanisms of interest. This chapter contains eight sections; sections 2.1, 2.2 and 2.3 discuss the cubic crystal structures of metals. The concept of slip systems, a key concept when considering inelastic deformations, is then introduced in section 2.4, while imperfections in crystals are discussed in sections 2.5 and 2.6, with section 2.6 focussing on dislocations, as these are the main imperfections on the microscale that are of interest when modelling deformation. Finally a note is given to a different microstructural method of deformation, in twinning, with the chapter concluding with a summary in section 2.8.

All truly solid materials, including all metals are considered to be crystalline. This means that when they are looked at on an atomic level, a regular repeating arrangement of atoms or molecules is seen. By definition, this is a crystal. A large piece of metal will contain many crystals, all with different orientations. The individual crystals in the metal, referred to as grains and can be observed when then metal is highly polished and examined under a microscope.

The formation of such crystals is due to a balance of repulsive forces from surrounding atomic nuclei, and attractive forces from electrons forming the bonds between atoms. The locations of atoms in the crystal are the locations of the least potential, i.e. lowest energy.

The smallest repeating pattern within the crystal is referred to as the unit cell. There are only 14 lattices which meet the requirements to be a unit cell [11], and of these only about six are commonly met. For the purposes of this work only two are studied in detail, these are the face-centred cubic structure and the

body-centred cubic structure. For reference, a third simple cubic structure will also be introduced.

2.1 Simple cubic (SC)

The simple cubic structure is a cubic structure containing 8 lattice points, one on each corner of a cube, as shown in Figure 2-1.

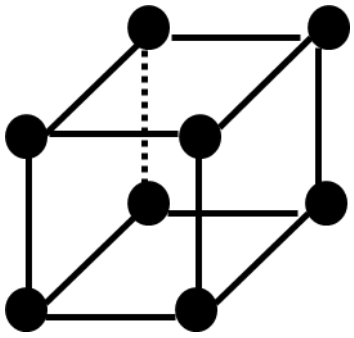

Figure 2-1: The simple cubic structure.

The only metal known to crystallise into a simple cubic structure is radioactive polonium in its alpha form. However, due to its simplicity it is a useful structure for introducing the main ideas and concepts surrounding unit cells. Within the unit cell, the position of each lattice point, or in metals the atoms, can be expressed using the lattice vectors **A, B** and **C** as shown in Figure 2-2, where a, b and c are lattice parameters defining the size of the unit cell. For the cubic structures of interest in this work a, b and c will take the same value.

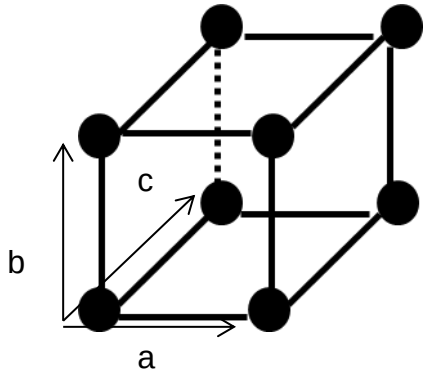

Figure 2-2: Simple cubic structure including lattice vectors, as the unit cell is cubic a=b=c in magnitude.

Due to the nature of most crystal structures, the properties of the metal are different depending on the direction taken through the crystal. Therefore it is necessary to use a method of describing individual planes of atoms, these are effective layers of atoms, which when stacked in a parallel fashion will result in the crystal structure being formed. The commonly used method of defining the specific planes within the crystal is by using Miller Indices.

The Miller indices are given as a set of three numbers, e.g. (hkl), which indicate a scaled value of the reciprocals of the crystal axes intercepts in a single unit cell. Using the axes shown in Figure 2-2 as the crystal axes, there are three steps for determining the Miller indices [12]:

i) Determine the intercepts the plane will make with the three crystal axes. These intercepts should be expressed as the number of axial lengths, with the axial lengths being the values of a, b, and c in Figure 2-2.
ii) Take the reciprocals of these intercepts.
iii) Scale the reciprocals to the smallest integers for which the same ratio is maintained.

The origin of the crystal axes can be taken as any point in the crystal, therefore due to this, it can be seen that there will be many parallel planes for which the same Miller indices will describe. The indices of a family of parallel planes are enclosed in curly braces.

Figure 2-3 shows three commonly observed planes within a cubic structure. These are the (1 0 0), (1 1 0) and (1 1 1) planes, shown here in a simple cubic structure, however the same planes, with a slightly different atomic arrangement contained upon them, are observed in both the body centred cubic structure and the face centred cubic structure.

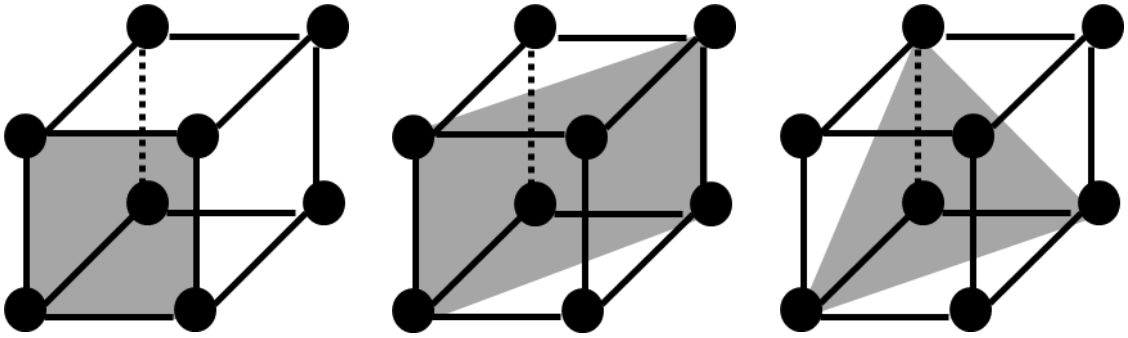

Figure 2-3: Diagrams indicating i) the (1 0 0) plane, ii) the (1 1 0) plane and iii) the (1 1 1) plane of the simple cubic structure.

Further to their use for defining planes within crystals, Miller indices are also used to identify directions through the crystal. A direction can be defined by choosing a point on the crystal and constructing a straight line through the point and the origin of the crystal axes. The direction is then the direction in which the straight line is pointing, and its Miller indices are defined by the crystal coordinates of the initially chosen point. To distinguish between the indices for a plane and those of a direction, directional indices are contained within square brackets. Figure 2-4 shows the commonly used directions within a cubic crystal.

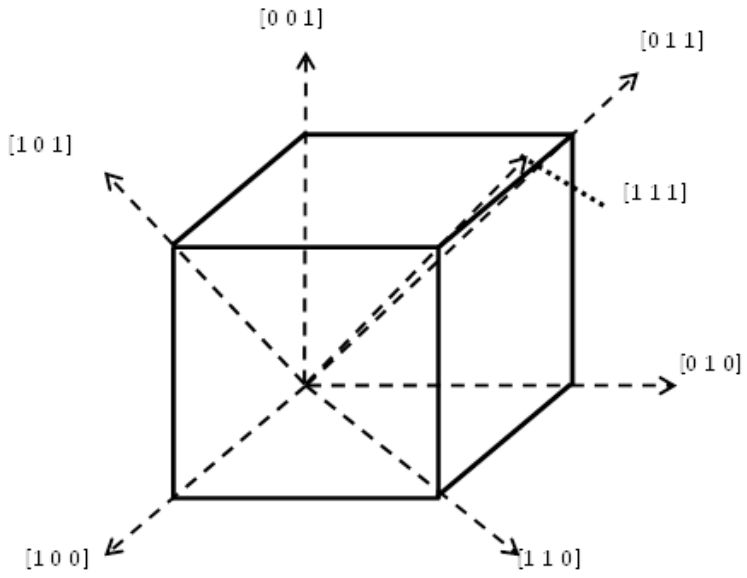

Figure 2-4: Diagram showing the main directions within a cubic crystal structure

As with planes, there are many directions within a crystal that are parallel. Families of parallel directions are identified using angled braces. With all Miller Indices, for both planes and directions, negative values are indicated using a bar over the negative value, i.e. $(1\,1\,\bar{1})$.

The packing fraction of the unit cell is the fraction of space that is occupied within the cell. It can be thought of by expanding the atoms on the lattice points so that they are all in contact. The packing fraction is now the volume occupied by the enlarged atoms divided by the volume of the whole unit cell. It should be noted that the number of atoms within the unit cell is a sum of the number of whole atoms contained entirely in the cell, plus the fractions of atoms that are shared with neighbouring unit cells. For a simple cubic structure, only one atom would be considered to be contained in each cells, as the eight atoms on the lattice points are contained within eight cells, therefore the value of an eighth is taken for each one.

2.2 Face-centred cubic (FCC)

The face-centred cubic structure is similar to the simple cubic; it is cubic with an atom at each corner of the cube, however it also has an additional six points, located at the centre of each face of the cubic structure as shown in Figure 2-5.

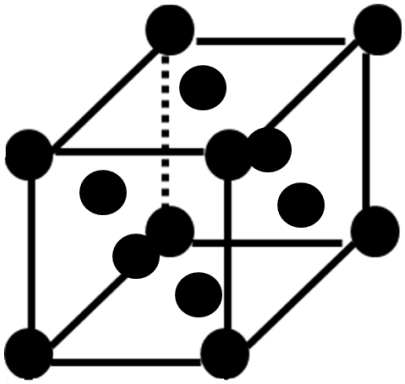

Figure 2-5: The face-centred cubic unit cell.

A FCC unit cell contains four whole atoms, leading to a packing fraction of 0.74 which is much higher than that of a simple cubic structure. It actually has the largest packing fraction of the three cubic structures considered in this work.

Many useful engineering metals have a FCC structure, including copper, aluminium, gold, lead and silver, as well as many more.

2.3 Body-centred cubic (BCC)

The body centred cubic structure is also a cubic structure similar to the simple cubic, but it has the addition of a lattice point in the centre of the body of the cube, shown in Figure 2-6.

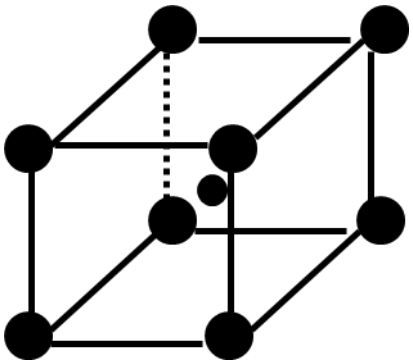

Figure 2-6: The body-centred cubic unit cell.

A BCC unit cell contains two whole atoms, leading to a packing fraction of 0.68. This is larger than that of a simple cubic structure, but not as large as that of an FCC structure.

Common engineering metals that have a BCC structure include iron (except between the temperature range of 910-1400°C), tungsten and chromium.

2.4 Slip systems

When a loading is applied to a metal, deformation can occur. Elastic deformation occurs when a relatively small loading, below the yield stress, is applied. Under elastic deformation, the positions of the atoms are shifted slightly away from the lowest energy configuration in which they naturally lie but return to their original positions upon unloading of the metal, reversing the deformation.

If a loading is applied which is in excess of the yield stress, the metal will deform inelastically. Inelastic deformation occurs by planes of atoms slipping over one another, which remain in their new locations upon unloading. The

specific planes of atoms which slip and the directions in which they can slip are determined by the slip systems of the structure of the metal.

Figure 2-7: Diagram showing 1) an un-deformed piece of metal with no loading and 2) the slip mechanism occurring during loading of the metal. The direction of the force applied to the metal is shown by the arrow with the slip directions visible in the body of the metal [13]

The planes of atoms which are most favourable for slip to occur are generally the planes with the greatest inter-planar spacing, as the forces between sliding planes will be at a minimum [12]. The planes with the greatest inter-planar spacing are also found to be the most atomically dense planes. Figure 2-7 shows how, when a load is applied to a sample of metal the deformation occurs due to planes of atoms slipping over one another. Image 1 in Figure 2-7 shows the initial un-deformed sample of metal; with image 2 showing the same sample after inelastic deformation has occurred. Stress has been applied to the sample in the horizontal direction, indicated by the arrow, with the deformation occurring due to slip of the slip systems observable as parallel lines of deformation.

In FCC metals, the planes with the greatest inter-planar spacing, and the most atomically dense are the {1 1 1} planes. Therefore these are the primary slip planes in FCC structures. For each unit cell, there are four such {1 1 1} planes. Each of these planes have slip directions of the <1 1 0> family. Therefore, the number of slip systems in each FCC unit cell is twelve.

For BCC metals there are a minimum twelve slip systems, however there can be as many forty-eight depending on the specific metal being analysed. The twelve slip systems that are common to all BCC structures are the {1 1 0} planes and the <1 1 1> directions. In certain BCC metals, the (2 1 1) planes and

the (3 1 1) planes form additional slip planes. As with the {1 1 0} planes, these additional planes have <1 1 1> directions.

2.5 Imperfections in crystal lattice

The theoretical strength of metals predicted by the consideration of slip planes in a perfect lattice is far greater than is observed experimentally. Experimentally single crystals are seen to be much softer; therefore it is important to consider imperfections which naturally occur in the crystal lattice. There are several types of imperfections which are observed which can be categorised into four main groups; these are: point defects, line defects, planar defects and volume defects.

The main group of defects of interest within this work is line defects which are made up of dislocations. However, as point defects can immobilise dislocations it is necessary to first introduce them.

Point defects consist of vacant atom sites in the lattice and interstitial atoms. Vacant atom sites are observed as a missing atom from a lattice point where upon an atom would be expected to be found, as shown in Figure 2-8(a). Interstitial atoms are observed as atoms occupying an interstice rather than a lattice site, as shown in Figure 2-8(b).

(a) (b)

Figure 2-8: Diagrams showing (a) a lattice vacancy and (b) an interstitial atom.

2.6 Dislocations

The main consideration for the lower than theoretical strength of metals is line faults, which are formed from the theory of dislocations.

As planes of atoms slip over one another, as already stated, the theoretical strength of the material is high, requiring a large loading to be applied. That slip

is observed along the slip planes under much lower loading forces indicates that the atomic planes do not slip as a rigid body, but by a process that starts in a localised region and spreads. As this process is followed, the plane will consist of two regions: an already slipped region and an un-slipped region. Separating these two regions will be a discontinuity referred to as a dislocation.

The dislocations which occur at the boundaries are of two types: edge dislocations and screw dislocations. Edge dislocations are caused by an extra half layer of atoms as shown in Figure 2-9.

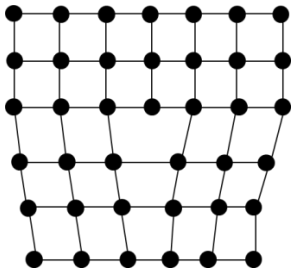

Figure 2-9: Schematic diagram showing an edge dislocation.

A screw dislocation can be thought of as an imaginary slice being made into an otherwise perfect lattice, with the two sides of the slice at the edge of the metal being skewed one atomic spacing forming the dislocation. This is shown in Figure 2-10.

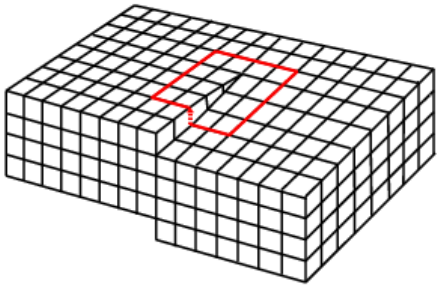

Figure 2-10: A screw dislocation [14]

Dislocations aid the deformation of metals as they can be mobile and can therefore propagate through the lattice. The propagation of a dislocation can cause the same effect as an entire plane of atoms slipping. The motion of

dislocations is not random and is governed by a property known as the Burgers vector.

2.6.1 Burgers vector

The Burgers vector is an important parameter when considering dislocation motion. As a dislocation moves across the slip plane, atomic displacements are produced. These atomic displacements are defined by the Burgers vector.

The Burgers vector itself is defined for a dislocation by taking a clockwise loop around the dislocation. If an equal number of atomic spacing's is travelled in all directions the loop will not be a closed one. This is shown for an edge dislocation in Figure 2-11 by the red line. To close the loop, the arrow is added. This arrow is the Burgers vector.

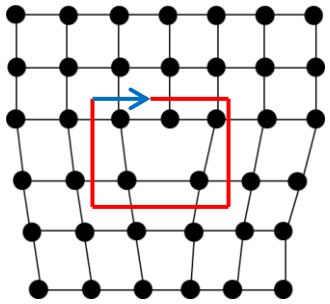

Figure 2-11: Burgers loop for an edge dislocation

The actual value of the Burgers vector is determined by the crystal structure of the metal. The passage of a dislocation does not alter the structure: the structure before passage of a dislocation is identical to the structure after the passage of a dislocation.

From Figure 2-11 it can be seen that, for a single dislocation, the Burgers vector is always one atomic spacing and it is therefore assumed that the Burgers vector is equal to one lattice vector (lattice vectors defined in section 2.1). This lattice vector is usually found to be the shortest lattice vector; however, as only BCC and FCC structure are of interest in this project the lattice vectors have the same length.

2.6.2 Mechanisms for slip

When a sufficient force is applied to the slip plane, the dislocations contained within the plane will propagate through the plane which causes the same effect as an entire plane of atoms slipping. The method in which an edge dislocation propagates is shown in Figure 2-12. The motion of edge dislocations is observed to always be perpendicular to the line of dislocation.

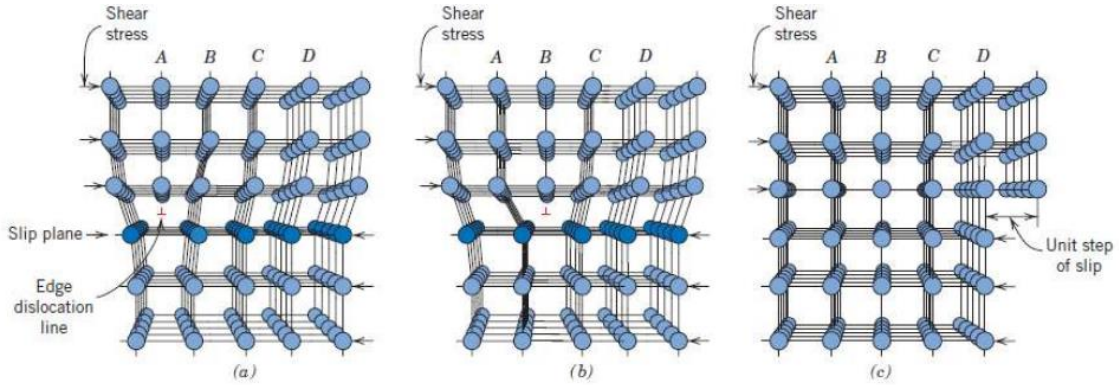

Figure 2-12: Propagation of an edge dislocation [15].

Figure 2-13 shows the mechanism for screw dislocation propagation. Unlike edge dislocation motion, screw dislocations propagate parallel to their line of dislocation.

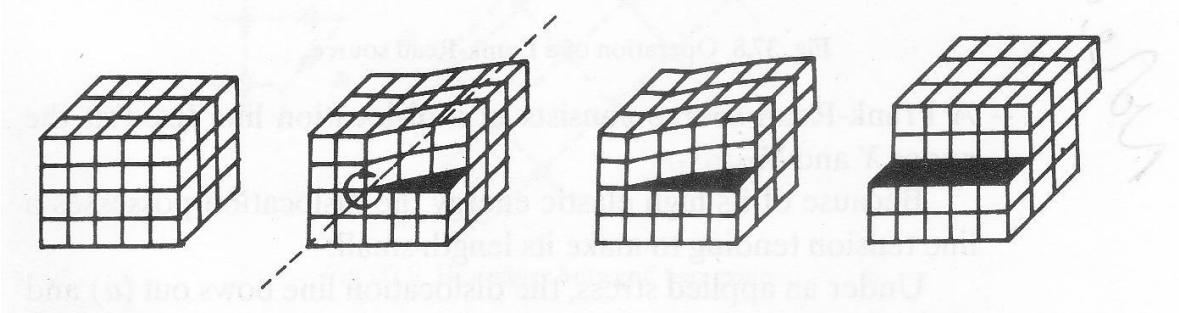

Figure 2-13: Propagation of a screw dislocation [16]

The glide of dislocations is confined to slip planes which contain both the line of dislocation and its Burgers vector. Due to this edge dislocations are confined to a single slip plane. Screw dislocations however are not restricted to a single slip plane. A screw dislocation can glide into other slip planes, which share a common slip direction with the original slip plane, via a cross slip plane [17], as

indicated in Figure 2-14. The reason for this occurring for screw dislocations is due to the cylindrical symmetry of a screw dislocation about its axis. The Burgers vector is parallel to this axis, which results in all crystal planes passing through the axis to look the same to a screw dislocation.

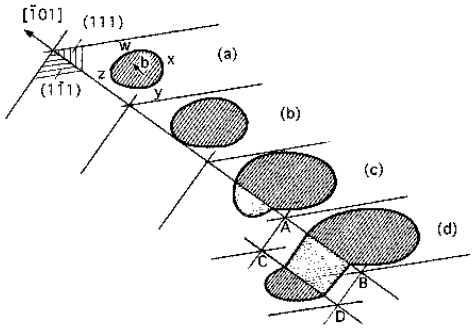

Figure 2-14: Diagram showing the propagation of a screw dislocation in an FCC crystal, with cross plane slip occurring in (c) and (d) [18].

It is important to highlight that dislocations intersecting slip planes, i.e. the Burgers vector of the dislocation and line of dislocation do not lie in the slip plane, have the effect of point obstacles, which halt the glide of dislocations in the slip plane. These intersecting dislocations are commonly referred to as forest dislocations and can provide a pinning mechanism for dislocations which can then form sources to generate further dislocations.

Associated with each dislocation contained in the slip plane are compressive and tensile fields. This is due to the strain of the crystal surrounding the dislocation. These force fields, as shown in Figure 2-15 can attract dislocations, or repel dislocations from one another. It is convenient to use a sign convention to describe the characteristics of dislocations. A dislocation where the extra half layer of atoms lies above the slip plane is deemed to have a positive sign, whereas a dislocation where the extra half layer of atoms is below the slip plane is deemed a negative dislocation.

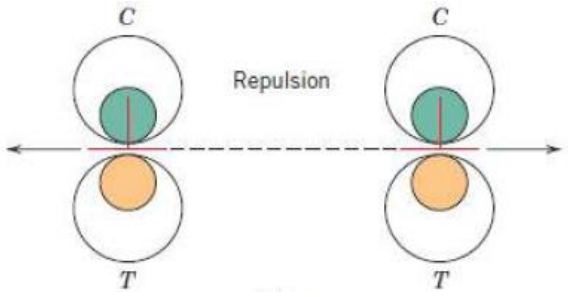

Figure 2-15: Diagram showing two dislocations with the extra half layer of atoms both lying above the slip plane, with the associated compressive and tensile force fields labelled as c and T respectively. As both of these dislocations have the same (positive) sign, a repulsion force is present between them [15].

The sign convention is a useful concept as it allows for easy understanding of the forces between dislocations contained in a slip plane. Dislocations with the same sign, e.g. two dislocations lying above the slip plane, will repel each other, whereas dislocations of opposite signs will attract one another. The attraction is shown in Figure 2-16, where it is seen that when two dislocations of opposite signs meet, they will annihilate each other, leaving a perfect lattice.

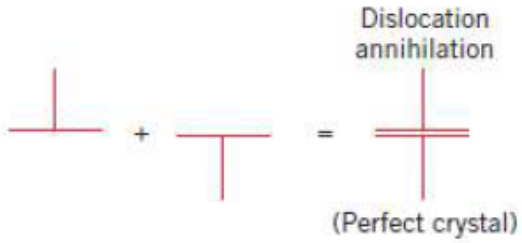

Figure 2-16: Schematic diagram of two oppositely signed dislocations. The positive (left) and the negative (right) dislocations will attract each other, annihilating when they meet [15].

So far all of the dislocations being considered occur within the crystal, and as will be seen in section 2.6.4 are generated by the activation of sources, are contained within the crystal. However, under certain conditions, dislocations are generated at the edge of the crystal. These dislocations are referred to as geometrically necessary dislocations. These predominantly occur at the boundaries between grains during the deformation process. The GND are must

be formed at such boundaries in order to maintain continuity across the boundary. GND are not only formed between grain boundaries, they are also necessary to form when a large geometrical change is observed, this could be during the bending of a sample. As the sample bends, GND will be formed along the top edge of the crystal to prevent the failure of the metal along this edge. GND will have significance in this work when considering the modelling of the front edge of a shock wave.

2.6.3 Climb

The mechanism for the propagation of an edge dislocation outlined restricts the motion of the dislocation to the slip plane containing both the dislocation line and its Burgers vector. However, under certain circumstances, a process referred to as climb can occur. Climb is the movement of an edge dislocation normal to the slip plane.

For climb to occur, non-conservative processes are required to occur, such as the diffusion of lattice vacancies to the line of dislocation. As the processes required are non-conservative, climb requires energy which is usually in the form of a thermal activation [19].

Dislocation climb is an important process as it can allow dislocations which are immobilised by point defects to overcome the effects immobilising them, and regain mobility.

2.6.4 Generation of dislocations

Contained within the structure of metals there are many dislocations. As loading is applied to the metal, and as plastic deformation occurs more dislocations are generated. The main mechanism for this generation is Frank-Reid sources.

The easiest way to consider a Frank-Reid source is by considering a dislocation line that is locked into place at each end, as shown in Figure 2-17.

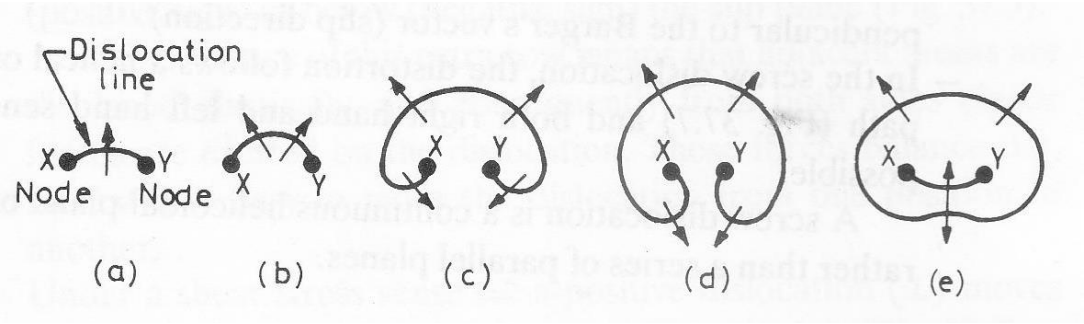

Figure 2-17: Frank-Reid source [16]

If a shear stress is applied, a critical value can be reached, whereupon the dislocation line will begin to curve outwards. The line will continue to curve outwards until the maximum applied stress is reached, this happens when the line has a semi-circular form, part (b) of Figure 2-17. After this occurs, the dislocation will no longer be stable and will therefore continue to expand. Each part of the line will be expanding at the same velocity as the stress acting on all parts of the line is equal. This causes the spiral to form around points X and Y in Figure 2-17(d).

With the line continuing to expand, two parts of the line, as shown in Figure 2-17(d), will approach each other. The two parts of the line will have the same Burgers vector, as the two parts are from the same line, however due to the evolution of the line, they will have opposite signs. As a result of this, when the two lines meet, dislocations will annihilate on contact resulting in a closed loop forming, Figure 2-17 (e). This closed loop continues to propagate through the metal, whilst the original dislocation line XY is reformed in its original state and the process is repeated.

2.7 Twinning

In a metal containing many slip systems, deformation by slip is the most dominant deformation mechanism. However, other deformation mechanisms exist. One of these is twinning. Whereas slip is a process associated with a line defect, twinning is associated with a plane defect, the twin boundary [12].

When shear stress is applied, the lattice direction of the crystal is altered so that one half of the crystal is the mirror image of the other. The line of the mirror is

the twinning plane. Figure 2-18 shows how the deformation produced by slip and twinning differ.

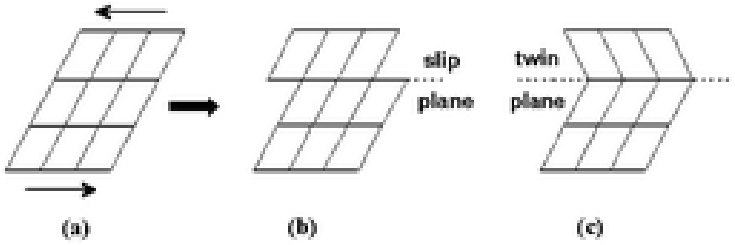

Figure 2-18: Diagram showing the difference between slip deformation and twinning. (a) shows the parent, un-deformed configuration, (b) the specimen having undergone slip and (c) the specimen when twinning has occurred [20].

The typical stress required to produce twinning is higher than that required for slip. Therefore twinning is predominantly seen in metals with a low number of slip systems, typical of hexagonal structures, or during shock loading at low temperatures such as in BCC iron. Despite the required stress for twinning being greater than is required for slip, it is still much lower than the theoretical strength of a perfect crystal would be [19]. This indicates that as with slip, dislocations are involved in the twinning process.

2.8 Summary

The crystalline nature of metals has been introduced with the important properties requiring consideration when modelling being outlined. The important properties of the BCC and FCC structures have been outlined as these are structures of the metals of interest to the project sponsor.

The slip system mechanisms for inelastic deformation has been shown, which in conjunction with crystal imperfections, in the form of dislocations, forms the backbone of microstructural plastic deformation.

The key details of dislocation properties, in the Burgers vector, the slip plane and dislocation link, and the generation mechanism have been detailed. These concepts are vital for the subsequent chapters in this work.

3 Relevant continuum mechanics

The current Cranfield model is derived within a continuum mechanics framework. This chapter presents the basic concepts of the continuum mechanics method, introducing the important measures and relations which are used within the Cranfield model. This chapter is intended to be an easily accessible reference for the reader, providing support for chapter 5 where the current Cranfield model is introduced.

The continuum mechanics framework is used for ease of modelling. A continuum approach considers the material being modelled to be made up of continua. A continuum is considered to be a continuous medium in which the material is evenly distributed throughout [21]. In order for this to hold true the size of the continuum must be large enough for the discrete nature of individual atoms to not be apparent. Eliminating the need to model each atom as a discrete particle significantly reduces the complexity of modelling. This section will introduce the required relationships and concepts of continuum mechanics used in material modelling.

First it is important to define a reference configuration. A material is regarded to be in a current configuration, however in order to measure deformations there needs to be a reference. The reference configuration provides this reference. It can be the initial configuration of the material, prior to and motion or deformation, or it can be a separate configuration in which the material does not achieve during the motion.

Motion can be described by the mapping of a point in the reference configuration to a corresponding point in the current configuration. This can be done by consideration of a point X in the reference configuration with position vector **X**. After deformation the point will be at position vector **x** in the current configuration, and for convenience shall be called point x. The mapping from **X** to **x** is achieved through the motion

$$\boldsymbol{x} = \boldsymbol{\chi}(\boldsymbol{X}, t) \qquad \textbf{(3-1)}$$

where χ is the motion. It is a time dependent vector valued vector function [22]. The inverse motion can be calculated, mapping point x in the current configuration back to point X in reference configuration.

$$\boldsymbol{X} = \boldsymbol{\chi}^{-1}(\boldsymbol{x}, t) \tag{3-2}$$

3.1 Deformation measures

The deformation measures used for the derivation and framework of the Cranfield model are introduced here.

The deformation gradient is a measure of deformation between the reference and current configurations and is arrived at by partial differentiation of equation (3-1) with respect to X.

$$d\boldsymbol{x} = \frac{\partial \boldsymbol{x}}{\partial \boldsymbol{X}} d\boldsymbol{X} \tag{3-3}$$

Where

$$\boldsymbol{F} = \frac{\partial \boldsymbol{x}}{\partial \boldsymbol{X}} = \frac{\partial \chi(\boldsymbol{X})}{\partial \boldsymbol{X}} = Grad\boldsymbol{x}(\boldsymbol{X}) \tag{3-4}$$

is the deformation gradient. The uppercase G in equation (3-4) indicates that the deformation gradient is taken with respect to the reference coordinates. If the deformation is being mapped back from the current to the reference configuration, then the deformation gradient is taken with respect to the current coordinates and is shown in equation (3-5).

$$\boldsymbol{F^{-1}} = \frac{\partial \chi^{-1}(\boldsymbol{X})}{\partial \boldsymbol{x}} = grad\boldsymbol{X}(\boldsymbol{x}) \tag{3-5}$$

The lowercase g in the grad term in equation (3-5) indicates that the gradient is taken with respect to the current configuration.

The change in volume between the reference and current configurations is given by the determinant of the deformation gradient tensor and is commonly referred to as the Jacobian

$$dv = det\boldsymbol{F}dV = J(\boldsymbol{X}, t)dV \quad \textbf{(3-6)}$$

As mass is conserved during deformations, the Jacobian can be shown to relate the densities in the reference and current configurations.

$$\frac{\rho}{\rho_0} = J^{-1} \quad \textbf{(3-7)}$$

3.2 Polar Decomposition

One of the fundamental principles of continuum mechanics is polar decomposition of the deformation gradient. This means that the deformation gradient can be split into an elongation term and a rotational term as shown in equation (3-8).

$$\boldsymbol{F} = \boldsymbol{RU} = \boldsymbol{vR} \quad \textbf{(3-8)}$$

Where $\boldsymbol{U}$ and $\boldsymbol{v}$ are unique positive definite, symmetric tensors. $\boldsymbol{U}$ is referred to as the right (symmetric, material) stretch tensor and $\boldsymbol{v}$ the left (symmetric, spatial) stretch tensor. $\boldsymbol{R}$ is an orthonormal tensor of rotation. This decomposition shows that when deformation occurs, both elongation and rotation occur.

3.3 Nansons Formula

To map a unit vector normal to an infinitesimal material surface element to a unit vector normal to an infinitesimal spatial surface element the deformation gradient cannot be used [22]. Instead a useful relationship called the Nanson's formula is used. The formula is defined as:

$$d\boldsymbol{s} = J\boldsymbol{F}^{-\boldsymbol{T}}d\boldsymbol{S} \quad \textbf{(3-9)}$$

Where

$$d\boldsymbol{s} = ds\boldsymbol{n} \quad \textbf{(3-10)}$$

$$d\boldsymbol{S} = dS\boldsymbol{N} \quad \textbf{(3-11)}$$

and ds and dS are the material and spatial surface elements, and **n** and **N** are the unit vectors normal to the surfaces.

Nansons formula has use during the derivation of different types of stress tensors.

3.4 Cauchy-Green deformation tensors

As well as the deformation gradient, other deformation measures and strain tensors are used. A good starting point is the product of the deformation gradient with the transpose of itself $\boldsymbol{F^T F}$.

From here two deformation tensors can be derived, the right Cauchy-Green tensor

$$\boldsymbol{C = F^T F = C^T} \tag{3-12}$$

and the left Cauchy-Green tensor

$$\boldsymbol{b = F F^T} \tag{3-13}$$

The right Cauchy-Green tensor, $\boldsymbol{C}$**,** represents the change in squared length of the element dX and is defined with respect to the reference configuration. The left Cauchy-Green tensor, $\boldsymbol{b}$**,** represents the change in squared length of the element dx and is defined with respect to the current configuration.

The deformation tensors 3.12 and 3.13 can be linked to the stretch tensors $\boldsymbol{U}$ and $\boldsymbol{v}$ arising during the polar decomposition of the deformation gradient. The stretch tensors are related to the Cauchy-Green deformation tensors via equations (3-14) and (3-15)

$$\boldsymbol{C = F^T F = U^2} \tag{3-14}$$

$$\boldsymbol{b = F F^T = v^2} \tag{3-15}$$

The Cauchy-Green deformation tensors are useful measures, however in the un-deformed configuration, equations (3-12) and (3-13) reduce to identity. More

usefully, they can be used to derive strain tensors which reduce to zero in the un-deformed configuration, making the constitutive equations less complicated.

3.5 Green-Lagrange strain tensor

The strain measured in terms of material variables can be expressed by the Green-Lagrange strain tensor

$$\boldsymbol{E} = \frac{1}{2}(\boldsymbol{F^T F} - \mathbf{1}) \tag{3-16}$$

The Green-Lagrange strain can be related to the Cauchy-Green deformation tensors and the elongation tensor by substituting equation (3-14) into equation (3-16) giving

$$\boldsymbol{E} = \frac{1}{2}(\boldsymbol{C} - 1) = \frac{1}{2}(\boldsymbol{U}^2 - 1) \tag{3-17}$$

3.6 Euler-Almansi strain tensor

When the squared lengths are measured in terms of spatial variables, the resulting strain tensor is the Euler-Almansi tensor.

$$\boldsymbol{\varepsilon} = \frac{1}{2}(1 - \boldsymbol{F^{-T} F^{-1}}) \tag{3-18}$$

The Euler-Almansi tensor can be related to the left Cauchy-Green tensor and the stretch tensor by substituting equations (3-12) and (3-13) into equation (3-18).

$$\boldsymbol{\varepsilon} = \frac{1}{2}(1 - \boldsymbol{b^{-1}}) = \frac{1}{2}(1 - (\boldsymbol{v^{-1}})^{\mathbf{2}}) \tag{3-19}$$

The Green-Lagrange and Euler-Almansi strain tensors are linked by relation (3-20)

$$\boldsymbol{E} = \frac{1}{2}(\boldsymbol{F^T F} - 1) = \boldsymbol{F^T}\frac{1}{2}(1 - \boldsymbol{F^{-T} F^{-1}})\boldsymbol{F} = \boldsymbol{F^T \varepsilon F} \tag{3-20}$$

3.7 Deformation rate measures

Taking the first derivative of the position vector $\boldsymbol{x}$ in the spatial description results in the spatial velocity. By taking the derivative of this with respect to the spatial coordinates yields the spatial velocity gradient:

$$\boldsymbol{l}(\boldsymbol{x},t) = \frac{\partial \boldsymbol{v}(\boldsymbol{x},t)}{\partial \boldsymbol{x}} = grad\boldsymbol{v}(\boldsymbol{x},t) \tag{3-21}$$

By putting the spatial velocity in terms of the motion, and then applying the chain rule, the spatial velocity gradient can be shown in terms of the deformation gradient

$$\boldsymbol{l} = \dot{\boldsymbol{F}}\boldsymbol{F}^{-1} \tag{3-22}$$

Importantly, the spatial velocity gradient can be additively decomposed as in equation (3-23).

$$\boldsymbol{l}(\boldsymbol{x},t) = \boldsymbol{d}(\boldsymbol{x},t) + \boldsymbol{w}(\boldsymbol{x},t) \tag{3-23}$$

Where

$$\boldsymbol{d}(\boldsymbol{x},t) = \frac{1}{2}(\boldsymbol{l} + \boldsymbol{l}^{\boldsymbol{T}}) \tag{3-24}$$

$$\boldsymbol{w}(\boldsymbol{x},t) = \frac{1}{2}(\boldsymbol{l} - \boldsymbol{l}^{\boldsymbol{T}}) \tag{3-25}$$

The tensors $\boldsymbol{d}$ and $\boldsymbol{w}$ are the symmetric and skew-symmetric parts of the spatial velocity gradient respectively. The symmetric part, $\boldsymbol{d}$, is referred to as the rate of deformation tensor and the skew-symmetric part, $\boldsymbol{w}$, is the rate of rotation tensor.

Similarly the material velocity gradient can be obtained by taking the material time derivative of the deformation gradient

$$\dot{\boldsymbol{F}} = \frac{\partial}{\partial t}\left(\frac{\partial \boldsymbol{\chi}(\boldsymbol{X},t)}{\partial \boldsymbol{X}}\right) = \frac{\partial}{\partial \boldsymbol{X}}\left(\frac{\partial \boldsymbol{\chi}(\boldsymbol{X},t)}{\partial t}\right) = \frac{\partial \boldsymbol{V}(\boldsymbol{X},t)}{\partial \boldsymbol{X}} = Grad\boldsymbol{V}(\boldsymbol{X},t) \tag{3-26}$$

3.8 Intermediate and isoclinic configurations

As a load is applied to the materials of interest is this work, deformation occurs. Three main types of deformation occur in metals; elastic deformation, plastic deformation and damage. Elastic deformation forms the Hooke's law region of a stress-strain plot, which for a metal is a straight line region with the strain being directly proportional to the stress. Plastic deformation occurs when the applied stress reached the yield point of the material. For a metal this is observed to be the point on a stress-strain plot where the straight line region ends and a curve begins to develop. Upon unloading, the plastic deformation will remain in the material. An important property of plastic deformation is that it does not affect the elastic properties of the material.

Damage is similar to plastic deformation as it is an irreversible process; however it is characterised by the formation of micro cracks and micro voids. Unlike plastic deformation, damage affects the elastic properties of the material.

In a real, physical experiment, each of these three types of deformation will be observed simultaneously. When modelling the deformations however, it is convenient to consider each type separately. In reality this is not achievable, i.e. a material cannot undergo plastic deformation without some degree of elastic deformation. For the purpose of modelling this as three separate processes the concept of multiplicatively decomposing the deformation gradient as well as intermediate configurations need to be introduced.

Equation (3-27) shows how the deformation gradient is decomposed as presented in [23].

$$\boldsymbol{F} = \frac{\partial \boldsymbol{x}}{\partial \boldsymbol{X}} = \frac{\partial \boldsymbol{x}}{\partial \boldsymbol{x}_{pd}} \frac{\partial \boldsymbol{x}_{\boldsymbol{pd}}}{\partial \boldsymbol{X}} = \boldsymbol{F}_e \boldsymbol{F}_{\boldsymbol{pd}} \tag{3-27}$$

Where $\boldsymbol{F}_e$ is the elastic part of the deformation gradient, $\boldsymbol{F}_{pd}$ is the inelastic part of the deformation gradient.

Making use of the multiplicatively decomposed deformation gradient, an intermediate configuration becomes apparent when considering a deformation.

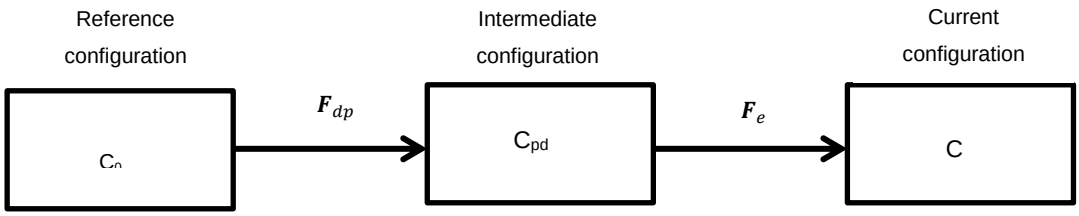

Figure 3-1: Link between reference, intermediate and current configurations.

It is usual to map between the initial and current configurations, however to reach the current configuration all types of deformation need to be included. Considering the decomposition in equation (3-27), a two stage deformation process can be written as shown in Figure 3-1.

Figure 3-1 shows three configurations: the initial configuration, C_0, the current configuration, C, and an intermediate configuration, C_{pd}. The initial and current configurations are as described previously in section 3-1, and the intermediate configuration is caused due to the consideration of the deformation processes separately. The intermediate configuration shown in Figure 3-1 can be considered as an elastically released configuration; only plastic deformation and damage are present.

The deformation gradient can be decomposed into stretch and rotational parts, as sown previously in section 3.2. The same decomposition can be applied to the multiplicatively decomposed deformation gradient resulting in a rigid body rotation associated with each stage of the deformation. Due to this, the elastically released intermediate configuration is not uniquely defined. This is overcome by introducing the isoclinic configuration. The isoclinic configuration is the same as the elastically released intermediate configuration, with the rigid body rotation caused by deformation removed so that it is orientated the same as the initial configuration. Physically, the isoclinic configuration is not achievable but it is a very useful concept for modelling as it is uniquely defined.

Figure 3-2 shows the relationship between the initial configuration, the elastically released intermediate configuration, the current configuration and the isoclinic configuration, $\tilde{C}_{dp}$.

The isoclinic configuration is the main configuration used in the derivation of the material model developed by Djordjevic as it the different deformation processes can be treated separately.

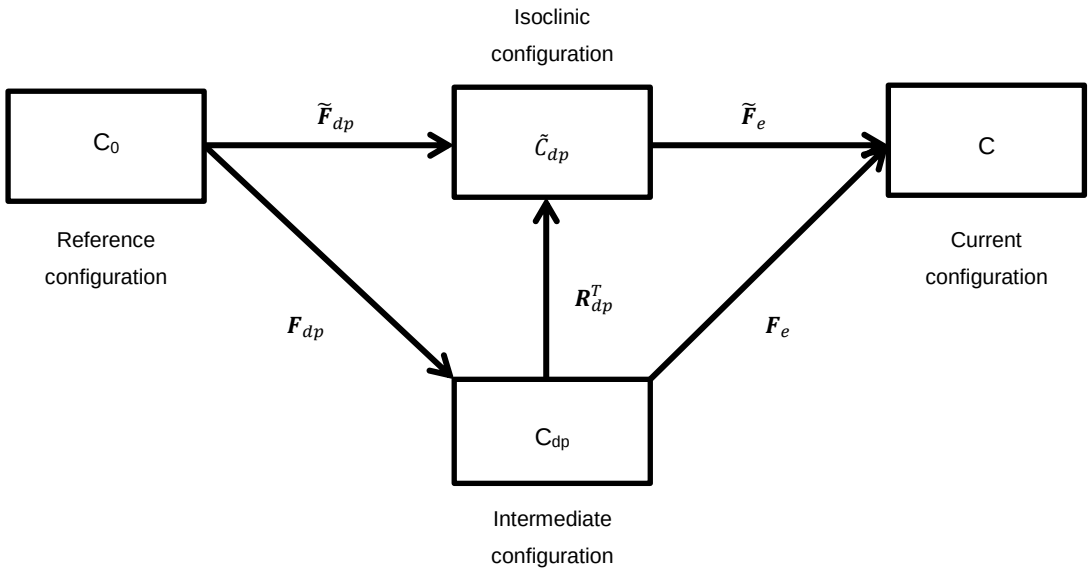

Figure 3-2: Links between the reference, intermediate, isoclinic and current configurations, with C_0 the reference configuration, C_{dp} the intermediate configuration, C the current configuration and $\widetilde{\boldsymbol{C}}_{\boldsymbol{dp}}$ the isoclinic configuration. The deformation gradient labels are as outline in equation (3-27), with $\widetilde{\boldsymbol{F}}_{\boldsymbol{dp}}$ and $\widetilde{\boldsymbol{F}}_{\boldsymbol{e}}$ the inelastic and elastic parts of the deformation gradient defined with respect to the isoclinic configuration and $\boldsymbol{R}_{\boldsymbol{dp}}^{\boldsymbol{T}}$ is the removal of the rigid body rotation caused during deformation.

3.9 Stress

Stress in a continuum can be described by considering the forces on an infinitesimal surface element on an imaginary plane cutting through the continuum. The force on the infinitesimal surface area, ds, is described by a traction vector, $\boldsymbol{t}$. The traction vector represents the force per unit area with the same direction as the force is acting. Stress tensor arise from this due to Cauchy's stress theorem which states: "there exist unique second-order tensor fields $\boldsymbol{\sigma}$ and $\boldsymbol{P}$ so that

$$\boldsymbol{t}(\boldsymbol{x}, t, \boldsymbol{n}) = \boldsymbol{\sigma}(\boldsymbol{x}, t)\boldsymbol{n} \quad \textbf{(3-28)}$$

$$\boldsymbol{T}(\boldsymbol{X}, t, \boldsymbol{N}) = \boldsymbol{P}(\boldsymbol{X}, t)\boldsymbol{N} \quad \textbf{(3-29)}$$

Where $\boldsymbol{\sigma}$ denotes a symmetric spatial tensor field called the Cauchy stress tensor, while $\boldsymbol{P}$ characterizes a tensor field called the first Piola-Kirchhoff stress tensor" [22]. It should be noted that the traction vector $\boldsymbol{t}$ is representative of the surface tractions in the current configuration, whereas $\boldsymbol{T}$ is a function of the referential configuration.

The Cauchy stress and the first Piola-Kirchhoff stress are related by equation (3-30).

$$\boldsymbol{\sigma} = J^{-1}\boldsymbol{P}\boldsymbol{F}^{\boldsymbol{T}} \quad \textbf{(3-30)}$$

There are many other stress tensors that have been defined in literature, of which two find use within the Cranfield model; these are the so called second Piola-Kirchhoff stress and the Mandel stress.

The second Piola-Kirchhoff stress is defined by the pull-back operation on the contravarient spatial tensor field, known as the Kirchhoff stress. The Kirchhoff stress is given as

$$\boldsymbol{\tau} = J\boldsymbol{\sigma} \quad \textbf{(3-31)}$$

Where J is the volume ratio and σ is the Cauchy stress tensor.

The second Piola-Kirchhoff stress tensor is now defined as

$$\boldsymbol{S} = \boldsymbol{\chi}_*^{-1}(\boldsymbol{\tau}^{\#}) = \boldsymbol{F}^{-1}\boldsymbol{\tau}\boldsymbol{F}^{-T} \quad \textbf{(3-32)}$$

The subscript $*$ and superscript # in equation (3-32) represent that the second Piola-Kirchhoff stress is achieved by a pull-back operation of the contravarient spatial tensor field.

From the definition of the Kirchhoff stress, equation (3-31), and the relation between the first Piola-Kirchhoff stress and the Cauchy stress, equation (3-30),

the second Piola-Kirchhoff stress can be expressed in terms of the Cauchy stress and the first Piola-Kirchhoff stress tensors:

$$\boldsymbol{S} = J\boldsymbol{F}^{-1}\boldsymbol{\sigma}\boldsymbol{F}^{-T} = \boldsymbol{F}^{-1}\boldsymbol{P} \tag{3-33}$$

The Mandel stress is a stress tensor which is defined with respect to an intermediate configuration. In the case of the Cranfield model the Mandel stress tensor is defined separately in both the intermediate and isoclinic configurations. It is shown in [23] that the Mandel stress is given in the intermediate configuration in terms of Kirchhoff stress and the second Piola-Kirchhoff stress tensor as:

$$\widetilde{\boldsymbol{\Sigma}} = \boldsymbol{F}_e^{-1}\boldsymbol{\tau}\boldsymbol{F}_e^{-T} = \widetilde{\boldsymbol{C}}_e\widetilde{\boldsymbol{S}} \tag{3-34}$$

And in the isoclinic configuration as:

$$\overline{\boldsymbol{\Sigma}} = \overline{\boldsymbol{F}}_{ed}^{-1}\boldsymbol{\tau}\overline{\boldsymbol{F}}_{ed}^{-T} = \overline{\boldsymbol{C}}_e\overline{\boldsymbol{S}} \qquad \overline{\boldsymbol{\Sigma}} = \overline{\boldsymbol{F}}_{ed}^{T}\boldsymbol{\tau}\overline{\boldsymbol{F}}_{ed}^{-T} = \overline{\boldsymbol{C}}_e\overline{\boldsymbol{S}} \tag{3-35}$$

A relationship exists between the Mandel stress in the intermediate configuration and the Mandel stress in the isoclinic configuration, which is determined by the inelastically induced rotation $\boldsymbol{R}_{dp}$ as:

$$\overline{\boldsymbol{\Sigma}} = \boldsymbol{R}_{dp}^{T}\widetilde{\boldsymbol{\Sigma}}\boldsymbol{R}_{dp} \tag{3-36}$$

In general, the Mandel stress is asymmetric. However, for a model modelling small elastic but large plastic deformation, a behaviour which is observable with most metals, the Mandel stress becomes symmetric.

3.10 Summary

The basic measures of deformation, including the deformation gradient, stretch, strain and stress, have been presented along with the key deformation rate measures required for modelling. Important decompositions of the deformation measures are made which allow for definition of the intermediate and isoclinic configurations, the latter of which is one of the key aspects of the current Cranfield model.

4 Relevant thermodynamics

It is important to include thermodynamics in a material model, as under deformation, heat is generated in the material. This heat is caused by energy dissipation during deformation, and when conserving energy it must be accounted for. Therefore thermodynamics needs careful consideration in modelling.

This section outlines the main principles of the thermodynamics used when the Cranfield model was derived by Djordjevic [23]. It covers the principle laws of thermodynamics, thermodynamic potentials and the method of dealing with real irreversible processes.

4.1 The 1st Law

The type of thermodynamic system in which the model is assumed to be is a closed system. This implies means that only energy, and not mass, can be exchanged [24]. The first law of thermodynamics is a balance in energy, and states that the change in internal energy is equal to the heat added to the system minus the work done by the system. Mathematically the first law is defined as:

$$\Delta U = Q - W \tag{4-1}$$

Where ΔU is the change in internal energy of the system, Q is the heat added to the system and W is the work done by the system. When considering a continuum approach, the first law or balance in energy is defined in the current configuration as:

$$\dot{E}_{tot} = \frac{D}{Dt}\mathrm{K} + P_{int} + Q_{input} = \frac{D}{Dt}\mathrm{K} + \frac{D}{Dt}U = \dot{\mathrm{K}} + \dot{U} \tag{4-2}$$

Where K is the kinetic energy of the continuum, P_{int} is the stress power, Q_{input} is the heat input to the system and U is the internal energy of the continuum.

4.2 The 2nd Law

The second law of thermodynamics states that “the entropy change of any system and its surroundings, considered together, is positive and approached zero for any process which approaches reversibility” [24]. As real processes in nature are irreversible, the change in entropy is always positive; entropy is always produced.

The mathematical formulation of the second law is:

$$\frac{DS}{Dt} - Q'_{input} \geq 0 \tag{4-3}$$

This inequality can be transformed into the Clausius-Duhem inequality by making the assumption that the entropy production is proportional to the heat flux and the heat source by the same factor, θ^{-1} [23], giving:

$$\frac{D}{Dt}\int_{\Omega} s\rho dv \geq \int_{\Omega} \frac{r}{\theta}\rho dv + \int_{\partial\Omega} -\frac{\boldsymbol{q}}{\theta}.\boldsymbol{n}ds \tag{4-4}$$

Application of the divergence theorem to equation (4-4) leads to the Clausius-Duhem inequality in local form:

$$\dot{s} \geq \frac{r}{\theta} - \frac{1}{q}\nabla.\frac{\boldsymbol{q}}{\theta} \tag{4-5}$$

The second law of thermodynamics shows that entropy is produced in an irreversible process, which real physical systems are. However it does not quantify the entropy production. The energy dissipated during inelastic deformation can be quantified by making use of the second law. By combining the first and second laws in the local form, the internal dissipation per unit volume was derived as equation (4-6)

$$\rho\theta\dot{s} - (\rho\dot{u} - \boldsymbol{\sigma}:\boldsymbol{d}) - \frac{1}{\theta}\boldsymbol{q}.\nabla\theta \geq 0 \tag{4-6}$$

Where

$$\rho\theta\dot{s} - \rho\dot{u} + \boldsymbol{\sigma}:\boldsymbol{d} = \Delta \tag{4-7}$$

The first law was applied to the internal dissipation resulting in the dissipation being written in terms of entropy production and heat fluxes. As the impacts of interest in the Cranfield model are of high velocities and strain rates, it is assumed the deformation process is adiabatic; heat does not flow, it causes a local temperature change. The dissipation therefore only consists of the adiabatic terms shown in equation (4-8).

$$\Delta_{ad} = \rho\theta\dot{s} \quad \textbf{(4-8)}$$

4.3 Irreversible thermodynamics with internal variables

The second law of thermodynamics shows that entropy is produced in a real irreversible system. However, due to it being an inequality it does not quantify the entropy produced. Due to this, a number of theories of irreversible thermodynamics have been developed. The theory used by Djordjevic in the development of the Cranfield model is the theory of irreversible thermodynamics with internal variables. The theory uses internal variables to describe the state of the system by assuming the existence of two types of thermodynamic potentials; state potentials and dissipation potentials.

Irreversible thermodynamics with internal variables makes use of the principle of equipresence; which states that if an independent variable is present in one constitutive equation then it must be present in all constitutive equations.

4.4 Thermodynamic potentials

There are four state potentials that are relevant for use in the theory of irreversible thermodynamics with internal variables.

These are:

- Internal energy, U
- Helmholtz free energy, ψ
- Gibbs free energy, g
- Enthalpy, h

These potentials express the energy of a system as state functions, assuming energy variation is path independent, depending only on the initial and final

states. The four potentials presented each represent the energy of the system, but displays it in terms of different variables which are more convenient to work with, depending on the situations being considered.

4.4.1 Internal energy

The internal energy of a system is the sum of the energy of all internal degrees of freedom. The internal energy is well defined for all equilibrium states of a system, however it is not directly measureable [25]. Instead, the first law is used to measure the change of internal energy as shown in section 4.1. In a differential form, equation (4-9), the first law implies that the change in internal energy is dependent on the change in entropy and the change in volume; therefore it can be concluded that the internal energy is a function of the entropy and volume.

$$dU = \theta ds - \boldsymbol{S} dV \tag{4-9}$$

In the reference configuration, the internal energy is shown in [23] to be in terms of the elastic strain and the temperature as:

$$\dot{U} = \left(\frac{\partial U}{\partial \boldsymbol{E}}\right) : \dot{\boldsymbol{E}} + \left(\frac{\partial U}{\partial s}\right) \dot{s} \tag{4-10}$$

Where

$$\left(\frac{\partial U}{\partial \boldsymbol{E}}\right) = \boldsymbol{S} \tag{4-11}$$

$$\left(\frac{\partial U}{\partial s}\right) = \theta \tag{4-12}$$

Often it is not convenient to work in the natural variables of entropy and strain; it can be more convenient to work with other natural variables. This can be achieved by applying Legrendre transforms to the internal energy.

4.4.2 Helmholtz Free energy function

The Helmholtz free energy is defined mathematically as:

$$\psi(\boldsymbol{E}, \theta) = U(\boldsymbol{E}, s) - \theta s \tag{4-13}$$

This expression is obtained by using equation (4-12) and applying a Legendre transform [23], resulting in the function being expressed in terms of the strain and temperature. Due to this, the Helmholtz free energy is a strain energy function, which is used in the current formulation of the Cranfield model.

The time derivative of the Helmholtz free energy is expressed as:

$$\dot{\psi}(\boldsymbol{E},\theta) = \dot{U}(\boldsymbol{E},s) - \dot{\theta}s - \theta\dot{s} = \boldsymbol{S}:\dot{\boldsymbol{E}} - s\dot{\theta} \tag{4-14}$$

Which gives rise to the relations:

$$\boldsymbol{S} = \left(\frac{\partial\psi}{\partial\boldsymbol{E}}\right)_{\boldsymbol{\theta}} \tag{4-15}$$

$$s = -\left(\frac{\partial\psi}{\partial\theta}\right)_{\boldsymbol{E}} \tag{4-16}$$

4.4.3 Gibbs free energy

An alternative potential is the Gibbs free energy. This is obtained by making use of equation (4-15) and applying a Legendre transformation. This results in a mathematical definition of the Gibbs free energy, which has stress and temperature as natural variables [25], as:

$$g(\boldsymbol{S},\theta) = \psi(\boldsymbol{E},\theta) - \boldsymbol{S}:\boldsymbol{E} \tag{4-17}$$

Similar to the Helmholtz free energy, the time derivative is taken of the Gibbs free energy to give a pair of constitutive equations. The time derivative is:

$$\dot{g}(\boldsymbol{S},\theta) = \dot{\psi}(\boldsymbol{E},\theta) - \boldsymbol{S}:\dot{\boldsymbol{E}} - \dot{\boldsymbol{S}}:\boldsymbol{E} = -\dot{\boldsymbol{S}}:\boldsymbol{E} - \boldsymbol{s}\dot{\theta} \tag{4-18}$$

From which the pair of constitutive equations are given as:

$$\boldsymbol{E} = -\left(\frac{\partial g}{\partial\boldsymbol{S}}\right)_{\boldsymbol{\theta}} \tag{4-19}$$

$$s = -\left(\frac{\partial g}{\partial\theta}\right)_{\boldsymbol{S}} \tag{4-20}$$

4.4.4 Enthalpy

The final commonly used thermodynamic potential is enthalpy and is a function of the stress and entropy. The definition of enthalpy is obtained by applying a Legendre transformation to equation (4-11) which yields:

$$h(\boldsymbol{S}, s) = U(\boldsymbol{E}, s) - \boldsymbol{S}:\boldsymbol{E} \tag{4-21}$$

As with the Helmholtz and Gibbs free energies, the time derivative of the enthalpy is taken which yields a pair of constitutive equations. The time derivative is given as:

$$\dot{h}(\boldsymbol{S}, s) = \dot{U}(\boldsymbol{E}, s) - \dot{\boldsymbol{S}}:\boldsymbol{E} - \boldsymbol{S}:\dot{\boldsymbol{E}} = -\dot{\boldsymbol{S}}:\boldsymbol{E} + \theta\dot{s} \tag{4-22}$$

The pair of constitutive equations provides relationships for the strain and the temperature:

$$\boldsymbol{E} = -\left(\frac{\partial h}{\partial \boldsymbol{S}}\right)_{\boldsymbol{s}} \tag{4-23}$$

$$\theta = \left(\frac{\partial h}{\partial s}\right)_{\boldsymbol{S}} \tag{4-24}$$

The four potentials are related to each other via equation (4-25)

$$g = U - \theta s - \boldsymbol{S}:\boldsymbol{E} = \psi - \boldsymbol{S}:\boldsymbol{E} = h - \theta s \tag{4-25}$$

4.5 Summary

The important laws of thermodynamics, including the first two laws, which are required when considering the balance of energy during modelling have been introduced. The laws introduced are in the form used in [23] during the development of the Cranfield model.

The theory of irreversible thermodynamics with internal variables, used in [23] has been introduced. This is one of the key concepts as the use of internal variables is an important concept in the Cranfield model.

The more commonly used thermodynamic potentials have been introduced in the form of the internal energy, the Helmholtz free energy, the Gibbs free

energy and Enthalpy. It will be seen in the following chapter that the Helmholtz free energy is used extensively in the hyperelastic part of the model, forming the basis of it.

5 Cranfield model

This chapter introduces the current formulation of the Cranfield model. The first three sections discuss the formulations for the elastic behaviour representation, the damage representation and finally the plastic deformation representation. The current formulation pulls together the concepts discussed in the previous two chapters resulting in the thermodynamically consistent continuum model. The shock wave modelling capability of the model is discussed, with the area requiring improvement being highlighted. The chapter is concluded with a summary.

5.1 Elastic behaviour representation

Elastic behaviour is modelled based on the assumption that the material is hyperelastic and with the use of the free energy function, the stress tensor and the stiffness tensor.

The Helmholtz free energy function is used in the elastic part of the model. The function is written in terms of an irreducible set of invariants which are given in terms of structural tensors and the elastic Green-Lagrange strain. The function is written in this form as it must be invariant to rigid body rotation; this condition is satisfied when written in terms of a set of irreducible invariants, J_1 to J_7. The set of irreducible invariants used for the formulation of the hyperelastic response are given in [23] as:

$$J_1 = \mathbf{1}:\bar{\boldsymbol{E}}_{\boldsymbol{e}} \qquad J_2 = \mathbf{1}:\bar{\boldsymbol{E}}_{\boldsymbol{e}}^{\mathbf{2}}$$

$$\boldsymbol{J_3 = \mathbf{1}:\bar{E}_e^3}$$

(5-1)

$$\boldsymbol{J_4 = \mathbf{1}:(\bar{M}^1\bar{E}_e)} \qquad J_5 = \mathbf{1}:(\bar{\boldsymbol{M}}^{\mathbf{1}}\bar{\boldsymbol{E}}_{\boldsymbol{e}}^{\mathbf{2}})$$

$$J_6 = \mathbf{1}:(\bar{\boldsymbol{M}}^{\mathbf{2}}\bar{\boldsymbol{E}}_{\boldsymbol{e}}) \qquad J_7 = \mathbf{1}:(\bar{\boldsymbol{M}}^{\mathbf{2}}\bar{\boldsymbol{E}}_{\boldsymbol{e}}^{\mathbf{2}})$$

Making use of the irreducible set of invariants, the Helmholtz free energy function is written in a quadratic form:

$$\bar{\boldsymbol{\psi}}(\boldsymbol{E_e}, \bar{\boldsymbol{M}}^{\boldsymbol{1}}, \bar{\boldsymbol{M}}^{\boldsymbol{2}}, \boldsymbol{\theta}) = \frac{1}{2}\boldsymbol{\alpha}_1 J_1^2 + \boldsymbol{\alpha}_2 J_2 + \frac{1}{2}\boldsymbol{\alpha}_3 J_4^2 + \boldsymbol{\alpha}_4 J_5 + \frac{1}{2}\boldsymbol{\alpha}_5 J_6^2 + \boldsymbol{\alpha}_6 J_7 + \boldsymbol{\alpha}_7 J_1 J_4 + \boldsymbol{\alpha}_8 J_1 J_6 + \boldsymbol{\alpha}_9 J_4 J_6 \quad \textbf{(5-2)}$$

The constants, $\boldsymbol{\alpha_1}$ to $\boldsymbol{\alpha}_9$ are material constants which are linearly independent and are required for modelling orthotropic materials, $J_1$to J_7 are invariants of the strain tensor and $\bar{\boldsymbol{M}}^1$ and $\bar{\boldsymbol{M}}^2$ are structural tensors required due to the orthotropic material. The structural tensors are given in the reference configuration as:

$$\boldsymbol{M^1} = \begin{bmatrix} 1 & 0 & 0 \\ 0 & 0 & 0 \\ 0 & 0 & 0 \end{bmatrix} \quad \textbf{(5-3)}$$

$$\boldsymbol{M^2} = \begin{bmatrix} 0 & 0 & 0 \\ 0 & 1 & 0 \\ 0 & 0 & 0 \end{bmatrix} \quad \textbf{(5-4)}$$

In the isoclinic configuration the structural tensors are shown in [23] to be given by the relation:

$$\bar{\boldsymbol{M}}^i = \bar{\boldsymbol{F}}_p \boldsymbol{M}^i \bar{\boldsymbol{F}}_p^{-1} \quad \textbf{(5-5)}$$

The stress tensor used for the elastic part of the model was obtained by taking the derivative of the Helmholtz function with respect to the elastic part of the Green-Lagrange strain

$$\bar{\boldsymbol{S}} = \frac{\partial \bar{\boldsymbol{\psi}}}{\partial \bar{\boldsymbol{E}}_e} = \boldsymbol{\alpha}_1 J_1 \frac{\partial J_1}{\partial \bar{\boldsymbol{E}}_e} + \boldsymbol{\alpha}_2 \frac{\partial J_2}{\partial \bar{\boldsymbol{E}}_e} + \boldsymbol{\alpha}_3 J_4 \frac{\partial J_4}{\partial \bar{\boldsymbol{E}}_e} + \boldsymbol{\alpha}_4 \frac{\partial J_5}{\partial \bar{\boldsymbol{E}}_e} + \boldsymbol{\alpha}_5 J_6 \frac{\partial J_6}{\partial \bar{\boldsymbol{E}}_e} + \boldsymbol{\alpha}_6 \frac{\partial J_7}{\partial \bar{\boldsymbol{E}}_e} + \boldsymbol{\alpha}_7 J_4 \frac{\partial J_1}{\partial \bar{\boldsymbol{E}}_e} + \boldsymbol{\alpha}_7 J_1 \frac{\partial J_4}{\partial \bar{\boldsymbol{E}}_e} + \boldsymbol{\alpha}_8 J_6 \frac{\partial J_1}{\partial \bar{\boldsymbol{E}}_e} + \boldsymbol{\alpha}_8 J_1 \frac{\partial J_6}{\partial \bar{\boldsymbol{E}}_e} + \boldsymbol{\alpha}_9 J_6 \frac{\partial J_4}{\partial \bar{\boldsymbol{E}}_e} + \boldsymbol{\alpha}_9 J_4 \frac{\partial J_6}{\partial \bar{\boldsymbol{E}}_e} \quad \textbf{(5-6)}$$

The derivatives in equation (5-6) are calculated in the work of Djordjevic and were found in terms of structural tensors and the elastic part of the Green-Lagrange strain. When substituted into equation (5-6) the stress tensor becomes:

$$\begin{aligned}\bar{\boldsymbol{S}} = {} & \boldsymbol{\alpha}_1(\mathbf{1}:\bar{\boldsymbol{E}}_{\boldsymbol{e}})\mathbf{1} + 2\boldsymbol{\alpha}_2\bar{\boldsymbol{E}}_{\boldsymbol{e}} + \boldsymbol{\alpha}_3\left(\mathbf{1}:(\bar{\boldsymbol{M}}^{\mathbf{1}}\bar{\boldsymbol{E}}_{\boldsymbol{e}})\right)\bar{\boldsymbol{M}}^{\mathbf{1}} + \boldsymbol{\alpha}_4(\bar{\boldsymbol{M}}^{\mathbf{1}}\bar{\boldsymbol{E}}_{\boldsymbol{e}} + \bar{\boldsymbol{E}}_{\boldsymbol{e}}\bar{\boldsymbol{M}}^{\mathbf{1}}) \\ & + \boldsymbol{\alpha}_5\left(\mathbf{1}:(\bar{\boldsymbol{M}}^{\mathbf{2}}\bar{\boldsymbol{E}}_{\boldsymbol{e}})\right)\bar{\boldsymbol{M}}^{\mathbf{2}} + \boldsymbol{\alpha}_6(\bar{\boldsymbol{M}}^{\mathbf{2}}\bar{\boldsymbol{E}}_{\boldsymbol{e}} + \bar{\boldsymbol{E}}_{\boldsymbol{e}}\bar{\boldsymbol{M}}^{\mathbf{2}}) + \boldsymbol{\alpha}_7(\mathbf{1}:\bar{\boldsymbol{M}}^{\mathbf{1}}\bar{\boldsymbol{E}}_{\boldsymbol{e}})\mathbf{1} \\ & + \boldsymbol{\alpha}_7(\mathbf{1}:\bar{\boldsymbol{E}}_{\boldsymbol{e}})\bar{\boldsymbol{M}}^{\mathbf{1}} + \boldsymbol{\alpha}_8(\mathbf{1}:\bar{\boldsymbol{M}}^{\mathbf{2}}\bar{\boldsymbol{E}}_{\boldsymbol{e}})\mathbf{1} + \boldsymbol{\alpha}_8(\mathbf{1}:\bar{\boldsymbol{E}}_{\boldsymbol{e}})\bar{\boldsymbol{M}}^{\mathbf{2}} \\ & + \boldsymbol{\alpha}_9(\mathbf{1}:\bar{\boldsymbol{M}}^{\mathbf{2}}\bar{\boldsymbol{E}}_{\boldsymbol{e}})\bar{\boldsymbol{M}}^{\mathbf{1}} + \boldsymbol{\alpha}_9(\mathbf{1}:\bar{\boldsymbol{M}}^{\mathbf{1}}\bar{\boldsymbol{E}}_{\boldsymbol{e}})\bar{\boldsymbol{M}}^{\mathbf{2}}\end{aligned} \tag{5-7}$$

The stiffness tensor is found by taking the derivative of the stress with respect to the elastic part of the strain. With the derivatives substituted in, the stiffness tensor is given by:

$$\begin{aligned}\bar{\mathbb{C}} = {} & \boldsymbol{\alpha}_1\mathbf{1}\otimes\mathbf{1} + \mathbf{2}\boldsymbol{\alpha}_2\mathbb{I} + \boldsymbol{\alpha}_3\bar{\boldsymbol{M}}^{\mathbf{1}}\otimes\bar{\boldsymbol{M}}^{\mathbf{1}} + \boldsymbol{\alpha}_5\bar{\boldsymbol{M}}^{\mathbf{2}}\otimes\bar{\boldsymbol{M}}^{\mathbf{2}} + \boldsymbol{\alpha}_4\mathbb{F}^{\mathbf{1}} + \boldsymbol{\alpha}_6\mathbb{F}^{\mathbf{2}} \\ & + \boldsymbol{\alpha}_7(\mathbf{1}\otimes\bar{\boldsymbol{M}}^{\mathbf{1}} + \bar{\boldsymbol{M}}^{\mathbf{1}}\otimes\mathbf{1}) + \boldsymbol{\alpha}_8(\mathbf{1}\otimes\bar{\boldsymbol{M}}^{\mathbf{2}} + \bar{\boldsymbol{M}}^{\mathbf{2}}\otimes\mathbf{1}) \\ & + \boldsymbol{\alpha}_9(\bar{\boldsymbol{M}}^{\mathbf{1}}\otimes\bar{\boldsymbol{M}}^{\mathbf{2}} + \bar{\boldsymbol{M}}^{\mathbf{2}}\otimes\bar{\boldsymbol{M}}^{\mathbf{1}})\end{aligned} \tag{5-8}$$

The stress and strain tensors are symmetric, therefore the stiffness tensor can be written in Voigt notation. Due to this, it is observed that the hyperelastic response of orthotropic materials is determined by nine coefficients, α_1 to α_9 or the nine coefficients from the stiffness tensor in matrix form, c_{11} to c_{66}. As the coefficients are representing the same response, the two sets of coefficients can be expressed in terms of each other.

The three equations 5.5, 5.7 and 5.8 determine the constitutive model for hyperelastic response [23].

5.2 Damage representation

The damage part of the Cranfield model is defined in terms of the damage part of the velocity gradient, a damage potential, which is introduced in this section and evolution equations.

Prior to defining a damage potential the concepts of the damage tensor and the damage energy release rate need to be defined.

The damage tensor, $\bar{\boldsymbol{\omega}}$, is an alternative tensor that can be used to describe the mapping of an effective area vector in the isoclinic configuration to a similar area vector in the elastically unloaded intermediate configuration [23]. Instead of using Nanson's formula, instead equation (5-9) can be used, making use of, and defining the damage tensor.

$$d\boldsymbol{s}_{dp}^{n} = (\mathbf{1} - \bar{\boldsymbol{\omega}})^{-1} d\boldsymbol{S}_1 \tag{5-9}$$

$(\mathbf{1} - \bar{\boldsymbol{\omega}})$ is referred to as the integrity tensor.

The damage energy release rate arises from the damage part of dissipation, and is defined as:

$$\overline{\boldsymbol{Y}} = -[\mathbf{1} - \bar{\boldsymbol{\omega}}]\overline{\boldsymbol{S}} \tag{5-10}$$

Similar to the Helmholtz free energy potential used in the elastic part of the model, a damage potential is defined. The damage pseudo potential derived in [23] is defined in terms of a set of irreducible invariants of $\overline{\boldsymbol{Y}}$ and structural tensors. Similar to the irreducible set of invariants given for the Helmholtz free energy function, the set of irreducible invariants are given for the damage potential in [23] as:

$$\bar{I}_{Y1} = \mathbf{1}{:}\,\overline{\boldsymbol{Y}} \qquad \bar{I}_{Y2} = \mathbf{1}{:}\,(\overline{\boldsymbol{Y}})^{\mathbf{2}}$$

$$\bar{I}_{Y3} = \mathbf{1}{:}\,(\overline{\boldsymbol{Y}})^{\mathbf{3}} \tag{5-11}$$

$$\bar{I}_{Y4} = \mathbf{1}{:}\,(\bar{\boldsymbol{M}}^{\mathbf{1}}\overline{\boldsymbol{Y}}) \qquad \bar{I}_{Y5} = \mathbf{1}{:}\,(\bar{\boldsymbol{M}}^{\mathbf{1}}(\overline{\boldsymbol{Y}})^{\mathbf{2}})$$

$$\bar{I}_{Y6} = \mathbf{1}{:}\,(\bar{\boldsymbol{M}}^{\mathbf{2}}\overline{\boldsymbol{Y}}) \qquad \bar{I}_{Y7} = \mathbf{1}{:}\,(\bar{\boldsymbol{M}}^{\mathbf{2}}(\overline{\boldsymbol{Y}})^{\mathbf{2}})$$

The damage potential can be defined in a quadratic from as:

$$f_d(\bar{\boldsymbol{Y}}, \bar{\boldsymbol{M}}^1, \bar{\boldsymbol{M}}^2, \boldsymbol{\Omega}) = \frac{1}{2}\bar{\gamma}_1\bar{I}_{Y1}^2 + \bar{\gamma}_2\bar{I}_{Y2} + \frac{1}{2}\bar{\gamma}_3\bar{I}_{Y4}^2 + \bar{\gamma}_4\bar{I}_{Y5}$$

$$+\frac{1}{2}\bar{\gamma}_5\bar{I}_{Y6}^2 + \bar{\gamma}_6\bar{I}_{Y7} + \bar{\gamma}_7\bar{I}_{Y1}\bar{I}_{Y4} + \bar{\gamma}_8\bar{I}_{Y1}\bar{I}_{Y6} \quad \textbf{(5-12)}$$

$$+\bar{\gamma}_9\bar{I}_{Y4}\bar{I}_{Y6} - \left(\Omega_0 + \Omega(\boldsymbol{\omega}^H)\right)^2$$

Where $\bar{\gamma}_1$ to $\bar{\gamma}_9$ are material parameters, $\bar{I}_{Y1}$to $\bar{I}_{Y7}$ are the irreducible invariants of the damage energy release rate and the structural tensors and Ω_0 is an initial damage hardening conjugate force.

A more convenient form to write the damage potential in is in tensor form which requires the damage characteristic tensor. The damage characteristic tensor is found by taking the second derivative of the damage potential with respect to $\bar{\boldsymbol{Y}}$.

$$\bar{\mathbb{J}} = \frac{\partial^2 f_d}{\partial \bar{\boldsymbol{Y}}^2} \quad \textbf{(5-13)}$$

The damage potential expressed in terms of the damage characteristic tensor can now be defined and this definition is the one used in the construction of the damage part of the model.

$$f_d(\bar{\boldsymbol{Y}}, \Omega) = \left(\frac{1}{2}\bar{\boldsymbol{Y}} : \bar{\boldsymbol{J}} : \bar{\boldsymbol{Y}}\right)^{\frac{1}{2}} - \left(\Omega_0 + \Omega(\boldsymbol{\omega}^H)\right) = 0 \quad \textbf{(5-14)}$$

The thermodynamic force, $\Omega(\boldsymbol{\omega}^H)$ is defined as:

$$\Omega(\boldsymbol{\omega}^{\boldsymbol{H}}) = \omega_{t1}\boldsymbol{\omega}^H \quad \textbf{(5-15)}$$

Where ω_{t1} is the slope of the hardening curve. $\Omega(\omega^H)$ controls the evolution of the damage surface [23].

The damage hardening parameter is defined by equation (5-16). This is derived using the modified Klepaczko criterion with the inclusion of the normalised activation energy.

$$\omega^H = \frac{\varepsilon}{\varepsilon_{c0}} \frac{1}{\left(\left(\frac{\mu(\theta) b^3 u_0}{k\theta}\right) + 1\right)} \left(\frac{\frac{\sigma(\varepsilon)}{\mu(\theta)}}{\frac{\sigma_0}{\mu_0}} \right)^{\left(\frac{\mu(\theta) b^3 u_0}{k\theta}\right)} \quad \textbf{(5-16)}$$

Making use of the principle of maximum dissipation, the rate of change of damage tensor and the rate of hardening were calculated:

$$\dot{\bar{\boldsymbol{\omega}}} = \dot{\lambda}_d \frac{\partial f_d}{\partial \overline{\boldsymbol{Y}}} = \dot{\lambda}_d \frac{\bar{\boldsymbol{J}} : \overline{\boldsymbol{Y}}}{\left(\frac{1}{2} \overline{\boldsymbol{Y}} : \bar{\boldsymbol{J}} : \overline{\boldsymbol{Y}}\right)^{\frac{1}{2}}} \quad \textbf{(5-17)}$$

$$\dot{\bar{\boldsymbol{\omega}}} = \dot{\lambda}_d \frac{\partial f_d}{\partial \overline{\boldsymbol{Y}}} = \dot{\lambda}_d \frac{\bar{\boldsymbol{J}} : \overline{\boldsymbol{Y}}}{\left(\frac{1}{2} \overline{\boldsymbol{Y}} : \bar{\boldsymbol{J}} : \overline{\boldsymbol{Y}}\right)^{\frac{1}{2}}} \quad \textbf{(5-18)}$$

In equations 5.17 and 5.18, $\dot{\lambda}_d$ is a Lagrange multiplier which determines the proportionality between the rate measures and their conjugate forces [23]. The Lagrange multiplier is calculated by using a consistency condition, which says that the rate of change of the damage potential is zero when damage is evolving.

$$\dot{f}_d(\overline{\boldsymbol{Y}}, \Omega) = \frac{\partial f_d}{\partial \overline{\boldsymbol{Y}}} : \dot{\overline{\boldsymbol{Y}}} + \frac{\partial f_d}{\partial \Omega} \dot{\Omega} = 0 \quad \textbf{(5-19)}$$

Calculations for $\dot{\overline{\boldsymbol{Y}}}$ and $\dot{\Omega}$ combined with the consistency condition results in the Lagrange multiplier being calculated as shown in equation (5-20).

$$\dot{\lambda}_d = - \frac{\frac{\partial f_d}{\partial \overline{\boldsymbol{Y}}} : \left[[\mathbf{1} - \bar{\boldsymbol{\omega}}] \bar{\mathbb{C}} : \left[\overline{\boldsymbol{C}}_e (\boldsymbol{l} - \boldsymbol{l}_p) \right]_{sym} \right]}{\frac{\partial f_d}{\partial \overline{\boldsymbol{Y}}} : \left(\frac{\partial f_d}{\partial \overline{\boldsymbol{Y}}} \overline{\boldsymbol{S}} - [\mathbf{1} - \bar{\boldsymbol{\omega}}] \bar{\mathbb{C}} : \left[[\mathbf{1} - \bar{\boldsymbol{\omega}}]^T \frac{\partial f_d}{\partial \overline{\boldsymbol{Y}}} \right]_{sym} \right) + \frac{\partial f_d}{\partial \Omega} \frac{\partial \Omega}{\partial \omega^H}} \quad \textbf{(5-20)}$$

5.3 Plastic behaviour

Plastic behaviour is accounted for in the Cranfield model by a combination of Hills coefficients and the Mechanical Threshold Stress model.

Hill's coefficients are a set of six coefficients first introduced by Hill in 1948 to account for material anisotropy, up to orthotropy, and were derived from the analysis of a proposed yield criterion.

Similar to the models treatment of damage, a plastic potential is defined which is invariant to rigid body rotations [23]. As with the hyperelastic and damage parts of the model, an irreducible set of invariants is defined which consist of seven invariants. For the plastic potential these are defined in [23] in terms of the deviatoric part of Mandel stress as:

$$\bar{I}_1 = \mathbf{1}:\bar{\boldsymbol{\Sigma}}^{\boldsymbol{D}} = 0 \qquad \bar{I}_2 = \mathbf{1}:(\bar{\boldsymbol{\Sigma}}^{\boldsymbol{D}})^{\mathbf{2}}$$

$$\bar{I}_3 = \mathbf{1}:(\bar{\boldsymbol{\Sigma}}^{\boldsymbol{D}})^{\mathbf{3}} \qquad \textbf{(5-21)}$$

$$\bar{I}_4 = \mathbf{1}:(\bar{\boldsymbol{M}}^{\mathbf{1}}\bar{\boldsymbol{\Sigma}}^{\boldsymbol{D}}) \qquad \bar{I}_5 = \mathbf{1}:(\bar{\boldsymbol{M}}^{\mathbf{1}}(\bar{\boldsymbol{\Sigma}}^{\boldsymbol{D}})^{\mathbf{2}})$$

$$\bar{I}_6 = \mathbf{1}:(\bar{\boldsymbol{M}}^{\mathbf{2}}\bar{\boldsymbol{\Sigma}}^{\boldsymbol{D}}) \qquad \bar{I}_7 = \mathbf{1}:(\bar{\boldsymbol{M}}^{\mathbf{2}}(\bar{\boldsymbol{\Sigma}}^{\boldsymbol{D}})^{\mathbf{2}})$$

In a quadratic form, the plastic potential, f_{pl}, is defined in terms of a set of seven irreducible invariants for the yield function, I_1 to I_7, and a set of six material parameters, β_1 to β_6, as:

$$f_{pl}(\bar{\boldsymbol{\Sigma}}^{D}, \bar{\boldsymbol{M}}^{1}, \bar{\boldsymbol{M}}^{2}, \boldsymbol{\sigma}_{MTS}) = \bar{\beta}_1\bar{I}_2 + \frac{1}{2}\bar{\beta}_2\bar{I}_4^2 + \frac{1}{2}\bar{\beta}_3\bar{I}_6^2 + \bar{\beta}_4\bar{I}_5 + \bar{\beta}_5\bar{I}_7 + \bar{\beta}_6\bar{I}_4\bar{I}_6 - \sigma_{MTS}^2 \qquad \textbf{(5-22)}$$

Where $\boldsymbol{\sigma}_{MTS}$ is a flow stress calculated using the Mechanical Threshold Stress model, as outlined in section **3.5.1.**

Similar to the method used in deriving the damage part of the model, the second derivative of the plastic potential was taken with respect to the stress, resulting in a characteristic tensor, $\mathbb{A}$. The plastic potential is then given in terms of $\mathbb{A}$ and the flow stress.

$$f_{pl}(\overline{\boldsymbol{\Sigma}}^D, \overline{\boldsymbol{M}}^1, \overline{\boldsymbol{M}}^2, \boldsymbol{\sigma}_{MTS}) = \left(\frac{1}{2}\overline{\boldsymbol{\Sigma}}^D : \overline{\mathbb{A}} : \overline{\boldsymbol{\Sigma}}^D\right)^{\frac{1}{2}} - \boldsymbol{\sigma}_{MTS}\left(\boldsymbol{\varepsilon}_p, \dot{\boldsymbol{\varepsilon}}_p, \boldsymbol{\theta}\right) \quad \textbf{(5-23)}$$

Equation (5-23) is the form of the plastic potential that was used by Djordjevic for the development of the plastic deformation part of the model.

The rate of plastic deformation tensor, $\boldsymbol{d_p}$, is defined in [23] to be

$$\overline{\boldsymbol{d}}_p = \dot{\boldsymbol{\lambda}}_{pl}\frac{\partial f_{pl}}{\partial \overline{\boldsymbol{\Sigma}}^D} = \dot{\lambda}_{pl}\frac{\overline{\mathbb{A}} : \overline{\boldsymbol{\Sigma}}^D}{\sqrt{\frac{1}{2}\overline{\boldsymbol{\Sigma}}^D : \overline{\mathbb{A}} : \overline{\boldsymbol{\Sigma}}^D}} \quad \textbf{(5-24)}$$

And the effective strain, $\dot{\boldsymbol{\varepsilon}}_p$ is shown to be equal to the Lagrange multiplier, $\dot{\boldsymbol{\lambda}}_{pl}$, the value of which is obtained from the consistency condition is given by:

$$\dot{\boldsymbol{\lambda}}_{pl} = \dot{\boldsymbol{\varepsilon}}_p = \frac{\left(2\overline{\boldsymbol{C}}_e\frac{\partial f_{pl}}{\partial \overline{\boldsymbol{\Sigma}}^D}\overline{\boldsymbol{S}} + \frac{\partial f_{pl}}{\partial \overline{\boldsymbol{\Sigma}}^D} : \overline{\boldsymbol{C}}_e(\overline{\boldsymbol{C}}_e\overline{\mathbb{C}})\right) : \left[\overline{\boldsymbol{l}}\right]_{sym} - \frac{\partial f_{pl}}{\partial \overline{\boldsymbol{\Sigma}}^D} : \overline{\boldsymbol{C}}_e\overline{\mathbb{C}} : \left[\overline{\boldsymbol{C}}_d\overline{\boldsymbol{l}}_d\right]_{sym}}{\left(2\overline{\boldsymbol{C}}_e\frac{\partial f_{pl}}{\partial \overline{\boldsymbol{\Sigma}}^D}\overline{\boldsymbol{S}} + \frac{\partial f_{pl}}{\partial \overline{\boldsymbol{\Sigma}}^D} : \overline{\boldsymbol{C}}_e(\overline{\boldsymbol{C}}_e\overline{\mathbb{C}})\right) : \left[\frac{\partial f_{pl}}{\partial \overline{\boldsymbol{\Sigma}}^D}\right]_{sym} + \frac{\partial \boldsymbol{\sigma}_{MTS}}{\partial \widehat{\boldsymbol{\sigma}}}\frac{\partial \widehat{\boldsymbol{\sigma}}}{\partial \boldsymbol{\varepsilon}_p}} \quad \textbf{(5-25)}$$

5.3.1 Mechanical Threshold Stress model (MTS)

The MTS provides a scalar valued flow stress as a function of the plastic strain and the temperature. The model was first proposed in 1988 by Follansbee and Kocks, with the formulation coming from the observations of microstructural thermally activated deformation processes such as dislocation motions. The model was based on two assumptions [8]:

i) Viscous drag effects are small compared to the dominant thermally activated dislocation motion. This assumption limited the model to only being valid for strain rate less than about $10^4 s^{-1}$.
ii) High temperature diffusion effects are absent,

Mathematically the model contains two parts; an athermal part and a thermal part.

$$\boldsymbol{\sigma}_{MTS} = \boldsymbol{\sigma}_a + \frac{\boldsymbol{\mu}}{\boldsymbol{\mu_0}}(\widehat{\boldsymbol{\sigma}} - \boldsymbol{\sigma_a})\boldsymbol{s}\left(\boldsymbol{\theta}, \dot{\boldsymbol{\varepsilon}}_{\boldsymbol{p}}\right) \quad \textbf{(5-26)}$$

Where $\boldsymbol{\sigma}_a$ is the athermal component of flow stress, $\hat{\boldsymbol{\sigma}}$ is the plastic evolution parameter and $\boldsymbol{s}(\boldsymbol{\theta}, \dot{\boldsymbol{\varepsilon}}_{\boldsymbol{p}})$ is the thermal activation factor.

The thermal activation factor is defined to be:

$$\boldsymbol{s}(\boldsymbol{\theta}, \dot{\boldsymbol{\varepsilon}}_{\boldsymbol{p}}) = \left[1 - \left(\frac{k\boldsymbol{\theta} ln\left(\frac{\dot{\boldsymbol{\varepsilon}}_{\boldsymbol{0}}}{\dot{\boldsymbol{\varepsilon}}_{\boldsymbol{p}}}\right)}{\boldsymbol{\mu} b^3 g_0}\right)^{\frac{1}{q}}\right]^{\frac{1}{p}} \quad \textbf{(5-27)}$$

The evolution parameter, $\hat{\boldsymbol{\sigma}}$, can be thought of as a balance of two processes; dislocation accumulation, Θ_0, and dynamic recovery, $\Theta(\dot{\varepsilon}, \theta, \hat{\sigma})$, which together form the strain hardening rate. The strain hardening rate is linearly dependent over a range of stresses and strains, however saturation behaviour can be observed. Due to this a hyperbolic function is used for the definition of the hardening rate.

$$\Theta = \frac{\partial \hat{\sigma}}{\partial \varepsilon_p} = \Theta_0 \left(1 - \frac{tanh\left(\alpha \frac{\hat{\sigma}}{\hat{\sigma}_s}\right)}{tanh(\alpha)}\right) \quad \textbf{(5-28)}$$

Relationships exist for the calculation of Θ_0 and $\hat{\sigma}_s$, however solving analytically for the hardening parameter and for the flow stress is not possible except for a constant strain rate and temperature [23]. Therefore the assumption was made that the strain rate and the temperature are constant within a time step. Using this assumption a reference hardening rate is calculated using equation (5-29), which completes the plastic description in the model.

$$\frac{\partial \boldsymbol{\sigma}_{MTS}}{\partial \hat{\boldsymbol{\sigma}}} \frac{\partial \hat{\boldsymbol{\sigma}}}{\partial \boldsymbol{\varepsilon}_p} = \frac{\boldsymbol{\mu}}{\boldsymbol{\mu}_0} s(\theta, \dot{\bar{\boldsymbol{\varepsilon}}}_p) \Theta_0 \left(1 - \left[\frac{tanh\left(\alpha \frac{\hat{\boldsymbol{\sigma}}}{\hat{\boldsymbol{\sigma}}_s}\right)}{tanh(\alpha)}\right]\right) \quad \textbf{(5-29)}$$

5.4 Shockwaves

The Cranfield model is capable of modelling shock loading. This is achieved by making use of a known result that the deformation is driven only by the pressure component of the stress for stresses far in excess of the Hugoniot Elastic Limit

(discussed in section 6). From this result, a generalised pressure was defined using the method describe by Vignjevic et al in [26]. The generalised pressure is derived from a variation of a standard decomposition of the stress tensor into its spherical and deviatoric components.

$$\boldsymbol{S}_{ij} = P\boldsymbol{\psi}_{ij} + \boldsymbol{S}_{ij}^{D} \tag{5-30}$$

A further pair of tensors were introduced into the decomposition $\tilde{P}\boldsymbol{\psi}_{ij}$ and $\overline{\boldsymbol{S}}_{ij}^{\tilde{D}}$ so that the two terms are orthogonal, where the dot product between them two is zero. Therefore, equation (5-30) is written in terms of the orthogonal tensors as:

$$\overline{\boldsymbol{S}}_{ij} = -\tilde{P}\boldsymbol{\psi}_{ij} + \overline{\boldsymbol{S}}_{ij}^{\tilde{D}} \tag{5-31}$$

Equation (5-31) was then multiplied through by the pressure tensor $\boldsymbol{\psi}_{ij}$ and relationships for the orthogonal pressure and devatoric stress components were found.

$$\tilde{P} = \hat{P} - \frac{\overline{\boldsymbol{S}}_{ij}^{\hat{D}}\boldsymbol{\psi}_{ij}}{\boldsymbol{\psi}_{kl}\boldsymbol{\psi}_{kl}} = \hat{P} - \hat{S} = -\frac{\overline{\boldsymbol{S}}_{ij}\boldsymbol{\psi}_{ij}}{\boldsymbol{\psi}_{kl}\boldsymbol{\psi}_{kl}} \tag{5-32}$$

Expressing the stress as a product of the stiffness and the strain allowed the pressure to be defined as:

$$\begin{aligned}\hat{P} &\\ &= -\left(\frac{(\mathbb{C}_{11}+\mathbb{C}_{12}+\mathbb{C}_{13})^2 + (\mathbb{C}_{12}+\mathbb{C}_{22}+\mathbb{C}_{23})^2 + (\mathbb{C}_{13}+\mathbb{C}_{23}+\mathbb{C}_{33})^2}{3}\right)^{\frac{1}{2}} \overline{\boldsymbol{E}}_{v} \\ &= -3K_{\psi}\overline{\boldsymbol{E}}_{v}\end{aligned} \tag{5-33}$$

And the tensor ψ_{ij} as:

$$\boldsymbol{\psi}_{(ii)} = \frac{\mathbb{C}_{i1}+\mathbb{C}_{i2}+\mathbb{C}_{i3}}{\left(\frac{1}{3}(\mathbb{C}_{11}+\mathbb{C}_{12}+\mathbb{C}_{13})^2 + (\mathbb{C}_{12}+\mathbb{C}_{22}+\mathbb{C}_{23})^2 + (\mathbb{C}_{13}+\mathbb{C}_{23}+\mathbb{C}_{33})^2\right)^{\frac{1}{2}}} \tag{5-34}$$

Where the terms $\mathbb{C}_{ij}$ are terms in the stiffness matrix and $K_{\psi}$is a generalised bulk modulus.

This decomposed stress term was coupled with the Mie-Gruneisen shock equation of state available in the DYNA3D code and forms the models capability of modelling shock waves.

5.5 DYNA3D

The Cranfield model is implemented in Lawrence Livermore National Laboratories DYNA3D code. DYNA3D is a non-linear, transient dynamic, explicit finite element code. The code has many features available in it:

- It allows for different types of elements, including truss and beam elements, 2-d shell elements and solid elements.
- Boundary, initial and loading conditions.
- Range of contact algorithms
- Number of implemented constitutive model for modelling complex material behaviour.
- Several Equations of state are coupled with some material models
- Allows for rigid body dynamics.

The DYNA3D code available at Cranfield University is coupled to the SPH code developed in house, although the Cranfield model is not currently coupled with the SPH code. The current implementation of the Cranfield model can only use hexagonal solid elements [23].

5.6 Model improvements

The main aim of this work is to propose model improvements for implementation into the existing material model. The part of the model in which the proposed improvements can be made are on the plastic deformation part of the model; more specifically the MTS part of the plasticity description.

Improvements are required for a number of reasons. The first main reason for this is the models capability of reproducing shockwaves accurately. It has recently been observed experimentally that there is an existence of a so-called superelastic precursor wave at very short time periods, of the order of nanoseconds, after the shock inducing impact, see chapter 6. The current

model cannot reproduce this behaviour using the MTS model. Therefore it is apparent that a new plasticity model is required.

Further to this, the MTS model is quite an old model, with respect to the rest of the formulation of the current model. Therefore it would be an advantage to upgrade this section of the model with a newer approach which will include more recently discovered/developed methods, potentially allowing for more accurate representation of the shock wave formation, especially at very short time scales after impact.

5.7 Summary

The current elastic, plastic and damage parts of the Cranfield model have been discussed. It has been shown how the model reproduces deformation using sets of irreducible invariants, along with defined thermodynamic style potentials for the elastic, plastic and damage behaviours.

The decomposition used in the current Cranfield model for the stress tensor, used as a part of the shock representation has been introduced. This decomposition allows for a generalised pressure to be defined, which is used along with the Mie-Gruneisen equation of state when representing high velocity impact.

The limitations of the plasticity part of the model, in the use of the Mechanical Threshold Stress model have been discussed with the short timescale behaviour requirements for the future development of the model being indicated. The remainder of this work will focus on identifying potential alternative models/methods which can be used as a replacement for the MTS model in future iterations of the Cranfield model.

6 Shock wave modelling

It is discussed in chapter 5 that the motivation for future improvements to the Cranfield model is due to the models shock wave representation ability. To understand the requirements of modelling shock waves, this chapter focusses on the governing properties and conditions under which the shock waves form. This chapter contains six sections: sections 6.1 and 6.1 discuss the formation and propagation of stress waves in general in a material as well as the governing wave equation. The condition under which the stress waves can form a shock wave are discussed in section 6.3, with the relations relating the properties of the material in front and behind a shock then being introduced in section 6.4. Finally the important Swegle-Grady fourth power law is introduced. This power law is one of the motivating factors for this work as a whole.

6.1 Stress waves

Shock waves can form in a material when the surface of the material is subjected to a rapid acceleration. This can occur when a high velocity impact occurs or when an explosive is detonated whilst in contact with the surface. To understand how shock waves occur, it is first important to establish how stress waves form and propagate in a material.

To understand how stress waves are formed, it is convenient to consider a plate formed of many, very thin layers of particles, parallel to the impact plane, being exposed instantaneously to a pressure which thereafter remains constant [27].

When the pressure is first applied at the surface, the surface layer of particles is accelerated, supporting the entirety of the pressure. The acceleration of the first layer of particles is in the direction of the second layer of particles causing compressive stresses to build up as the first layer moves closer to the second. This in turn accelerates the second layer at an increasing rate towards the third layer. The process continues with the second layer accelerating the third layer and then subsequent layers being accelerated. Relative motion ceases when the compressive stresses between the first two layers is equal to the applied pressure; the pressure is supported entirely by the compressive stresses in the

material. This process results in many layers of particle being accelerated in the direction of disturbance. Via this process, stress waves are formed [27].

As stress waves propagate through a material, they cause stresses and therefore strains on the particles within it. This can result in plastic deformation if the stress is greater than the materials elastic limit.

Stress waves will continue to propagate through the material until they reach a free surface. At a free surface they are reflected as tensile stress waves, in an ideal situation with equal velocity and magnitude.

6.2 Wave Equation

Stress waves can be described mathematically by the wave equation. This can be derived by considering the 1D element of a bar with width dx, area A and an applied stress in the x-direction as shown in Figure 6-1 [28].

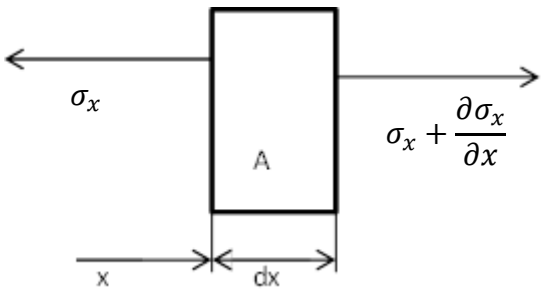

Figure 6-1: Element of a one-dimensional bar with the forces and stresses acting on it.

By conserving momentum, equation (6-1) can be written.

$$\frac{\partial \sigma}{\partial x} = \rho \frac{\partial v}{\partial t} \quad \textbf{(6-1)}$$

From the definitions of strain and velocity, the continuity condition is derived.

$$\varepsilon = \frac{\partial u}{\partial x} \quad \textbf{(6-2)}$$

$$v = \frac{\partial u}{\partial t} \quad \textbf{(6-3)}$$

In equations (6-2) and (6-3), v is the particle velocity and ε is the longitudinal strain in the x-direction.

Substituting the definitions of velocity into equation (6-1) gives equation (6-4).

$$\frac{\partial \sigma}{\partial x} = \rho \frac{\partial^2 u}{\partial t^2} \tag{6-4}$$

Applying the chain rule to equation (6-4) and assuming the stress, σ, is a single-valued function of strain such that $\sigma = \sigma(\varepsilon)$ equation (6-5) is formed.

$$\frac{\partial \sigma(\varepsilon)}{\partial \varepsilon}\frac{\partial \varepsilon}{\partial x} = \rho \frac{\partial^2 u}{\partial t^2} \tag{6-5}$$

From the definition of strain, ε, as shown in equation (6-2) the first differential of the strain can be written in terms of u.

$$\frac{\partial \varepsilon}{\partial x} = \frac{\partial^2 u}{\partial x^2} \tag{6-6}$$

Equation (6-6) can be substituted into equation (6-5) to form the one-dimensional wave equation, equation (6-7).

$$c^2 \frac{\partial^2 u}{\partial x^2} = \frac{\partial^2 u}{\partial t^2} \tag{6-7}$$

Where:

$$c = \sqrt{\frac{S}{\rho}} \tag{6-8}$$

$$S = \frac{\partial \sigma}{\partial \varepsilon} \tag{6-9}$$

Physically, c, is the wave velocity and S is the slope of the stress-strain curve.

Equation (6-8) shows the wave speed has a dependence on the slope of the stress-strain curve. The slope of the stress-strain curve is not constant. A change of slope occurs at the yield point. Due to this it is apparent that two types of stress wave form and propagate: an elastic wave with a wave speed calculated from the slope of the Hooke's law region of the stress-strain curve

and an inelastic wave with a wave speed calculated from the slope of the stress-strain curve after the yield point. For a state of uniaxial stress, the slope of the Hooke's law region is always steeper that that after the yield point, therefore shock waves cannot form.

6.3 Uniaxial Strain

It has been shown that in a state of uniaxial stress shock waves cannot form. However, in a state of uniaxial strain, under high stress amplitude of high strain rate a shock wave can form and propagate through the material.

A typical uniaxial strain – longitudinal stress curve is shown in Figure 6-2.

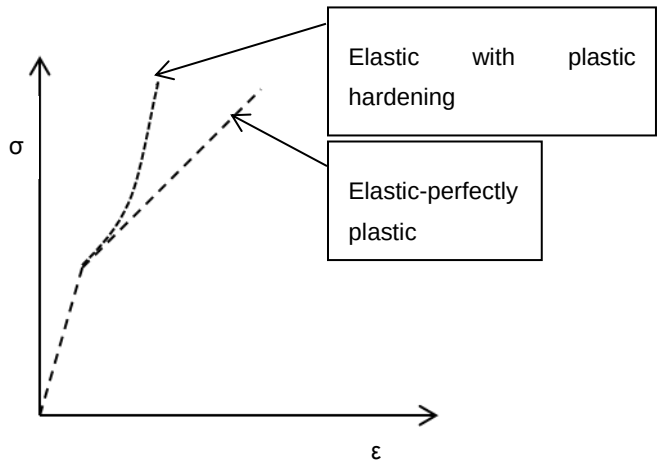

Figure 6-2: Longitudinal stress-strain curve in uniaxial strain state showing the curve of an elastic perfectly plastic deformation, and a curve of elastic-plastic with hardening.

As the strain state is uniaxial, i.e. strains in only one direction, then the following relations hold:

$$\varepsilon_x \neq 0 \qquad \varepsilon_y = \varepsilon_z = \varepsilon_{xy} = \varepsilon_{xz} = \varepsilon_{yz} = 0 \tag{6-10}$$

It is assumed that the strain can be decomposed and written in terms of an elastic term and a plastic term [27]

$$\varepsilon_x = \varepsilon_x^e + \varepsilon_x^p \tag{6-11}$$

It is also assumed that the plastic flow is incompressible and Von Mises or Tresca yield conditions are imposed. These conditions allows for a relationship between the x-directional stress and the strain:

$$\sigma_x = \frac{E(1-v)}{(1-2v)(1+v)}\varepsilon_x = \left(K + \frac{4G}{3}\right)\varepsilon_x \tag{6-12}$$

Where G is the shear modulus, K the bulk modulus, E the elastic modulus and v the Poission's ratio.

The yield condition is applied beyond the yield point. Applying this, the x component of stress can be shown in terms of strain and yield criterion:

$$\sigma_x = K\varepsilon_x + \frac{2Y_0}{3} \tag{6-13}$$

This yield point can be shown to be different to the yield point under uniaxial stress by substitution of ε_x taken from a rearranged equation (6-12). The yield point for a state of uniaxial strain is known as the Hugoniot elastic limit and is mathematically defined as:

$$\sigma_x = \left(\frac{K}{2G} + \frac{2}{3}\right)Y_0 \tag{6-14}$$

As shown previously in equations (6-7) and (6-8) the speed of the stress wave can be obtained from the wave equation, and that the speed is dependent on the slope of the stress strain curve. As two waves form, due to the two regions of different slopes, the speed of each wave can be found. For a purely elastic wave the speed is found by:

$$c_e = \sqrt{\frac{(K + 4\,G/3)}{\rho}} \tag{6-15}$$

Whilst the plastic wave speed is given by

$$c_p = \sqrt{\frac{K}{\rho}} \tag{6-16}$$

Equations (6-15) and (6-16) would imply that for a perfectly plastic material the elastic wave will have a greater wave speed than the plastic wave. However, if plastic hardening occurs, the slope of the plastic region of the stress strain curve in a state of uniaxial strain is in fact steeper than the elastic region. Therefore the plastic waves will have a greater wave speed then the elastic wave. A shock wave is formed when the speed of the plastic wave is greater than the speed of the elastic wave, which causes a steep plastic front which breaks down forming a single discontinuous front.

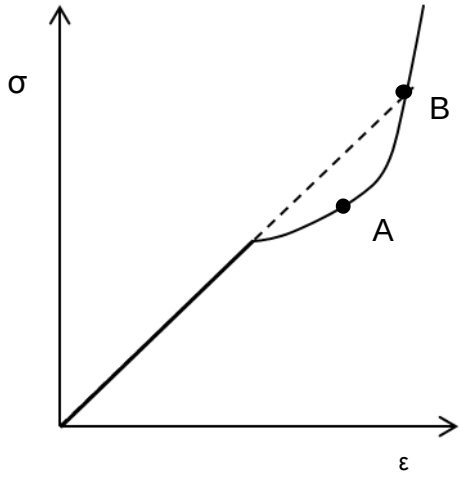

Figure 6-3: Stress-train curve in a state of uniaxial strain.

Figure 6-3 shows a typical longitudinal stress vs. longitudinal strain curve obtained in a state of uniaxial strain. From this three types of waves can be formed:

i) When the stress is above the HEL, but is below the strong shock limit (point B on Figure 6-3), for instance stress state that corresponds to the point A in Figure 6-3, a two wave system propagates; an elastic precursor wave followed by a slower plastic shock wave.

ii) If the stress level is at point B, the strong shock limit, then the elastic precursor wave and the plastic shock wave will propagate at the same speed.

iii) If the stress level is higher than point B, the speed of the plastic wave will be greater than the speed of the elastic wave, therefore only a single strong shock wave front will propagate through the material.

6.4 Hugoniot Relations

As a shock wave propagates, properties and parameters of the material change. These include pressure, velocity, density and temperature. The Hugoniot relations relate these variables through the shock front and are derived from the conservation laws; the conservation of mass, momentum and energy.

The conservation of mass is mathematically defined by equation (6-17).

$$\rho_0 U_S = \rho_1 (U_s - U_p) \quad \textbf{(6-17)}$$

Where $U_s$and $U_p$are the shock velocity and the particle velocity respectively and ρ_0 and ρ_1 are the densities in front and behind the shock.

As this is a conservation law, its physical meaning is that the mass that flows into the shock front must be equal to the mass leaving the shock.

The conservation on momentum is expressed mathematically as

$$P_1 - P_0 = \rho_0 U_s U_p \quad \textbf{(6-18)}$$

Where $P_1 - P_0$is an imparted impulse causing a change in momentum of mass traveling through the shock.

The conservation of energy is expressed in equation (6-19).

$$P_1 U_p = \frac{1}{2}\rho_0 U_s U_p^2 + \rho_0 U_s (E_1 - E_0) \quad \textbf{(6-19)}$$

The energy relation can be reduced to eliminate $U_s$and U_p by using equations (6-17) and (6-18). The resultant equation, equation (6-20) is known as the Hugoniot equation.

$$E - E_0 = \frac{1}{2}(V_0 - V_1)(P_1 + P_0) \quad \textbf{(6-20)}$$

Contained within these four equations are five unknowns. This implies that if just one variable is known or measured, it is possible to calculate the remaining four. The Hugoniot equation gives the locus of all the thermodynamic states achievable during a single shock [29]. The Hugoniot can be plotted in different ways, depending on the variables of interest. It can be plotted as shock velocity and particle velocity, pressure and particle velocity or pressure and volume.

6.5 Swegle-Grady power law

Experimental studies of shock waves have shown that there exists a power law between the strain rate and the stress associated with plastic shock deformation [30]. The power law is of the form

$$\dot{\varepsilon} \propto \sigma^4 \quad \textbf{(6-21)}$$

The exact physical origin of the power law is unknown; however attempts have been made to explain it. Presented in this section is the mathematical explanation presented by Malygin et al. [31], as this explanation attempts to not only provide an explanation of the physical origin, but also provide an analytical relationship between the strain rate and the stress.

Malygin et al. [31] explain the physical basis of such a power law as being due to the generation of geometrically necessary dislocations in the shock wave front. The density of generated GND is found to be proportional to the pressure in the waves to the power of three. When this is substituted into the Orowan relationship, which governs the strain rate, $\dot{\varepsilon} = mb\rho u$ has a linear dependence on the density of dislocations and the velocity of dislocations. The velocity of dislocations is analysed in [31], and is found to vary linearly on the pressure in the shock wave. Substitution of the found dependencies of pressure of the density of dislocations and the velocity of dislocations results in the Swegle-Grady law in the form

$$\dot{\varepsilon} = K_P P^4 \tag{6-22}$$

Where

$$K_P = \frac{0.4m^2(1-2v)\pi^2}{2^{3/2}3^3}\left(\frac{E}{B}\right) \approx 2.6 \times 10^{-3}\left(\frac{E}{B}\right) \tag{6-23}$$

Where m is an orientation factor, v is the Poisson's ratio, E is the Young's modulus of the crystal in the absence of compression and B is the coefficient of viscous drag of dislocations.

6.6 Summary

The main physical principles associated with the formation of shockwaves have been introduced. It has been shown that a state of uniaxial strain is required for the formation of a shock wave.

The Hugoniot relations, relating material properties in front and behind a shock wave have been introduced. These relations are of significant importance to the modelling of materials as they allow for the calculation of material properties after wave propagation without any knowledge required of the conditions in the thin shock front.

Finally, the Swegle-Grady 4th-power law has been introduced. The law has been widely observed in experimental results, therefore reproduction of this law in the shock wave representation of the model is of significance. A potential explanation of this law is given by considering the generation of GND at the shock front. This is an important result, as it will be called upon in chapter 7 when the Malygin shock wave model is introduced.

7 Dislocation self-organisation processes

The first method of modelling plasticity that has been identified as being relevant for potential future inclusion in the Cranfield model is the so-called Self-organisational processes of dislocations model. This model makes use of experimental observations of dislocations to develop expressions for the evolution of the density of dislocations during deformations. The model has been identified for analysis as it has a continuum mechanics base, but includes microstructural effects, in the form of dislocations.

This chapter contains eight sections. Section 7.1 discusses the multistage nature of strain hardening, a process for which there appears to be linked to the formation of dislocation structures. Section 7.2 introduces the dislocation patterns that are observed after deformation, with a thermodynamical explanation of the structuring process given in 7.3. The simulation of the patterning is discussed in section 7.4, where an early method is outlined, with the results and limitations discussed. Following this, a much more rigorous dislocation kinetic model is discussed in section 7.5, with the shock wave model born out of the same dislocation kinetic equations being introduced in 7.6. Finally discussion is given to the usefulness of this method to the future development of the Cranfield model

The experimental observations forming the basis of this model are from experiments investigating the dislocation distribution in plastically deformed metals, which are found to show that as plastic deformation occurs, the dislocation distribution evolves into a structured pattern [32]. The exact patterns which the dislocations form depend on the degree of plastic deformation and the strain hardening. This formation of patterns, along with the strain hardening having a multistage nature has led to the development of a method referred to as self-organisation processes of dislocations. Within this method two important dislocation mechanisms are double cross slip of screw dislocation components into parallel slip planes to the primary slip plane, and the emergence of Frank-Reid dislocation sources. These mechanisms have impact on the strain hardening, which is found experimentally to be of a multistage nature. Along

with these, other dislocation processes have an impact and are therefore accounted for in the method.

Double cross slip of screw dislocations occurs when the screw component of a dislocation overcomes an obstacle in the primary slip plane by entering a cross slip plane (see section 2.6.2), bypassing the obstacle, and then entering a slip plane parallel to the primary slip plane. The Frank-Reid dislocation source mechanism is detailed in 2.6.4.

7.1 Multistage nature of strain hardening

Strain hardening is an important process that is observed in metals. Strain hardening is characterised by an increase in resistance to deformation under increasing plastic deformation. Strain hardening is observed experimentally to be a multistage process. Patterns formed by dislocations during deformation, through self-organisation, provide an insight into the dislocation mechanisms which occur during the strain-hardening process, which is associated with plastic deformation. Figure 7-1 shows a typical strain hardening curve for an FCC metal, with the different stages of hardening labelled in roman numerals.

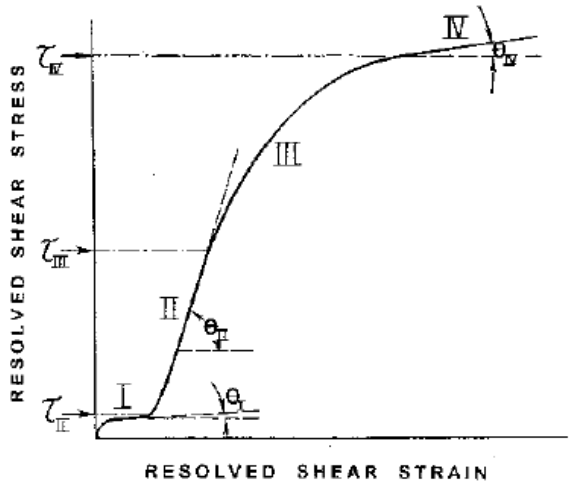

Figure 7-1: Idealised strain-hardening curve typical of FCC metal showing 4 stages [33].

The strain hardening shown in Figure 7-1 shows four stages of hardening. In some materials, under certain conditions a fifth stage is observed, with different dislocation mechanisms being prominent in each. The first three stages are

described extensively by Malygin in [9]. The first stage of hardening, commonly referred to as the stage of easy glide, is predominantly caused by the interaction of mobile dislocations with edge dipoles, causing immobilisation.

The second stage of strain hardening sees the rate of hardening steeply increase. This is due to the fact that more immobilisation mechanisms occur on the mobile dislocations. As with the first stage, mobile dislocations will still interact with edge dipoles, but additionally interactions of dislocations with dislocations in secondary slip systems occur. These interactions can immobilise the dislocations in both the primary and secondary slip systems, or annihilation can occur.

The third stage described in [9] is a stage which is associated with dynamic recovery, which is associated with annihilation of screw dislocations. This recovery leads to a decrease in the rate of strain hardening, as seen in Figure 7-1.

Further stages of hardening, the fourth and fifth stages, occur when significant plastic deformation has occurred already. When this happens, distortions occur at grain boundaries and as a result of bending. To accommodate these geometrical distortions of the crystals, additional dislocations are generated which are commonly referred to as geometrically necessary dislocations (GND). The patterning at the fourth and fifth stages of strain hardening consist primarily of fragmented dislocation structures, formed from GND's.

7.2 Structures

When viewing plastically deformed metals using a transmission electron microscope (TEM) the dislocation structures that are formed can be seen. The main structures observed are persistent slip bands and cellular structures. Other structures can be observed, but it is the bands and cells which are most common.

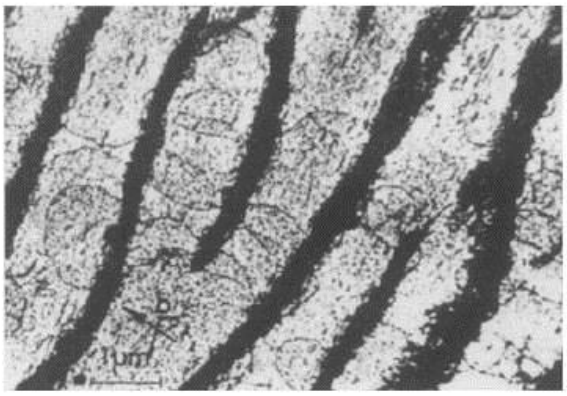

Figure 7-2: TEM image of persistent slip bands in cyclically fatigued copper [32]

Figure 7-2 shows a transmission electron microscope image of a section of cyclically fatigued copper approximately 9 µm by 6 µm in size. The image shows the persistent slip bands that have formed during the cyclic fatiguing process.

Slip bands are the predominant dislocation structure observed during the first stage of hardening. The bands consist of immobilised dislocations which have encountered objects such as edge dipoles and impurities.

At the second and third stages, the banded structures typically give way to 2-d network and 3-d cellular dislocation structures, as is shown in Figure 7-3.

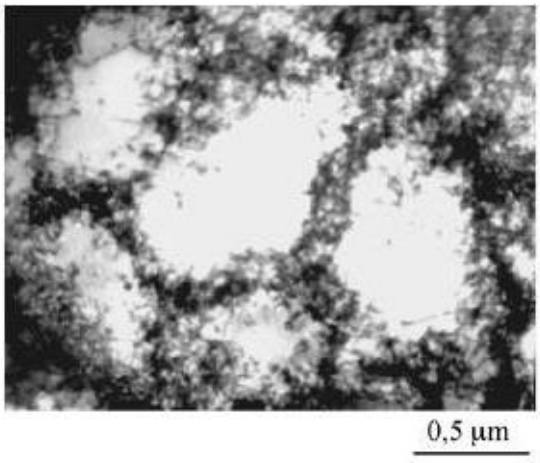

Figure 7-3: Cellular dislocation structure observed in a single Ni crystal [34]

The cellular dislocation structure shown in Figure 7-3 is formed of cell walls which contain a high density of dislocations, and the main bodies of the cells which have a much lower density of dislocations.

At the fourth and fifth stages of hardening a fragmented dislocation structure is observed [35]. These fragmented dislocation structures are typically seen after large deformations have occurred. As highlighted in section 7.1, fragmented dislocation structures are accumulations of dislocations generated due to geometrical distortions to the crystal, referred to as geometrically necessary dislocations [35]. The physical size of a fragmented dislocation structure can range between several hundreds of nanometres to several microns, with the size typically decreasing with increasing amounts of deformation.

7.3 Theory explaining structures

So far, the formation of dislocation structures has been discussed with reference to the multistage nature of strain hardening and the specific dislocation processes that occur during structure formation. The dislocation processes alone do not explain why the self-organisation of dislocations occurs, here the reason as to why dislocations self-organise is addressed.

Early attempts to explain the reasons for the formation of structures in metals undergoing plastic deformations were made by Holt [36]. The explanation given comprised of long ranging interactions energetically favouring clustering, as the interaction energy decreases with decreasing dislocation separation. This explanation however is rather simplistic and ignores short-range interactions between. the individual dislocations which are of importance.

A further, more detailed explanation is provided in [32], which sites the work of Seeger [37] by consideration of the structures from a thermodynamics point of view, specifically the changes of entropy of the system.

Prigogine's theory of dissipative systems implies that the formation of ordered structures of dislocations is related to a decrease of entropy in the system. However, the second law of thermodynamics states that, for a real, irreversible system the change in entropy is always positive [25]. For both of these

statements to be true of the same system, the system must act to pump entropy into the environment. Considerations are given to a single dislocation which requires activation energy to overcome an obstacle. From here, equation (7-1) is derived, which is the condition for a decrease of entropy to be possible.

$$dU < W + K(\dot{\rho}^{+} + \dot{\rho}^{-}) \quad \textbf{(7-1)}$$

Where dU is the infinitesimal change of internal energy, W is the work done on the system, K is a normalising coefficient and $\dot{\rho}^{+}$ and $\dot{\rho}^{-}$ represent the increase of dislocations from the activation of sources and the decrease of dislocation number due to annihilation processes respectively [32]

While the thermodynamic arguments of Seeger provide an explanation as to why dislocation structures form, and a condition to allow them to form, it does not provide any detail of the evolution of the system.

7.4 Simulation of formation of structures

The formation of self-organised dislocation structures have been simulated in both FCC and BCC single crystals by Sangi et al. [32]. The simulations were done using a combined cellular automata (CA) and molecular dynamics (MD) model. The combined approach was taken as the cellular automata part describes short range interactions of dislocations, whereas the molecular dynamics part considers the long-range interactions of dislocations [32].

The structures simulated in [32] depend on numerous conditions, including: the number of active glide systems, the applied forces and the cut-off radius of dislocations. The cut-off radius of dislocations is a parameter which is required for the molecular dynamics part of the model, and it sets the distance over which dislocations can interact via long range interactions.

Figure 7-4 displays the result of the simulation carried out by Sangi et al. which shows the banded structure expected at the first stage of hardening. The simulation was done using the data of iron. Figure 7-5 displays the simulation of the cellular dislocation structure from [32] which was done for an FCC structure.

Finally Figure 7-6 shows a labyrinth structure that was observed in a simulation of an FCC material at 300°C.

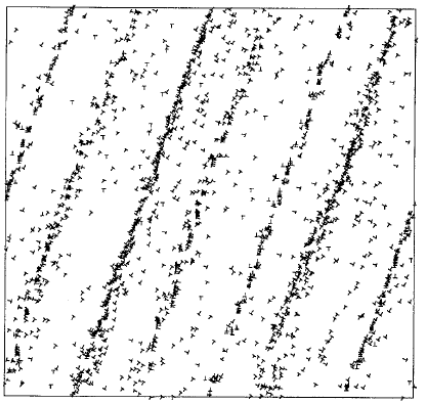

Figure 7-4: Wall structure of dislocation simulated in [32] with data of iron.

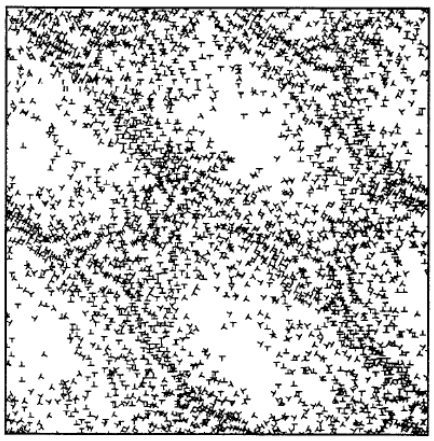

Figure 7-5: Simulation of 4000 edge dislocations forming cellular structures in an FCC structure [32].

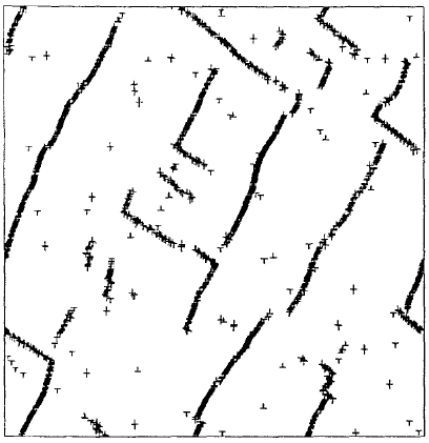

Figure 7-6: Labyrinth dislocation structure observed in a simulation of FCC crystals at 300°C [32].

The combined CA and MD simulation approach used by Sangi et al. in [32], despite showing the formation of dislocation structure has a few problems. The first of these involves the relatively low numbers of dislocations used. All of the simulations carried out were done using only 4000 dislocations, whereas in a real metal which has undergone significant working there may be as many as 10^{11} cm^{-2} [38]. Increasing the number of dislocations in the simulation to the full scale of the problem would result in significant increases in computational cost, rendering the model to be impractical.

Further to this, an issue with the cut-off radius is raised in [32]. The remaining interaction energy was found to be influenced by the cut-off radius. Attempts to find a value of the cut-off radius which provided an absolute minimum of the remaining interaction energy proved inconclusive. However, as the simulations only had a relatively small number of dislocations in them, potentially increasing the dislocation density and using a larger sample size could allow this issue to be resolved. Therefore, for a simulation on the scale of real world dislocation numbers, this issue could resolve itself.

Finally, the structures simulated were all formed in single crystal of FCC and BCC metals. Whilst the FCC and BCC structures are of interest in the Cranfield model, it is more likely that metals modelled using it will be polycrystalline in nature. Extending this to account for polycrystalline metals would require

introducing the effects that grain boundaries have on the formation of structures, as well as incorporating the generation of geometrically necessary dislocations (GND) that are generated at boundaries into the model. Currently, the number of dislocations in the simulation is kept at a constant number, however, by adding in grain boundaries and the generation of GND the dislocation density will need rise during plastic deformations.

7.5 Malygin model

An extensive set of kinetic equations are presented by Malygin in [9], which describe the first three stages of hardening in terms of the dislocation densities. The equations presented consist of microscopic properties, which allow for a description of the evolution of the ensemble of dislocations. The important parameters contained within the equations are the densities of mobile and immobile dislocations, ρ_m and ρ_i, respectively. Statistical averaging is applied to the equations, allowing for a description of the evolution of the whole dislocation ensemble to be achievable. The processes described by the kinetic equations presented in [9] include the formation of lines, bands, cells, the processes of annihilation, double cross slip, Frank-Reid source activation and immobilisation under the conditions of plastic deformation. The basis of the set of kinetic equations is equation (7-2) which gives the ensemble averaged scalar density of dislocations as:

$$\frac{\partial \rho^a}{\partial t} + \nabla \cdot (u^a \rho^a) = n^a u^a + \sum_p \frac{u^a}{\lambda_p^a} \rho^a \qquad \textbf{(7-2)}$$

Where

ρ is the scalar density of dislocations,

u is the velocity of the dislocations

λ_p is the characteristic free path of dislocations before elementary acts of change of density of dislocations.

The superscript a in equation (7-2) denotes that the quantities are for dislocations with the same Burgers vector b^a.

From equation (7-2), further kinetic equations are developed which describe the evolution of the densities of dislocations during plastic deformation. There are two such equations, equation (7-3) which describes the evolution of the density of mobile dislocations ρ_m and equation (7-4) describing the density of immobilised dislocations ρ_i.

$$\frac{\partial \rho_m}{\partial t} + \nabla \cdot (u\rho_m) = nu + \left(\lambda_m^{-1} + \lambda_f^{-1}\right)u\rho_m - (\lambda_{is}^{-1} + h_i\rho_i)u\rho_m - h_a u\rho_m^- \rho_m^+ \quad \textbf{(7-3)}$$

$$\frac{\partial \rho_i}{\partial t} = \lambda_{ie}^{-1} u\rho_m - h_d u\rho_i\rho_m \quad \textbf{(7-4)}$$

where:

λ_m and λ_f are the free paths of screw dislocations between acts of multiplication on obstacles of non-deformation origin and deformation origin respectively.

λ_{is} is the free path of screw dislocations to obstacles destroying their mobility either through immobilisation or annihilation.

h_i is the mean height of edge dipoles.

h_a is the characteristic distance of annihilation of screw dislocations with opposite signs.

λ_{ie} is the free path of screw dislocations between acts of DCS with formation of edge diploes.

h_d is the mean height of edge diploes being destroyed by mobile dislocations.

It is noteworthy that the kinetic equations are developed for deformations that are quasi-static by nature, which is true for low velocity impacts. For high velocity impacts, which include impacts inducing shock waves, the same kinetic equations will be incorrect. The issues of high velocity impacts have been addressed in [39] , where a shock wave model is presented based on the kinetics of dislocations.

Further kinetic equations are presented by Malygin in [35] which describe the formation of the fragmented dislocation structures associated with the fourth and fifth stages of hardening, when a large deformation occurs.

It is worth noting that further to the self-organisation of dislocations methods, a different theory aiming to explain the same experimental observations has been developed by Kuhlmann-Wilsdorf. The theory, known as the low energy dislocation structures (LEDS), proposes that the dislocations reside in positions which minimise the energy of the assembly of dislocations [32] [40] [41]. However, this theory has been widely unaccepted due to the fact that thermal processes are not apparent, which are well known from experimental observations to exist.

7.6 Malygin shock wave model

Following on from the kinetic dislocation equations presented in [9] and subsequent publications [35] [42], Malygin et al. have developed a shock wave model capable of representing the formation and propagation of shock waves from a dislocation point of view.

The model contains two separate parts, representing the two regions of the shock wave; a shock front model and a model for the plastic relaxation region that follows the shock wave front. For both regions a kinetic relationship are derived which govern the shock wave.

The model of the shock wave front is derived starting from a basic force relationship, accounting for plastic strain, ε_{pl} and a wave-induced strain inconsistency, ε_G.

$$\sigma = K_0\varepsilon_G - 2G\varepsilon_{pl} \quad \textbf{(7-5)}$$

Where:

σ is the compressive stress

$K_0 = E/3(1-2v) \approx E$ is the bulk modulus

$G = E/2(1+v)$ is the shear modulus

The first time derivative of equation (7-5) is taken, and the coefficients are substituted in resulting in the kinetic equation

$$\frac{d\sigma}{dt} = E\left(\dot{\varepsilon}_G - \eta\dot{\varepsilon}_{pl}\right) \tag{7-6}$$

with $\eta = \frac{1}{1+\nu}$.

Making use of the Swegle-Grady law, and introducing the coordinate $z = U_1 t - x$, to account for the propagation of the shock front through the metal, where U_1 is the velocity of the shock front, equation (7-6) becomes

$$U_1 \frac{d\sigma}{dz} = E\left(\dot{\varepsilon}_G - \eta K_P \left(\frac{\sigma}{E}\right)^4\right) \tag{7-7}$$

This is simplified by the introduction of dimensionless coordinates and stress, which leaves the kinetic relation, equation (7-7), as:

$$\frac{ds}{dZ} = 1 - s^4 \tag{7-8}$$

Where:

$Z = z/w$, $w = \frac{U_1}{K_P \eta^{1/4}}\left(\frac{K_P}{\dot{\varepsilon}_G}\right)^{3/4}$ is the width of the shock front

$s = \sigma/\sigma_p$, $\sigma_p = E\left(\frac{\dot{\varepsilon}_G}{\eta K_P}\right)^{1/4}$ is the maximum stress.

The model of the shock wave front is completed by the solution to equation (7-8) which is found as:

$$\frac{1}{2}\operatorname{arctanh}\left(\frac{\sigma}{\sigma_P}\right) + \frac{1}{2}\arctan\left(\frac{\sigma}{\sigma_P}\right) = \frac{t}{t_w} - \frac{x}{w} \tag{7-9}$$

t_w is the time of wave front formation and is found mathematically as:

$$t_w = \frac{w}{U_1} = \frac{1}{K_P \eta^{1/4}}\left(\frac{K_P}{\dot{\varepsilon}_G}\right)^{3/4} \tag{7-10}$$

Where:

σ_p is the maximum stress in the wave front,

K_P is the coefficient form the Swegle-Grady law, given in section 6.5.

The second part of the model presented in [39] accounts for the plastic relaxation region behind the shock wave front. The basis of the model for the region of relaxation is the same kinetic equation that is presented in [9] for cases of quasi-static deformation. This equation is used as the dislocation structures and patterning observed in the plastic relaxation region of the shock wave are very similar to those observed in the quasi-static case [10],

$$\frac{\partial \rho(x,t)}{\partial t} = \lambda_D u \frac{\partial \rho}{\partial x^2} + \frac{u}{\lambda_m}\rho + \delta_f u \rho^{3/2} - h_a u \rho^2 \quad \textbf{(7-11)}$$

Equation (7-11) is simplified by the introduction of dimensionless variable $\psi = \rho/\rho_f$ and the dimensionless coordinate and time, $X = x/\Lambda_0$ and $T = t/t_0$, respectively, results in the dimensionless kinetic equation:

$$\frac{\partial \psi(X,T)}{\partial T} = \frac{\partial^2 \psi}{\partial X^2} + \alpha\psi + \psi^{3/2} - \psi^2 \quad \textbf{(7-12)}$$

The solution of equation is found to be in the form of a travelling wave, as:

$$\psi(X,T) = \frac{1}{[f + C\exp(qX + hT)]^2} \quad \textbf{(7-13)}$$

Where

C is a constant of integration, and is set to be equal to f to achieve wave stability,

$f = \frac{1}{2a}\left[(1+4a)^{1/2} - 1\right]$,

$q = \left[\frac{a}{6}\left(\frac{2}{(1+4a)^{1/2}-1}\right)\right]^{1/2}$,

$h = \frac{-2a}{3}\left(\frac{1}{(1+4a)^{1/2}-1} + \frac{5}{4}\right)$.

Substitution of the dimensional variables back into equation (7-13) yields the solution of the kinetic equation for the density of dislocations in dimensional form:

$$\rho(x,t) = \frac{\rho_m}{\left[1 + \exp\left(\frac{x - U_2 t}{\Lambda}\right)\right]^2} \quad \textbf{(7-14)}$$

The density of dislocations, $\rho(x,t)$, is used to calculate the stress and the strain in the second wave. The stress is calculated from

$$\sigma(x,t) = m_T \alpha G b \rho(x,t)^{1/2} \quad \textbf{(7-15)}$$

And the strain:

$$\varepsilon(x,t) = m_T^{-1} \delta_f^{-1} b \rho(x,t)^{1/2} \quad \textbf{(7-16)}$$

Where

m_T is the Taylor factor and α is the coefficient of interactions of dislocations.

The shock wave model outlined in this section, fully presented in [39] required a few comments to be made to determine its relevance in the context of the Cranfield model.

Firstly, the model is structure around knowledge and properties of microstructural dislocations. This is relevant as it has been identified that future developments to the continuum Cranfield model will develop a more multiscale approach, combining microstructural effects into the predominantly continuum scale model. The model is also developed to be relevant for metals with both a FCC and BCC structure, the same materials that are of interest to the Cranfield model.

Further to this, in keeping with the nature of dislocation organisation processes outlined in this chapter, these processes are identified and the model developed with this in mind. This is accounted for by the identification of the that in the region of plastic relaxation, the region behind the shock wave front, the dislocation structures are of the same form as those observed in quasi static

deformation. Using this, the same dislocation-kinetic relationship is used to describe the density of dislocations in this region as was developed for non-shock wave cases.

Next, the shock wave model aims to capture a two-wave structure which is observed experimentally and predicted theoretically, as presented in chapter 6. A two wave structure is achieved by the model being composed of two parts: a spate shock wave front model and a model for the plastic relaxation region following the shock front.

The development of the kinetic equation for the model of the shock wave front includes the dependency of the strain rate on the stress in the form of the Swegle-Grady 4^{th}-Power law. There is vast experimental evidence suggesting the existence in such a law, and therefore the occurrence of the dependence in the calculation of the kinetic equation is a good sign.

Despite the advantages of the shock wave model presented in [39] there are some negative points which need addressing. These include the lack of detail regarding the full implementation and verification of the model. Many of the equations and individual aspects of parts of the model are compared with experimental data in [39], however the model as a whole is not verified. There is indication in [39] that verification has been done, however this will be the subject of a future publication. There is no indication given as to the degree of success of the verification process. For any future consideration of this model, a full verification of it would need to be carried out, or observed in literature.

7.7 Usefulness for Cranfield model

Understanding of the dislocation processes which are apparent during plastic deformation is very useful for in aiding a full understanding of the nature of plastic deformation and in particular the plastic evolution of metals.

Whilst the method put forward by Malygin in [9] gives a very complete dislocation – kinetic set of equations governing the various processes occurring

during plastic deformation and the associated strain hardening, a large number of equations are required. It will be seen in the following chapter that a similar dislocation model, which again uses the evolution of the densities of dislocations, is much simpler with the results from the model showing good agreement with experimental data.

7.8 Summary

The self-organisational processes of dislocations method provides a description of dislocation patterns which are formed during the process of plastic deformation. Understanding the patterns formed, and the mechanisms of formation are of use as these include dislocation motions, annihilation and multiplication, all of which have a direct impact on the evolution of plastic deformation.

It has been show by Sangi that the theoretical reason for the formation of structures can be used to reproduce the structures observed experimentally, with the various different structures forming depending on the conditions of the simulation.

Dislocation – kinetic equations are provided by Malygin describing the evolution of the densities of dislocations during plastic deformation, both in a quasi-static case and in a shock wave situation. This method is compared in the following section to an alternative dislocation based method of plasticity.

8 Mayer's Model

The second model which is identified for analysis is the latest mobile and immobile dislocation based model. This model, which was developed by Mayer et al. [10], is described in this chapter with a focus on how the model meets the requirements for the future development of the Cranfield model, as well as identifying the draw backs of the method. This chapter contains five sections; section 8.1 looks at the formulation of the model, section 8.2 discusses the advantages of this method, with 8.3 discussing the relative disadvantages. A comparison between this shock wave model and the shock model presented in the previous chapter is then presented, followed by a summary of the chapter in section 8.5.

The model proposed by Mayer et al [10] is a continuum mechanics based model capable of modelling the plastic deformation and fracture of metals under shock wave propagation. This model has been chosen as it includes microstructural effects, and claims to have the capability of reproducing the superelastic precursor wave observed for a very short time period after shock loading is applied.

8.1 Formulation of model

The model presented by Meyer et al. in [10] describes dislocation plasticity and fracture of metals under shock loading conditions. The model describes plasticity making use of information about the state of the defect sub-systems which include the kinetics of dislocations and the formation and propagation of micro-cracks. These two processes are considered as two separate processes, with a separate tensor derived and calculated for each; the tensor w_{ik} for plastic deformation and W_{ik} for the process of fracture.

Mayer's model is formulated as a combination of a model of dislocation plasticity and fracture, continuum mechanics equation and the wide-range equation of state [43]

The basis of the model is a series of continuum mechanics equations, which govern the rates of change of mass, momentum and energy. The equations are used in a Lagrangian form and are given as:

$$\frac{1}{\rho}\frac{d\rho}{dt} = -\sum_{k=1}^{N}\left(\frac{\partial v_k}{\partial x_k} + \frac{dW_{kk}}{dt}\right) \tag{8-1}$$

$$\rho\frac{dv_i}{dt} = \sum_{k=1}^{N}\frac{\partial \sigma_{ik}}{\partial x_k} \tag{8-2}$$

$$\rho\frac{dU}{dt} = \sum_{k=1}^{N}\left(-P\left(\frac{\partial v_k}{\partial x_k} + \frac{dW_{kk}}{dt}\right) + \sum_{i=1}^{N} S_{ik}\frac{dw_{ik}}{dt}\right) \tag{8-3}$$

Further to the continuum mechanics equations, a series of equations is presented describing the kinetics of dislocations which include terms for mobile and immobilised dislocations. The change in densities of the mobile and immobile dislocations are taken into account along with the generation rates of each. The four equations are given as:

$$\frac{d\rho_D^\beta}{dt} = Q_D^\beta - Q_I^\beta - k_a b\left|V_D^\beta\right|\rho_D^\beta\left(2\rho_D^\beta + \rho_I^\beta\right) \tag{8-4}$$

$$\frac{d\rho_I^\beta}{dt} = Q_I^\beta - k_a b\left|V_D^\beta\right|\rho_D^\beta\rho_I^\beta \tag{8-5}$$

$$Q_D^\beta = k_g b\left[\frac{2Bc_t^2\left(V_D^\beta\right)^2}{\sqrt{1-\left(V_D^\beta/c_t\right)^2}} + bY\left|V_D^\beta\right|\right]\rho_D^\beta \tag{8-6}$$

$$Q_I^\beta = V_I\left(\rho_D^\beta - \rho_0\right)\sqrt{\rho_I^\beta} \tag{8-7}$$

Where ρ_D^β is the density of mobile dislocations, ρ_I^β is the density of immobilised dislocations, Q_D^β is the generation rate of mobile dislocations, Q_I^β is the

immobilisation rate, b is the modulus of the Burgers vector, k_a is the coefficient of annihilation of dislocations, B is the friction coefficient, Y is the yield strength and K_g is the coefficient of generation. The superscript β numerates the slip system of the dislocations.

From the four equations describing dislocation dynamics, equations (8-4), (8-5), (8-6) and (8-7), it is apparent that mobile and immobile dislocations are treated as two separate processes. Overall, the complete model consists of seventeen equations which are numerically solved, and contain eleven material constants. The complete set of equations is presented in appendix A.

The model is presented as being verified. The verification reported in [10] was done by simulation of plate impact tests of aluminium, copper and nickel. The verification shows proof that the model reproduces similar behaviour to that which is observed in a similar experimental set up.

8.2 Advantages

The model of Mayer has many advantages which would make it appropriate for inclusion into the current Cranfield model. These advantages will be discussed in this section.

An appealing feature of Mayer's model is the relative simplicity of it. The model requires only eleven material parameters to describe and reproduce complex behaviour encountered in a high velocity impact.

Plastic deformation of metals is due in a large part to the formation and motion of dislocations. Therefore, a model of plasticity which describes the processes of dislocations would appear to be most appropriate. Mayer's model does this, with the formulation of the model accounting for the generation, motion and immobilisation of dislocations. A further advantage of the method in which dislocation motions are accounted for in the Mayer's model is the fact that continuum level equations are used in the description of atomistic scale effects. This introduces the multi-scale modelling aspect which would be needed for future inclusion into the Cranfield model, which is primarily developed in a continuum framework.

The results produced by Mayer's model show interesting properties. One of these results is shown in Figure 8-1, which consists of plots of the longitudinal stress against distance for shock waves at different time intervals after impact.

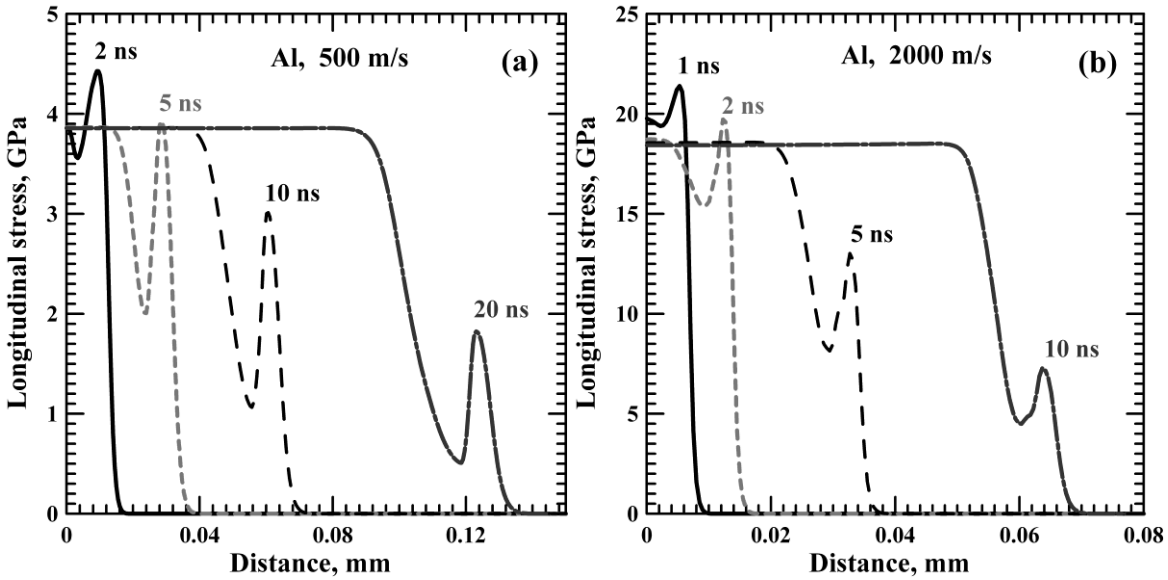

Figure 8-1: Model results for the formation and evolution of shock waves resulting from an impact velocity of (a) 500ms^{-1} and (b) 2000ms^{-1} in aluminium shown at time intervals after the impact [10]

It is observed in Figure 8-1 that an elastic precursor wave and a plastic shock front are formed for both of the impact velocities displayed. It can be seen in Figure 8-1 that the amplitude of the elastic precursor wave is initially greater than the amplitude of the plastic shock wave. Within a short time period, ~20ns, the elastic precursor decays to an amplitude more in line with the dynamical elastic limit. This behaviour is representative of a superelastic precursor wave, and the model by Mayer et al. is currently the only model in which this can be reproduced.

Distinction can also be made in Figure 8-1 between strong shock and weak shock. For the lower of the two impact velocities (500ms^{-1}), a weak shock would be formed. The slope of the elastic precursor is observed to be steeper than that of the plastic shock wave. For the higher of the two impact velocities, Figure 8-1(b), the slope of the precursor is observed to be the same as for that of the plastic shock wave.

8.3 Disadvantages

As with any model there are a few disadvantages or limitations with Mayer's model.

A limitation of the model was observed during the verification process. The verification process, which consisted of simulation of plate impact experiments and comparisons with experimental data, shown that the model successfully reproduced a plastic shock wave and an unloading wave. Spall fracture can be observed in the verification results along with reverberations of the spall pulse. However, as can be seen from Figure 8-2 the amplitude of the reverberations of the spall pulse are larger than is observed experimentally. This is consistent through all of the result shown for the verification of the model in [10].

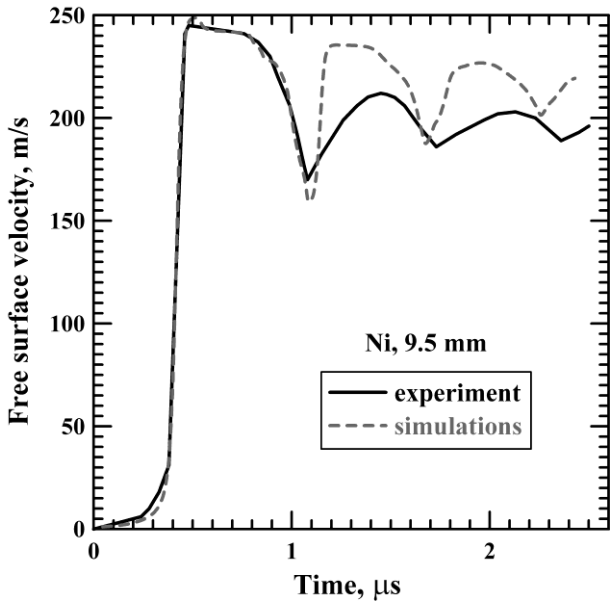

Figure 8-2: Comparison of experimental and simulated data for free surface velocity for a 9.5mm Nickel target being impacted by a 0.2mm thick aluminium target plate at 470ms^{-1} [10]

This overestimate of the amplitude of the spall pulse reverberations is an indicator that there is an additional dissipative loss [10] which is not accounted for in the model. To be completely thermodynamically consistent, further investigation into this additional loss would be required.

The verification of the model was carried out for three separate metals; aluminium, copper and nickel, all of which have a FCC structure. As outlined in section 2, the metallic structures of interest for the Cranfield model are both FCC and BCC metals. The formulation of the model theoretically allows for different structures to be modelled as parameters of the slip systems of interest are included, as well as the Burgers vector. These parameters are dependent on the crystal structure of the metal being modelled, and are calculated directly from an analysis of the crystal structure.

Finally, the model only considers dislocation kinetics for deformation. Whilst this is the dominant process in most materials, other processes, such as twinning, could also have an impact. Inclusion of other deformation processes however might improve the accuracy of the model slightly, however, for the additional level of complexity and computation cost it would likely be more of a hindrance than an advantage to include such mechanisms.

8.4 Comparison of shock wave models

Two shock wave models have been outlined, the model of Malygin [39] in section 7.6 and the model developed by Mayer [10] in the present chapter. Both of the models being investigated are dislocation based models, which make use of calculations of the density of dislocations in a metal during shock loading. Both of the models have advantages which will be discussed and compared in this section.

Advantages of Mayer model: the model has been implemented and results published. The results show reproduction of a superelastic precursor as well as prediction of spall pulses. The model was developed with a continuum basis, the same basis as the framework of the Cranfield model.

Advantages of Malygin model: the shock wave model incorporates the Swegle-Grady 4^{th}-power law in the strain rate description, as well as providing an explanation of the law. The individual types of dislocation are accounted for, the Mayer model just treats mobile and immobile, whereas the Malygin model

differentiates between GND, statistically stored dislocations, and screw and edge components.

Both models make use of the Taylor relation for stress evolution, this describes the strain hardening observed during the shock propagation processes.

The Mayer model provides a better description of the material response to the shock wave propagation, whereas the Malygin model provides a more depth discussion of the form of shock wave itself. The spallation pulses that are observed in the results of the Mayer model are comparable to that which is observed experimentally, this result is unseen in the Malygin model from the evidence of its capabilities that are available. This indicates that the Mayer model is relevant for longer time scales than the Malygin model, despite the fact that phenomena, such as the super elastic precursor wave, which are observed for only very short time periods are captured.

As the model of Mayer has been verified and proven to reproduce known observations in the material response to shock loading, and due to its ability to show both short and long time scale responses, in the context of the Cranfield model, it is the more suitable of the two shock wave models considered to be combined in the future into the Cranfield model.

8.5 Summary

The model of Mayer et al. meets the requirements for inclusion into the Cranfield model by meeting the following criteria:

- Capable of modelling plasticity and fracture at shock loading – a requirement of the Cranfield model to allow it to accurately reproduce high velocity impacts.
- Multi-scale – the molecular dynamic scale dislocations are described in a predominantly continuum scale framework.
- Superelastic precursor wave is observed for short time periods after impact – in line with recent short pulse (femtoseconds) laser experiments.

There are significant advantages to Mayer's model over the dislocation – kinetic equations and shock wave model of Malygin. Due to these criteria and also the

relative simplicity of the model it would be recommended for further analysis into the plasticity part of the model, to numerically verify the reported results and assess the full capability of the model, before potentially including the model as a replacement for the MTS part of the Cranfield model. The fracture part of the model is seen to produce results less accurate than the damage part of the current Cranfield model, therefore only the plasticity part of the Mayer's model will be considered for future work.

9 Virial Stress

The third method to be looked at is the application of the virial stress tensor to cases of shock loading. The virial stress tensor is a calculation of the continuum scale Cauchy stress using purely atomistic variables. This is of potential advantage to future developments of the Cranfield model as it allows microscale properties to be fed directly up to the continuum scale of the overall model. This chapter contains two main components: firstly the virial stress is derived by considering the forces experienced by the atoms in the metal, the major drawbacks of this are then discussed with a potential solution then being described. The chapter is then concluded with the summary of the findings.

The future development of the Cranfield model relies on the inclusion of micro-scale effects into the continuum mechanical model. In order to achieve this, the concept of multi-scale modelling is required. This requires the use of modelling techniques which are applied for different times and length scales to be used together. It has been identified that the processes of plastic deformation, including plastic deformation from shock loading, are predominantly explained by microstructural effects, mainly dislocation processes. As a result of this it is necessary to include in the current Cranfield model a method of accounting for microscale processes but maintaining the continuum framework the current model is developed within.

One such way of achieving this is to calculate the macroscopic, continuum scale properties of the system using purely microscale effects. There exists a method of calculating the Cauchy stress tensor, known as the virial stress, which allows for the calculation of the continuum scale Cauchy stress, using purely atomistic scale properties of the system. The stress is calculated by knowledge of forces between individual atoms within the system. The virial stress tensor is derived in the following section.

9.1 Derivation of Virial stress tensor

The Virial stress tensor is derived here for a system consisting of N number of particles. The derivation followed here is based on the derivation of the virial stress tensor presented in [44].

To derive the stress tensor it is first important to define the position of the particle. This is done with respect to the centre of mass of the system as

$$\boldsymbol{x}_\alpha = \boldsymbol{x} + \boldsymbol{r}_\alpha \tag{9-1}$$

Where $\boldsymbol{x}_\alpha$ is the position of particle α, $\boldsymbol{x}$ is the position of the centre of mass of the system and $\boldsymbol{r}_\alpha$ is the position of α relative to the position of the centre of mass of the system.

Making use of Newton's second law, equation (9-2), which states that the force on a particle, $\boldsymbol{f}_\alpha$ is equal to its rate of change of linear momentum, $\boldsymbol{p}_\alpha$, the virial stress tensor can be derived.

$$\boldsymbol{f}_\alpha = \dot{\boldsymbol{p}}_\alpha \tag{9-2}$$

Taking the tensor product of both sides of Newton's second law with the position of the particle α relative to the centre of mass of the system, $\boldsymbol{r}_\alpha$, yields the following relation:

$$\boldsymbol{r}_\alpha \otimes \boldsymbol{f}_\alpha = \boldsymbol{r}_\alpha \otimes \dot{\boldsymbol{p}}_\alpha \tag{9-3}$$

The right hand side of equation (9-3) can be written as a result of the product rule of differentiation as:

$$\frac{d}{dt}(\boldsymbol{r}_\alpha \otimes \boldsymbol{p}_\alpha) = (\dot{\boldsymbol{r}}_\alpha \otimes \boldsymbol{p}_\alpha) + (\boldsymbol{r}_\alpha \otimes \dot{\boldsymbol{p}}_\alpha) \tag{9-4}$$

Including this in equation (9-3) leads to

$$\frac{d}{dt}(\boldsymbol{r}_\alpha \otimes \boldsymbol{p}_\alpha) = (\boldsymbol{r}_\alpha \otimes \boldsymbol{f}_\alpha) + (\boldsymbol{v}_\alpha^{rel} \otimes \boldsymbol{p}_\alpha) \tag{9-5}$$

Where $\boldsymbol{v}_\alpha^{rel} = \dot{\boldsymbol{r}}_\alpha$ is the velocity of particle α relative to the centre of mass of the system.

The two terms on the right hand side of equation (9-5) can be written as the virial tensor and the kinetic tensor:

$\boldsymbol{\mathcal{W}}_\alpha = \boldsymbol{r}_\alpha \otimes \boldsymbol{f}_\alpha =$ the Virial tensor

$\boldsymbol{\mathcal{T}}_\alpha = \frac{1}{2}(\boldsymbol{v}_\alpha^{rel} \otimes \boldsymbol{p}_\alpha) =$ the Kinetic tensor

This results in relation (9-6) which is referred to as the dynamical virial theorem.

$$\frac{d}{dt}(\boldsymbol{r}_\alpha \otimes \boldsymbol{p}_\alpha) = \boldsymbol{\mathcal{W}}_\alpha + 2\boldsymbol{\mathcal{T}}_\alpha \tag{9-6}$$

When using multi-scale modelling, the time scales as well as the length scales are different as shown in Figure 9-1. Therefore, it is needed to define an atomistic timescale in which the atoms vibrate due to thermal vibrations from their stationary points. It would not be possible or feasible to map each vibration, so instead an average is taken over the atomistic time, τ. For an arbitrary function, f, the average is calculated by:

$$\bar{f} = \frac{1}{\tau}\int_0^\tau f(t)dt \tag{9-7}$$

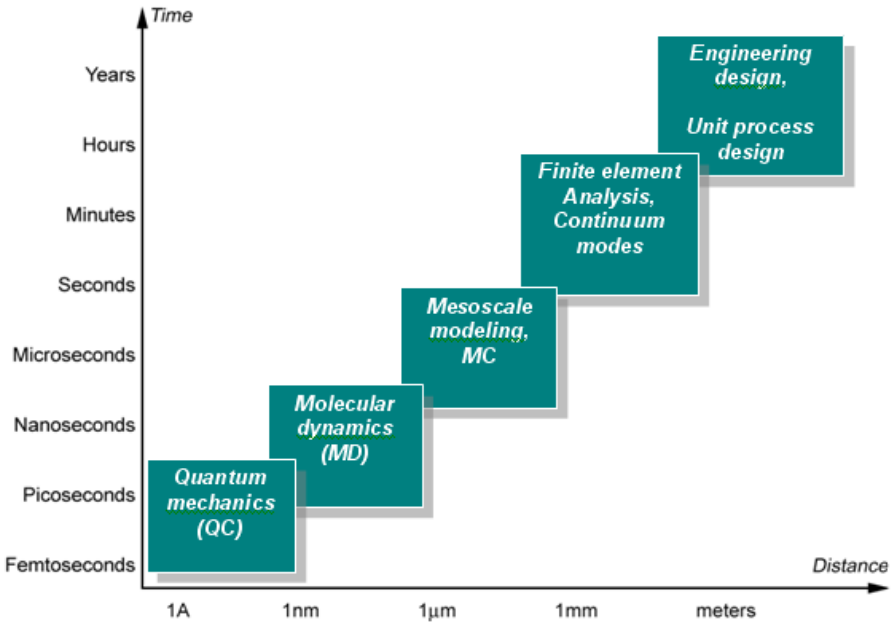

Figure 9-1: Diagram showing relationship between the time scales and length scales of different scales of modelling [45]

Applying the average in the same way to the dynamical virial theorem accounts for thermal vibrations in the stress calculations

$$\frac{1}{\tau}(\boldsymbol{r}_\alpha \otimes \boldsymbol{p}_\alpha)|_0^\tau = \overline{\boldsymbol{\mathcal{W}}}_\alpha + 2\overline{\boldsymbol{\mathcal{T}}}_\alpha \tag{9-8}$$

By setting the atomistic time to be sufficiently large, the term on the left hand side of equation (9-8) can be made as small as required. This allows for the relation to be written:

$$\overline{\boldsymbol{\mathcal{W}}}_\alpha = -2\overline{\boldsymbol{\mathcal{T}}}_\alpha \tag{9-9}$$

Taking the sum over all particles in the system results in the tensor virial theorem:

$$\overline{\boldsymbol{\mathcal{W}}} = -2\overline{\boldsymbol{\mathcal{T}}} \tag{9-10}$$

Where $\overline{\boldsymbol{\mathcal{W}}} = \sum_\alpha \overline{\boldsymbol{r}_\alpha \otimes \boldsymbol{f}_\alpha}$ and $\overline{\boldsymbol{\mathcal{T}}} = \frac{1}{2}\sum_\alpha m_\alpha \overline{\boldsymbol{v}_\alpha^{rel} \otimes \dot{\boldsymbol{x}}_\alpha}$.

This can be further developed by simplifying the kinetic tensor. In order to do this it is first necessary to derive an identity. This is done by considering the position of the centre of mass.

The position of the centre of mass is calculated

$$\boldsymbol{x} = \frac{\sum_\alpha m_\alpha \boldsymbol{x}_\alpha}{\sum_\alpha m_\alpha} \tag{9-11}$$

From this it can be observed that the identity (9-12) holds.

$$\sum_\alpha m_\alpha \boldsymbol{r}_\alpha = \boldsymbol{0} \quad \Rightarrow \quad \sum_\alpha m_\alpha \boldsymbol{v}_\alpha^{rel} = \boldsymbol{0} \tag{9-12}$$

Substituting equation (9-1) into equation (9-10):

$$\overline{\boldsymbol{\mathcal{T}}} = \frac{1}{2}\sum_\alpha m_\alpha \overline{\boldsymbol{v}_\alpha^{rel} \otimes \boldsymbol{v}_\alpha^{rel}} + \left[\overline{\sum_\alpha m_\alpha \boldsymbol{v}_\alpha^{rel}}\right] \otimes \dot{\boldsymbol{x}} \tag{9-13}$$

Making use of the identity (9-12) and observing that, on an atomistic timescale the position of the centre of mass of the system is unchanging allows for the above expression to be simplified to

$$\bar{\boldsymbol{T}} = \frac{1}{2}\sum_{\alpha} m_{\alpha}\overline{\boldsymbol{v}_{\alpha}^{rel} \otimes \boldsymbol{v}_{\alpha}^{rel}} \tag{9-14}$$

This is the final simplified kinetic tensor which is included in the definition of the virial stress tensor.

To complete the full derivation of the virial stress tensor, the virial tensor, $\overline{\boldsymbol{W}}$, needs to be expanded. This is done through splitting the force acting on particle α into two components: the internal force – the force which results from interaction of the particle with other particles in the system, and the external force – the force which is apparent due to interactions with externally applied fields and atoms outside of the system.

Due to the splitting of the force into separate terms, the virial tensor can also be split to account for this, into external and internal parts which correspond to the external force and the internal force respectively.

$$\overline{\boldsymbol{W}} = \overline{\boldsymbol{W}}_{int} + \overline{\boldsymbol{W}}_{ext} = \sum_{\alpha}\overline{\boldsymbol{r}_{\alpha} \otimes \boldsymbol{f}_{\alpha}^{int}} + \sum_{\alpha}\overline{\boldsymbol{r}_{\alpha} \otimes \boldsymbol{f}_{\alpha}^{ext}} \tag{9-15}$$

The external virial tensor can be expanded and written in terms of continuum variables in the form of a body force, $\rho\boldsymbol{b}$, and the traction, $\boldsymbol{t}$, which the surrounding medium applies to the system. This is applied as:

$$\overline{\boldsymbol{W}}_{ext} = \sum_{\alpha}\overline{\boldsymbol{r}_{\alpha} \otimes \boldsymbol{f}_{\alpha}^{ext}} := \int_{\Omega} \boldsymbol{x} \otimes \rho\boldsymbol{b}dV + \int_{\partial\Omega} \boldsymbol{x} \otimes \boldsymbol{t}dA \tag{9-16}$$

Applying Cauchy's stress theorem allows for the traction to be replaced with the Cauchy stress and a vector normal to the surface of integration. Substituting this in and applying the divergence theorem gives the expression:

$$\overline{\boldsymbol{W}}_{ext} = \int_{\Omega} [\boldsymbol{x} \otimes \rho\boldsymbol{b} + div_x(\boldsymbol{x} \otimes \boldsymbol{\sigma})]dV = \int_{\Omega} [\boldsymbol{\sigma}^T + \boldsymbol{x} \otimes (div_x\boldsymbol{\sigma} + \rho\boldsymbol{b})]dV \tag{9-17}$$

This is simplified by using the result that, under equilibrium conditions, $(div_x\boldsymbol{\sigma} + \rho\boldsymbol{b}) = \mathbf{0}$. Therefore

$$\overline{\boldsymbol{\mathcal{W}}}_{ext} = V\boldsymbol{\sigma}^T \tag{9-18}$$

The continuum stress field, the Cauchy stress is defined as the average value of $\boldsymbol{\sigma}$ over the volume Ω:

$$\boldsymbol{\sigma}_{av} := \frac{1}{V}\int_{\Omega} \boldsymbol{\sigma} dV \tag{9-19}$$

Substituting equation (9-18) into equation (9-15) and then into the tensor virial theorem, equation (9-11) and expression for the virial stress is obtained as:

$$\boldsymbol{\sigma}_{av} = -\frac{1}{V}[\overline{\boldsymbol{\mathcal{W}}}_{int} + 2\overline{\boldsymbol{\mathcal{T}}}]^T \tag{9-20}$$

Which when the full definitions for the internal virial tensor and the kinetic tensor are substituted in, the virial stress tensor is written purely in terms of atomistic variables:

$$\boldsymbol{\sigma}_{av} = -\frac{1}{V}\left[\sum_{\alpha} \overline{\boldsymbol{f}_{\alpha}^{int} \otimes \boldsymbol{r}_{\alpha}} + \sum_{\alpha} m_{\alpha}\overline{\boldsymbol{v}_{\alpha}^{rel} \otimes \boldsymbol{v}_{\alpha}^{rel}}\right] \tag{9-21}$$

As the Virial stress tensor provides a link between the continuum scale and the molecular dynamic microscale the applicability of the virial stress to the Cranfield model, which includes deformation under shock wave loading, is investigated. The advantage of using a multiscale approach to modelling deformation under shock loading is due to the varying time scales inherent in the calculation; behaviour of the system over short, molecular dynamics timescales can be captured in a model built in a continuum mechanics model with relatively long time scales.

It is apparent that, due to the time averaging process which determined the average position of the particle about the equilibrium position, accounting for thermal vibrations, that the virial stress tensor calculation is only valid for systems in macroscopic equilibrium.

However, it is apparent that calculation of the stress tensor using purely atomistic properties is achievable for systems not in macroscopic equilibrium. This is achieved by using the so-called Hardy equations. These equations have similar form to the virial stress equation, however additional localisation functions are included.

Unlike the virial stress equation, equation (9-21), which is derived starting from the consideration of forces on each atom in the system, the Hardy's stress equation is derived using the conservation equations of continuum mechanics in spatial form as a starting point [46].

$$\frac{\partial \rho}{\partial t} = \nabla \cdot (\rho v) \tag{9-22}$$

$$\frac{\partial p}{\partial t} = \nabla \cdot (\sigma - \rho v \otimes v) \tag{9-23}$$

$$\frac{\partial e}{\partial t} = \nabla \cdot (\sigma \cdot v - ev - q) \tag{9-24}$$

The continuum fields contained within equations (9-22), (9-23) and (9-24) are defined to be

$$\rho(x,t) = \sum_{\alpha}^{N} m^{\alpha} \psi(x^{\alpha} - x) \tag{9-25}$$

$$p(x,t) = \sum_{\alpha}^{N} m^{\alpha} v^{\alpha} \psi(x^{\alpha} - x) \tag{9-26}$$

$$e(x,t) = \sum_{\alpha}^{N} \left\{ \frac{1}{2} m^{\alpha} (v^{\alpha 2}) + \phi^{\alpha} \right\} \psi(x^{\alpha} - x) \tag{9-27}$$

Here the atomistic variables of mass, m^{α} and potential energy, ϕ^{α}, for the atom α in the system are introduced. The function $\psi(x^{\alpha} - x)$is the localisation function, which effectively spreads out the properties of the atoms in the system allowing them to contribute to the properties of the continuum at the position x

at time t [46]. In order for the localisation function to be introduced in this way it must have dimensions of inverse volume.

Substituting definitions (9-25), (9-26) and (9-27) into the continuity equations, and recognising constraints on the localisation function, and making four key assumptions regarding the form of the potential energy and forces between atoms, equation (9-28) is developed.

In order for the localisation function to be introduced its dimensions must be that of inverse volume.

$$\sigma_H(x,t) = -\left\{\frac{1}{2}\sum_{\alpha=1}^{N}\sum_{\beta\neq\alpha}^{N} x_{\alpha\beta} \otimes F_{\alpha\beta} B^{\alpha\beta}(x) + \sum_{\alpha=1}^{N} m_\alpha \tilde{v}_\alpha \otimes \tilde{v}_\alpha \psi(x_\alpha - x)\right\} \quad \textbf{(9-28)}$$

Equation (9-28) is the Hardy stress calculation.

The constraints imposed on the localisation function are as follows [46]:

1. The function is normalised
2. The spatial gradient of the localisation function is equivalent to the negative of the gradient of ψ with respect to its argument:

$$\frac{\partial \psi(r)}{\partial x} = \frac{\partial \psi(r)}{\partial r}\frac{\partial r}{\partial x} = -\frac{\partial \psi(r)}{\partial r}$$

3. The bond function:

$$B^{\alpha\beta}(x) \equiv \int_0^1 \psi\left(\lambda x^{\alpha\beta} + x^\beta - x\right) d\lambda$$

between atoms α and β, represents a weighted function of the bond length segment which lies within the characteristic volume. Taking the derivative of the integrand with respect to λ and then integrating from $\lambda = 0$ to 1it is found:

$$\psi(x^\alpha - x) - \psi\left(x^\beta - x\right) = -x^{\alpha\beta} \cdot \frac{\partial}{\partial x} B^{\alpha\beta}(x)$$

As well as these three constraints on the localisation function, for a complete derivation of the Hardy's stress it is important to highlight four key assumptions which were made by Hardy regarding the potential energy and forces between atoms [46]. These are:

i) The total potential energy of the system can be considered to be a summation of the potential energies of each atom within the system.

ii) Similarly, the force experienced by any atom is written as a summation

$$F^{\alpha} = -\frac{\partial \phi}{\partial x^{\alpha}} = -\sum_{\alpha=1}^{N} F^{\alpha\beta}$$

Here $F^{\alpha\beta}$ represents the force exerted on atom α by atom β.

iii) The atomic potentials are only dependent on the interatomic distances.

iv) Each atomic potential energy depends only on the distances between the atoms under consideration in the calculation.

It is noted in [46] that the choice of characteristic volume can yield other atomistic stress definitions. The example of the virial stress is used; if the characteristic volume is taken to be the entire system of atoms and the system is stationary, then the resulting stress definition will be identical to the virial stress definition [46]. This result shows a level of validity to the derived Hardy stress.

The robustness of the Hardy stress is confirmed as a similar derivation carried out by Murdoch [47], whilst unaware of the Hardy derivation, yielded the same result.

It is indicated in [48] and [47] that the Hardy stress can be used in a system under shock loading.

9.2 Summary

The virial stress tensor has been derived and discussed. It is determined that due to the time averaging process inherent in the derivation of the virial stress, the tensor can only calculate an average stress, requiring the system to be in macroscopic equilibrium.

A modified atomistic stress tensor is then derived, the Hardy stress, which does not rely on time averaging, therefore not requiring the system to be in

macroscopic equilibrium. This more robust stress calculation can be applied to systems undergoing shock deformation.

10 Conclusions

A full review of the current Cranfield orthotropic material model has been carried out with the areas of potential improvement being identified. The areas identified were the plasticity part of the model as well as the shock wave representation. The improvements suggested are to allow for the model to reproduce phenomena observed over very short timescales (nanoseconds).

Three methods of modelling have been identified as relevant for future investigations, including implementation, to allow for microstructural effects to be captured by the Cranfield model. Two of these methods are plasticity models available in literature, with the third allowing for multiscale effects to be captured. These methods are:

- Self-organisational processes of dislocations
- Latest mobile/immobile dislocation based method, proposed by Mayer
- Application of an atomistic stress tensor

The self-organisational processes of dislocations model has been identified as relevant for future investigation as it is developed for both quasi-static and shock deformation, but further to this, the Swegle- Grady 4^{th}–power law naturally arises in the derivation of the shock wave model.

The Mayer's model is a constitutive model which treats mobile and immobile dislocations separately. The model is relatively simple, containing few material parameters, but appears from the initial published results to capture nanosecond shock wave behaviour.

The atomistic stress tensor has been derived from considering the forces on individual atoms in a system, resulting in the calculation of the continuum scale Cauchy stress. It is determined that this method alone is not relevant for modelling dynamic shock loaded systems as, due to the averaging process involved in the calculation, only an average stress for a system in macroscopic equilibrium can be obtained. Modification of this method, using the addition of localisation functions, has been identified as a possible stress calculation which remains purely in terms of atomistic terms.

The recommendations for future work following this work are:

- Implementation of both the Self-organisational processes and the Mayer's model into the DYNA3D hydrocode
- Validate implemented models to confirm their capabilities
- Numerically investigate the applicability of the atomistic stress tensor, including for different localisation functions to determine the most appropriate.
- Investigate whether the virial stress tensor can be used to aid the understanding of the physical origins of the Swegle-Grady 4th – power law.

REFERENCES

[1] C. Qi, M. Wang and Q. Qian, “Strain-rate effects on the strength and fragmentation size of rocks,” *International journal of impact engineering,* vol. 36, pp. 1355-1364, 2009.

[2] G. Johnson and W. Cook, “A constitutive model and data for metals subjected to large strain, high strain rates and high temperatures,” in *Proceedings of the 7th International Symposium on Ballistics*, The Hague, 1983.

[3] L. Schwer, “DYNAlook - 6th European LS-DYNA Users' conference: Optional Strain-Rate forms for the Johnson Cook Constitutive Model and the Role of the Parameter Epsilon_0,” 2007. [Online]. Available: http://www.dynalook.com/european-conf-2007/optional-strain-rate-forms-for-the-johnson-cook.pdf. [Accessed 04 08 2014].

[4] M. A. Meyers, Dynamic behaviour of materials, New York: John Wiley and Sons, 1994.

[5] D. J. Steinberg, S. G. Cochran and M. W. Guinan, “A constitutive model applicable at high-strain rate,” *Journal of Applied Physics,* vol. 51, p. 1498, 1980.

[6] V. Panov, “Modelling of behaviour of metals at high strain rates,” PhD Thesis, Cranfield University, Cranfield University, 2006.

[7] D. J. Steinberg and C. M. Lund, “A constitutive model for strain rates from 10^-4 to 10^6 s^-1,” *Journal of Applied Physics,* vol. 65, p. 1528, 1989.

[8] B. Banerjee and A. S. Bhawlkar, “An extended mechanical threshold stress plasticity model: Modelling 6061-T6 Aluminium alloy,” *Journal of mechanics of materals and structures,* vol. 3, no. 3, pp. 391-424, 2008.

[9] G. A. Malygin, “Dislocation self-organization processes and crystal

plasticity," *Physics - Uspekhi,* vol. 42, no. 9, pp. 887-916, 1999.

[10] A. E. Mayer, K. V. Khishchenko, P. R. Levashov and P. N. Mayer, "Modeling of plasticity and fracture of metals at shock loading," *Journal of applied physics,* vol. 113, no. 19, 2013.

[11] D. R. Askeland, The science and engineering of materials, London: Chapman and Hall, 1984.

[12] R. A. Higgins, Properties of Engineering Materials, London: Edward Arnold, 1994.

[13] "Slip (materials science) page," 2013. [Online]. Available: http://en.wikipedia.org/wiki/slip(materials science). [Accessed 4 6 2013].

[14] F. de Juan, "Dislocations and torsion in grapene and related systems," 2010. [Online]. Available: http://inspirehep.net/record/1094489/plots. [Accessed 15 April 2013].

[15] D. Pai, "Dislocations and plastic deformation," Aero and Auto dept. MIT Manipal.

[16] "Line defects," Mech Look, 20 07 2012. [Online]. Available: http://www.mechlook.com/line-defects/. [Accessed 02 07 2013].

[17] R. E. Smallman and R. J. Bishop, Modern Physical Metallurgy and Materials Engineering, Oxford: Butterworth Heinemann, 1999.

[18] A. Donald, "Obstacles to dislocation motion," [Online]. Available: http://www.bss.phy.cam.ac.uk/~amd3/teaching/A_Donald/Crystalline_solids_2.htm. [Accessed 02 07 2013].

[19] R. W. K. Honeycombe, The Plastic Deformation of Metals, London: Edward Arnold, 1968.

[20] C. Malla Reddy, G. Rama Krishna and S. Ghosh, "Mechanical properties

of molecular crystals - application to crystral engineering," *CrystEngComm,* vol. 12, no. 8, pp. 2296-2314, 2010.

[21] G. E. Mase, Schaum's outline series: Theory and problems of continuum mechanics, New York: McGraw-Hill, 1970.

[22] G. A. Holzapfel, Nonlinar solid mechanics a continuum approach for engineering, Chichester: Wiley, 2000.

[23] N. Djordjevic, "Modelling the inselastic behaviour of orthotropic material under dynamic loading including high velocity impact (PhD Thesis)," Cranfield University, Cranfield, 2011.

[24] M. M. Abbott and H. C. v. Ness, Schaum's outline series Theory and problems of thermodynamics, New York: McGraw - Hill , 1972.

[25] S. J. Blundell and K. M. Blundell, Concepts in Thermal Physics, Oxford: Oxford University Press, 2006.

[26] R. Vignjevic, J. Campbell, N. K. Bourne and N. Djordjevic, "Modelling shock waves in orthotropic elastic materials," *Journal of applied physics,* vol. 104, no. 4, 2008.

[27] N. Djordjevic, *Impact Dynamics lecture notes,* Cranfield: Cranfield University, 2012.

[28] J. A. Zukas, High velocity impact dynamics, New York: Wiley, 1990.

[29] T. Neal, "Second Hugoniot relationship for solids," *J.Phys.Chem.Solids,* vol. 38, pp. 225-231, 1977.

[30] D. E. Grady, "Structured shock waves and the fourth-power law," *Journal of applied physics,* vol. 107, no. 1, 2010.

[31] G. A. Malygin, S. L. Ogarkov and A. V. Andriyash, "On the power-law pressure dependence of the plastic strain rate of crystals under intense

shock wave loading," *Physics of the solid state,* vol. 55, no. 4, pp. 780-786, 2013.

[32] D. Sangi, E. A. Steck and S. Bross, "Simulation of self-organised dislocation structures in f.c.c. and b.c.c. single crystals," *Acta Mechanica,* vol. 132, no. 1-4, pp. 93-112, 1999.

[33] D. Kuhlmann-Wilsdorf, "Advancing towards constitutive equations for the metal industry via the LEDS theory," *Metallurgical and materials transactions B,* vol. 35B, 2004.

[34] N. A. Koneva, V. A. Starenchenko, D. V. Lychagin, L. I. Trishkina, N. A. Popova and E. V. Kozlov, "Formation of dislocation cell substructure in face-centred cubic metallic solid solutions," *Materials Science and Engineering A,* Vols. 483-484, pp. 179-183, 2008.

[35] G. A. Malygin, "Kinetic mechanism of the formation of fragmented dislocation structures upon large plastic deformations," *Physics of solid state,* vol. 44, no. 11, pp. 2072-2079, 2002.

[36] D. L. Holt, "Dislocation cell formation in metals," *Journal of applied physics,* vol. 41, pp. 3197-3201, 1970.

[37] A. Seeger and W. Frank, *Structure formation by dissipative processes in crystals with high defect densities,* vol. 3, 1988, pp. 125-138.

[38] H. P. Myers, Introductry solid state physics, London: Taylor and Francis, 1997.

[39] G. A. Malygin, S. L. Ogarkov and A. V. Andriyash, "A dislocation kinetic model of the formation and propagation of intense shock waves in crystals," *Physics of the solid state,* vol. 55, no. 4, pp. 787-795, 2013.

[40] D. Kuhlmann-Wilsdorf, "The theory of dislocation-based crystal plasticity," *Philosophical Magazine A,* vol. 79, no. 4, pp. 955-1008, 1999.

[41] D. Kuhlmann-Wilsdorf, “Q: Dislocations structures - how far from equilibrium? A: Very close indeed,” *Materials science and engineering A,* vol. 315, pp. 211-216, 2001.

[42] G. A. Malygin, “Analysis of the Parameters of a submicron dislocaion structure in metals subjected to severe plastic deformation,” *Physics of solid state ,* vol. 46, no. 11, pp. 2035-2041, 2004.

[43] V. E. Fortov, K. V. Khishchenko, P. R. Levashov and I. V. Lomonosov, “Wide-range multi-phase equations of state for metals,” *Nuclear Instruments and Methods in Physics Research A,* vol. 415, pp. 604-608, 1998.

[44] N. C. Admal and E. B. Tadmor, “A unified interpretation of stress in molecular systems,” *Journal of elasticity,* vol. 100, no. 1-2, pp. 63-143, 2010.

[45] “Solutions: Tools and methods,” Kintech Laboratory, 2013. [Online]. Available: http://www.kintechlab.com/solutions/methodology. [Accessed 5 7 2013].

[46] J. A. Zimmerman, E. B. Webb, J. Hoyt, R. E. Jones and P. A. B. D. J. Klein, “Calculation of stress in atomistic simulation,” *Modelling and simulation in materials science and engineering,* vol. 12, pp. 319-332, 2004.

[47] A. I. Murdoch, “A Critique of Atomistic Definitions of the Stress,” *Journal of elasticity,* vol. 88, no. 2, pp. 113-140, 2007.

[48] Y. Fu and A. C. To, “On the evaluation of Hardy's thermomechanical quantities using ensemble and time averaging,” *Modelling and simulations in materials science and engineering,* vol. 21, no. 5, 2013.

APPENDICES

Appendix A : The equations of Mayer's model

The full set of 17 equations presented by Mayer in [10] is presented here.

The basis of the model is the three continuum mechanics equations:

$$\frac{1}{\rho}\frac{d\rho}{dt} = -\sum_{k=1}^{N}\left(\frac{\partial v_k}{\partial x_k} + \frac{dW_{kk}}{dt}\right)$$

$$\rho\frac{dv_i}{dt} = \sum_{k=1}^{N}\frac{\partial \sigma_{ik}}{\partial x_k}$$

$$\rho\frac{dU}{dt} = \sum_{k=1}^{N}\left(-P\left(\frac{\partial v_k}{\partial x_k} + \frac{dW_{kk}}{dt}\right) + \sum_{i=1}^{N} S_{ik}\frac{dw_{ik}}{dt}\right)$$

The shear and the bulk moduli, G and K respectively, are related by the relation:

$$G = \frac{3}{2}K\frac{1-2\mu}{1+\mu}$$

Where $K = \rho c_b^2$

Describing the evolution of the densities of mobile and immobile dislocations ,as well as the generation rate of mobile dislocations and the immobilisation rate, are four kinetic equations:

$$\frac{d\rho_D^\beta}{dt} = Q_D^\beta - Q_I^\beta - k_a b\left|V_D^\beta\right|\rho_D^\beta\left(2\rho_D^\beta + \rho_I^\beta\right)$$

$$\frac{d\rho_I^\beta}{dt} = Q_D^\beta - k_a b\left|V_D^\beta\right|\rho_D^\beta\rho_I^\beta$$

$$Q_D^\beta = k_g b\left[\frac{2Bc_t^2\left(V_D^\beta\right)^2}{\sqrt{1-\left(V_D^\beta/c_t\right)^2}} + bY\left|Y_D^\beta\right|\right]\rho_D^\beta$$

$$Q_I^\beta = V_I\left(\rho_D^\beta - \rho_0\right)\sqrt{\rho_I^\beta}$$

The dislocation velocity in macroscopic stress field, V_D^β, is found using an equation of motion:

$$m_0 \xi_\beta^3 \frac{dV_D^\beta}{dt} = \left[\sum_{i=1}^{N} \sum_{k=1}^{N} S_{ik} b_i^\beta n_k^\beta \pm \frac{1}{2} bY \right] - B \xi_\beta^3 V_D^\beta$$

Where $\xi_\beta = \frac{1}{\sqrt{1-\left(V_D^\beta / c_t\right)^2}}$, and $B = \frac{4\theta^2 k_B^3}{h^2 c_b^3} T$ is a coefficient of friction which is temperature dependant.

The yield strength is calculated by

$$Y = Y_0 + A_I G b \sqrt{\rho_I}$$

The plastic strain rate is found using:

$$\frac{dw_{ik}}{dt} = -\frac{1}{2} \sum_\beta \left(b_i^\beta n_k^\beta + b_k^\beta n_i^\beta \right) V_D^\beta \rho_D^\beta + \Omega_{ik}$$

The stress deviators are found:

$$S_{ik} = 2G \left[u_{ik} - \frac{1}{3} \delta_{ik} \sum_{l=1}^{N} (u_{ll} + W_{ll}) - w_{ik} \right]$$

Finally a subset of equations describe fracture effects. Firstly the equation for the thermal nucleation rate of micro-cracks:

$$\frac{dn}{dt} = \frac{c_t}{16 R_{cr}^4} \frac{\exp\left(-2\pi\gamma R_{cr}^2 / (3k_B T)\right) - \exp(-\gamma/\Delta\gamma)}{\left[1 - 2\pi\Delta\gamma R_{cr}^2 / (3k_B T)\right][1 - \exp(-\gamma/\Delta\gamma)]}$$

$$\sigma_n = \sum_{i=1}^{N} \sum_{k=1}^{N} \sigma_{ik} e_i e_k$$

The growth of existing cracks is describes by:

$$\rho \frac{\sigma_\beta}{G} \left(R^2 \ddot{R} + \frac{3}{2} R \dot{R}^2 \right) = -4(\gamma - \gamma') + 6R \frac{\sigma_n^2}{G}$$

$$\gamma' = \rho b \rho_0 c_t R^2 \dot{R}/2$$

$$\frac{dW_{ik}}{dt} = -e_i e_k \frac{1}{1-\alpha}\frac{d\alpha}{dt} + O_{ik}$$

Where $\alpha = n2\pi R^2 \sigma_n/G$ is the volume fraction of cracks.